Development of conducting polymer-based composites for flexible gas sensor devices

by

Guodong Wu

A dissertation submitted to Graduate Faculty of
Auburn University
in partial fulfillment of the
requirements for the Degree of
Doctor of Philosophy

Auburn, Alabama
December 9, 2023

Keywords: flexible substrate, conducting polymers, gas sensor, carbon dioxide, breath analysis,
volatile sulfur compounds.

Approved by

Dr. Dong-Joo (Daniel) Kim, Chair, Professor of Materials Engineering
Dr. Pengyu Chen, Associate Professor of Materials Engineering
Dr. Siyuan Dai, Assistant Professor of Materials Engineering
Dr. Xinyu Zhang, Professor of Chemical Engineering

Abstract

In the realm of gas sensing technologies, there has been a remarkable upswing in demand for sensors that are not only flexible and wearable but also versatile, able to monitor a variety of environmental markers from pollutant levels to human respiratory rates. This dissertation delves into the exploration and advancement of these wearable, flexible gas sensors made from conducting polymers (CPs), emphasizing their potential when integrated with Carbon Nanotubes (CNTs) and two-dimensional (2D) materials, such as graphene and MXenes.

For the first time, disposable masks, predominantly comprised of polypropylene (PP) fibers, were leveraged as flexible substrates for wearable sensing applications. When combined with conducting polymers and bolstered by CNTs or 2D materials, these disposable or discarded masks facilitate a straightforward synthesis process, leading to cost-effective and high-sensing performance (e.g., excellent sensitivity and selectivity, rapid response/recovery time towards target gas) nanocomposites.

The pivotal discoveries of this dissertation include:

Breath Analysis and Odor Detection: Our innovatively crafted wearable wireless Bluetooth sensors displayed exceptional promise in breath analysis, particularly in charting human respiratory rates. Furthermore, these sensors proved adept in identifying foul-smelling gases for potential health monitoring and detecting food degradation.

Effects of External Factors: Through meticulous experimentation, we discerned the sensors' reactions under diverse conditions, such as varying synthesis sequences, gas concentrations,

temperature shifts, humidity levels, component ratios, and even in different physical states like bending or folding. While these sensors might retain their sensitivity, subtle variations were noticed. These can be ascribed to the intrinsic qualities of the conducting polymers and their interplay with the embedded nanostructures.

Sensing Mechanism Exploration: A thorough exploration into the sensing mechanism highlighted the collaborative roles, such as the formation of heterojunctions, enhanced conductivity, and increased specific surface areas, of the conducting polymer when integrated into a hybrid structure with other materials. This synergy not only boosted the sensor's capability but also provided insights into the dynamics of charge carrier transfers and their pivotal role in gas detection.

The notable improvements in the performance of the fabricated flexible gas sensors underline the immense potential in melding conducting polymers with cutting-edge nanomaterials. Harnessing waste masks for such sophisticated purposes accentuates the potential for eco-friendly advancements in wearable technology. The potential applications of these enhanced sensors span medical diagnostics, environmental surveillance, and industrial safety measures. By leveraging the unique properties of conducting polymers and amalgamating them with nanostructures, we have developed advanced, flexible, wearable gas sensing devices, setting the stage for a future where these sensors are an integral part of our daily lives.

Acknowledgments

Firstly, I would like to give special thanks to my advisor Dr. Dong-Joo Kim for his constant encouragement and guidance throughout my Ph.D. career. I sincerely appreciate all his contributions with his precious dedication, counsel, to guide me during my Ph.D. study at Auburn University. I am also grateful to my committee members, Dr. Pengyu Chen, Dr. Xinyu Zhang, Dr. Siyuan Dai, and my university reader, Dr. Bryan Beckingham for providing their precious time and insightful comments on my research projects and the dissertation.

I would like to express my sincere gratitude to Dr. Haishun Du for generously sharing his research experience, ideas and resources with me to support my research. The achievements in this dissertation would not have been realized without this precious collaboration.

I would like to thank Dr. Majid Beidaghi at the Department of Materials Engineering; Dr. Tae-Sik Oh at the Department of Chemical Engineering; Dr. Xuejun Pan, at the Department of Biological Systems Engineering, University of Wisconsin-Madison; for their numerous support or discussions for my research projects. Especially, thank you Mr. Steve Moore and Ms. Cheryl Rhodes for many services in the material engineering department.

I am also thankful to my friends and collaborators: Shang-Tung Chiang, Kiandokht Pakravan, Jiachen Liu, Haoran Wang, Farshad Feyzbar K Nejad, Adam Bachmann, Houshang Yin, Mingyuan Chen, Yue Liang, Yufei Nan, for many enjoyable conversations, friendships and excellent collaboration.

Additionally, I would like to express my heartfelt gratitude to my labmates, Doohee Lee, Wonhyeong Kim, Jaesik Yoon, and Yoo Lim Cha, for their invaluable assistance and unwavering support in the laboratory.

Lastly, I am very grateful to my parents for their endless love, constant moral support and encouragement throughout the years.

Table of contents

List of Figures

List of Tables

List of Abbreviations

PANI Polyaniline

PPy Polypyrrole

PP Polypropylene

MOSs Metal oxide semiconductors

COVID-19 Coronavirus disease 2019

SARS-CoV-2 Severe Acute Respiratory Syndrome Coronavirus 2

CPs Conducting polymers

PEDOT Poly(3,4ethylenedioxythiophene)

GC Gas chromatography

NDIR Nondispersive infrared spectroscopy

VWR VWRINTERNATIONAL, LLC

Pt Platinum

Ti Titanium

Ag Silver

Au Gold

Pd Palladium

DI Water Deionized water

HF Hydrofluoric

DMSO Dimethyl Sulfoxide

RT Room Temperature

ML Multilayered

PET Polyethylene Terephthalate

PVC Poly Vinyl Chloride

SEM Scanning Electron Microscopy

XRD X-ray Diffraction

EDS Energy Dispersive X-ray Spectroscopy

XPS X-ray Photoelectron Spectroscopy

FTIR Fourier Transform Infrared Spectroscopy

AFM Atomic Force Microscopy

I-V Current Voltage

NMR Nuclear Magnetic Resonance spectroscopy

VOC Volatile Organic Compound

UV Ultra Violet

DC Direct Current

RF Radio Frequency

MFC Mass Flow Controller

S/N Signal to Noise

LOD Limit of Detection

Chapter 1 Introduction

1.1 Background and motivation

Breath analysis has steadily emerged as an essential non-invasive diagnostic tool for evaluating human health. The composition of human exhaled breath comprises approximately 79% nitrogen, 16% oxygen, 4% carbon dioxide, water, and thousands of trace gases [1]. Variations in the content of these trace gases can be indicative of specific health conditions. CO_2, a predominant greenhouse gas, has witnessed a surge in environmental levels due to increased fossil fuel consumption. Additionally, CO_2 serves as a crucial biomarker for diagnosing respiratory diseases [2]. High concentrations of CO_2 in enclosed spaces can lead to reduced oxygen availability, further resulting in respiratory ailments such as asthma, allergies, and dizziness [3].

Among trace gases explored for a biomarker, volatile sulfur compounds (VSCs) - notably methyl mercaptan (CH_4S), dimethyl sulfide (C_2H_6S), and hydrogen sulfide (H_2S) - play a pivotal role in detecting halitosis associated with periodontal disease and renal failure. Moreover, ammonia (NH_3), present in human exhalation, acts as a biomarker for specific conditions, finding its application in non-invasive clinical diagnostics like end-stage renal disease (ESRD) monitoring, pylorus helicobacter detection, and hepatic encephalopathy diagnosis. Traditional methodologies like gas chromatography (GC), mass spectrometry (MS), and selected ion flow tube mass spectrometry (SIFT-MS) have been employed for breath monitoring [4]. Yet, these techniques are not amenable to on-the-go, real-time analysis of low-concentration gases due to their intricate processing, substantial cost, cumbersome size, and extended analysis duration.

Conducting polymers (CPs), including polyaniline (PANI), polypyrrole (PPy), and poly(3,4-ethylenedioxythiophene) (PEDOT), have garnered substantial interest in crafting flexible gas sensors tailored for environmental and health monitoring. Of these, PANI exhibits remarkable potential for crafting flexible NH_3 sensors. However, pure CPs tend to deprotonate in the air, leading to a pronounced decline in their long-term stability. To circumvent this stability conundrum, research has ventured into CP-carbon series materials and CP-metal oxide semiconductor composites. However, these CP-based composite sensors often grapple with subpar sensing attributes, manifesting as diminished sensitivity and selectivity, sluggish response kinetics, and extended recovery durations. Besides, the literature still lacks an exhaustive exploration into the sensing mechanism of CP-based composites. Furthermore, an overarching challenge that persists is the fabrication of a lightweight, wearable device that seamlessly integrates with wireless systems, enabling efficient and swift monitoring of respiratory rates for potential ailment diagnosis.

1.2 Objectives of research

In this dissertation, we address the development of superior gas sensors integrated into wearable substrates by overcoming the aforementioned limitations: the ambiguous sensing mechanism of CP-based composites and challenges such as limited adaptability, high operational temperatures, and insufficient sensing performance.

Prompted by the environmental concerns stemming from discarded masks and the research challenges associated with CPs, we repurposed disposable or waste masks as flexible substrates. By melding CPs with CNT or other 2D materials like graphene and MXenes, we architect a nanocomposite that significantly enhances sensing performance, making it apt for breath analysis

and food spoilage monitoring. Additionally, this work delves into the refined sensing mechanisms underpinning the heightened performance of CP-based hybrids by examining the influence of variables such as gas concentration, temperature, humidity, component ratios, and physical alterations like folding and bending on the sensor's properties.

Based on the previously discussed motivations, this dissertation is structured to emphasize four primary tasks presented in Chapters 3-6:

Chapter 3: Flexible Mask Sensors Based on CNT/PANI Nanocomposite for Ammonia Sensing and Breath Analysis. In this chapter, our primary focus is to enhance the stability and sensitivity of PANI-based ammonia sensors. We employed disposable masks as flexible substrates to develop a porous PP/CNT/PANI nanocomposite gas sensor. This involved drop-coating a surfactant-augmented CNT aqueous solution onto the mask's porous polypropylene fibers, succeeded by in-situ polymerization of aniline on the PP/CNT structure. The resulting gas sensor displays remarkable stability due to van der Waals forces and π–π interactions between CNT and PANI. Its sensitivity is enhanced by improved charge transfer channels and a porous structure that facilitates ammonia gas adsorption. Importantly, the sensor can detect breathing patterns in real-time, signifying the potential for noninvasive human breath monitoring. A significant portion of breath signals originate from ammonia and moisture in exhaled breath. While volatile sulfur compounds, CO_2, and volatile organic compounds in exhaled breath slightly influence the sensing signals, we delve deeper into their effects in Chapters 4-6.

Chapter 4: Graphene/PANI Functionalized Mask Sensors for Ammonia and Volatile Sulfur Compounds Detection. Expanding on the previous chapter, we investigated the influence of VSC on breath sensing patterns. We sought to improve sensitivity and assess how humidity affects NH_3

and H$_2$S sensing performance. A flexible PP/G/PANI hybrid gas sensor was fabricated through dip-coating, followed by in-situ polymerization using a discarded disposable mask as substrate. The sensor's morphology, structure, surface chemistry, and surface area were characterized using SEM, EDS-mapping, FTIR, and BET analysis. We introduced an odor-sensing system capable of identifying malodorous gases in exhaled breath, a promising diagnostic tool for kidney diseases. The superior sensing capabilities can arise from the efficient conducting paths formed by the G/PANI network and the hierarchical porous architecture of the PP/G/PANI.

Chapter 5: Conductive Ti$_3$C$_2$T$_x$/PANI-PP Composite Sensor for CO$_2$ Detection and Human Respiratory Rate Monitoring. To examine the impact of CO$_2$ on breath sensing patterns, emphasize enhancing selectivity and sensitivity and explore the heterojunctions effects on sensing mechanism. We present the Ti$_3$C$_2$T$_x$/PANI-PP hybrid sensor, crafted by incorporating ammonium persulfate (APS) into a Ti$_3$C$_2$T$_x$-infused aniline solution, which then underwent in-situ polymerization and film deposition on a mask substrate. This composite sensor is adept at monitoring human respiratory rates in real-time, and we explored factors influencing the breath signal dynamics. The stellar performance of the Ti$_3$C$_2$T$_x$/PANI-PP sensor can be attributed to the heterojunctions between Ti$_3$C$_2$T$_x$ and PANI, heightened conductivity, and expanded specific surface area.

Chapter 6: Wearable Ethanol Sensor for Drunk Driving Monitoring Based on Ti$_3$C$_2$T$_x$ /Polypyrrole Functionalized Face Mask. To examine the effect of ethanol on breath-sensing patterns while aiming to boost the gas sensor's response time. We created the PP/Ti$_3$C$_2$T$_x$/PPy composite gas sensor by spray-coating MXene onto a face mask surface, then in-situ polymerized aniline on the MXene-PP film using APS. The enhanced sensing performance of the PP/Ti$_3$C$_2$T$_x$ /PPy composite

sensor can be traced back to the rich functional groups, such as amino groups in PPy and terminal groups in $Ti_3C_2T_x$, combined with the Schottky junction between $Ti_3C_2T_x$ and PPy.

These chapters comprehensively address the challenges and explore the potential of flexible, wearable sensors for diverse applications.

Chapter 2 Research background

2.1 Conducting polymers

Polymers were considered to be electrical insulators before the invention of conducting polymers (conjugate polymers), but these organic polymers have unique electrical and optical properties similar to those of inorganic semiconductors [1]. A conjugated carbon chain consists of alternating single and double bonds, where the highly delocalized, polarized, and electron-dense π bonds are responsible for its electrical and optical behavior. Typical conducting polymers include polyacetylene (PA), polyaniline (PANI), polypyrrole (PPy), polythiophene (PTH), poly(para-phenylene) (PPP), poly(phenylenevinylene) (PPV), and polyfuran (PF) [2], as shown in Figure 2-1. Alan G. MacDiarmid and physicist Alan J. Heeger [3] discovered (SN)x sulfur nitride metal, an inorganic material, which showed higher electrical conductivity when doped with bromine, and this finding led to the investigation of conducting polyacetylene. The solubility and processability of conducting polymers depend mainly upon the attached side chains, and the attached dopant ions give them mechanical, electrical and optical properties. Conducting polymers are crystalline and partially amorphous. Conducting polymers consist of both localized and delocalized states, and the delocalization of π bonds depends heavily upon disorder, and this delocalization plays an essential role in the generation of charge carriers like polarons, bipolarons, solitons, etc., which are responsible for the transition from insulator to metal. Conducting polymers were synthesized using various methods, including chemical oxidation, electrochemical polymerization, vapor phase synthesis, hydrothermal, solvothermal, template-assisted, electrospinning, self-assembly, and photochemical methods, the inclusion method, the solid state method, and plasma polymerization [1, 4]. Generally, conducting polymers have low electrical conductivity and optical

properties in their pristine state; however, doping with suitable materials can give them excellent properties.
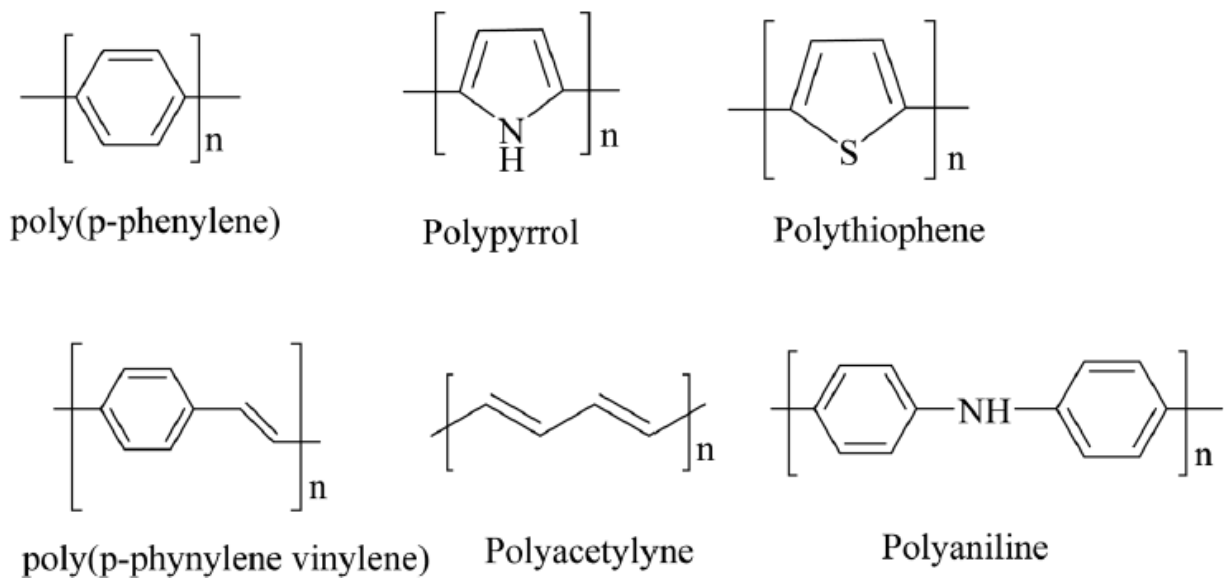
Figure 2-1. Structural illustration of different conducting polymers.

Polyaniline is the most promising and most explored among conducting polymers, and polyaniline has good mechanical property, high processability, tunable conducting and optical properties. [5, 6] The conductivity of polyaniline is dependent upon the dopant concentration, and it gives metal-like conductivity only when the pH is less than 3. Polyaniline exists in different forms. They are classified as leuco-emeraldine, emeraldine, and pernigraniline, by their oxidation state, i.e., leuco-emeraldine exists in a sufficiently reduced state, and pernigraniline exists in a fully oxidized state, as shown in Figure 2-2. Polyaniline becomes conductive only when it is in a moderately oxidized state and acts as an insulator in a fully oxidized state. The synthesis of polyaniline by the chemical oxidation method is shown in Figure 2-3.
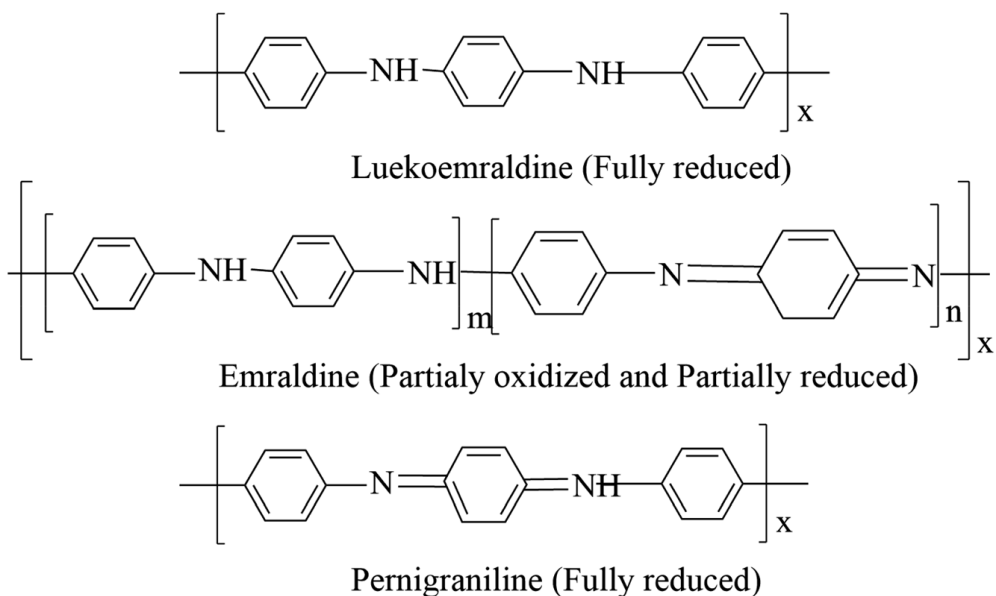
Figure 2-2. Structural illustration of different forms of polyaniline.
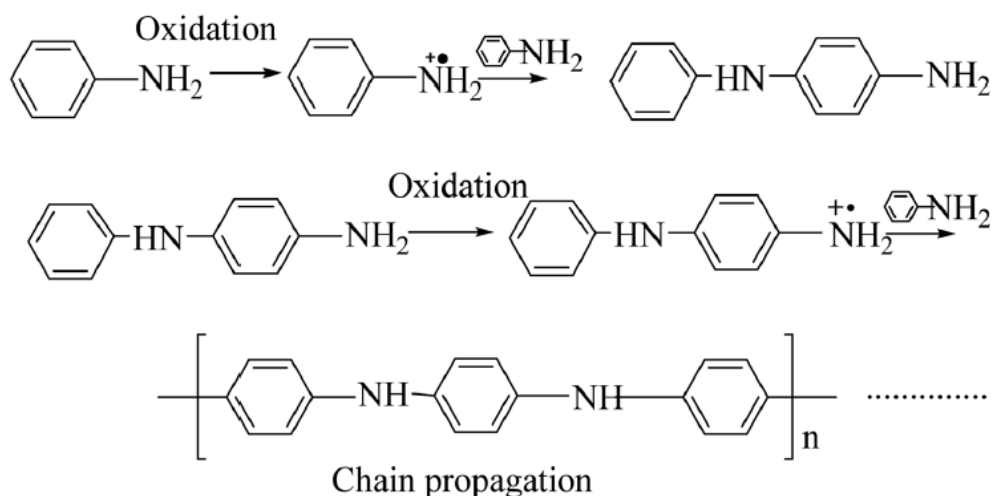
Figure 2-3. Synthesis of polyaniline by the chemical oxidation method.

Polypyrrole is unique due to its increased commercial interest because of its high stability, enhanced conductivity, and it is relatively easy to form homopolymer and composites from it. Polypyrrole was first prepared by the chemical oxidation of a pyrrole monomer in the presence of hydrogen peroxide, and it is a black powdery material [7, 8]. Polypyrrole behaves like an insulating

8

material in its undoped virgin state, and it shows a constant conductivity of 10^{-5} s m^{-1} when doped with halogenic electron acceptors such as bromine or iodine. It is not crystalline, and acts as amorphous in nature, but bulk polypyrrole has 15% crystallinity, and the crystalline region is in the monoclinic phase. For electrochemically synthesized polypyrrole with a thickness of 1 μm and a yellow blackish color, transformation occurs by an increase in protonation concentration and it has higher stability in air and high thermal stability in the range of 300 °C; thermal degradation can occur due to the loss of dopant anions.

Nowadays, conducting polymers have attracted much attention in the field of battery, supercapacitors, biomedical, gas sensors (as shown in Figure 2-4) due to their good electrical conductivity, facile synthesis process, low operating temperature, and inherent compatibility with polymer substrates [9].
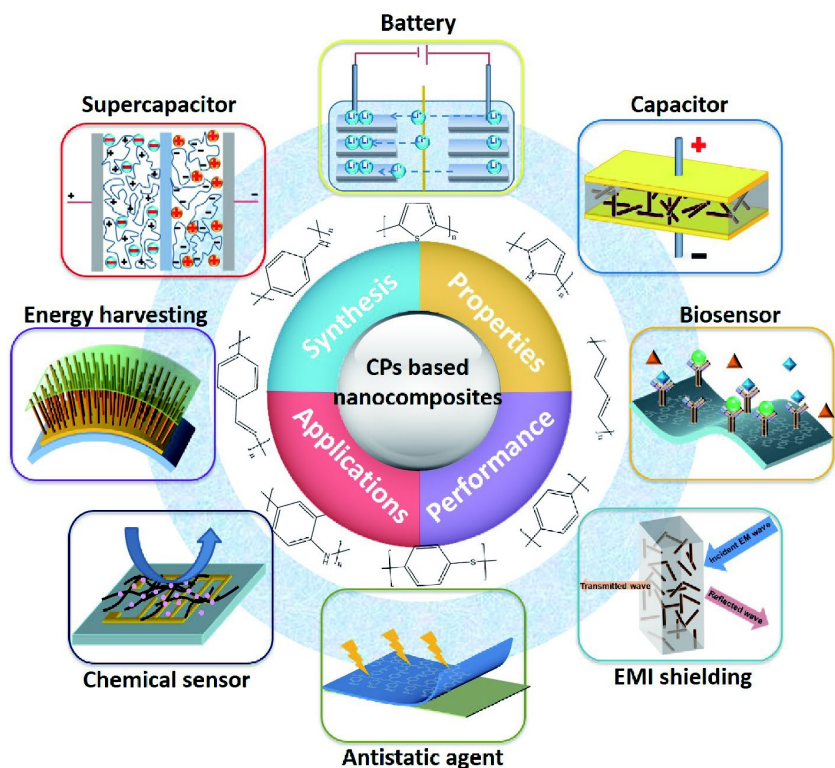
Figure 2-4. Schematic illustration of applications of conducting polymers and their composites.

2.2 Flexible and wearable gas sensing devices

Nowadays, the growing demands for portable and wearable electronics have promoted increasing academic interest in flexible electronics [10]. Conventional silicon based materials and organic semiconductors have been widely investigated for flexible electronics but their low stability and flexibility greatly limit the further practical application [9]. Comparatively, low-dimension materials, such as CNTs, with excellent electrical and optical properties, higher carrier mobility and size-related intriguing physical properties, are becoming promising materials in the construction of flexible electronics in terms of their room-temperature operability, rapid signal response, ease of use, and selectivity [11].

A typical CNT based flexible sensor was reported by Srikanth Ammu and co-workers, which was made from single walled carbon nanotube thin films on cellulose (paper and cloth) via inkjet-printed method [12]. Resistance changes were observed in relation to Cl_2 and NO_2 vapor with concentration of 5 to 100 ppm at room temperature due to the weak charge-transfer between CNTs and gases [13]. It was demonstrated that flexible substrate selection was an important factor for sensor recovery performance. Porous cellulosic substrates facilitated the gas recovery in ambient environment at room temperature, while flexible polyethylene terephthalate (PET) substrates required photoirradiation treatment for recovery [8, 14]. Despite the impressive flexibility of CNT based sensors, the signal response speed is too sluggish for practical real time application due to the weak adhesion of gas molecules on sensing materials. Motivated by this, Huan Liu and co-workers reported PbS colloidal quantum dots (CQD) on a flexible paper substrate via the layer-by-layer spin-coating deposition technique [15]. The porous thin CQD film of 80 nm guaranteed the rapid diffusion of gas, which enabled the rapid response at room temperature, high sensitivity, good reversibility, and outstanding mechanical bending ability. In brief, rational design of one

dimensional materials or patterned nanoparticles with excellent sensing properties and good adhesion to flexible substrates is a feasible strategy for flexible sensor construction.

Recently, flexible conductive polymer film-based gas sensors have attracted widely scientific attention for environment and human health monitoring (as shown in Figure 2-5) due to their wearability, flexibility, transparency, and compatibility over curved substrates of integrated electronics [16, 17].
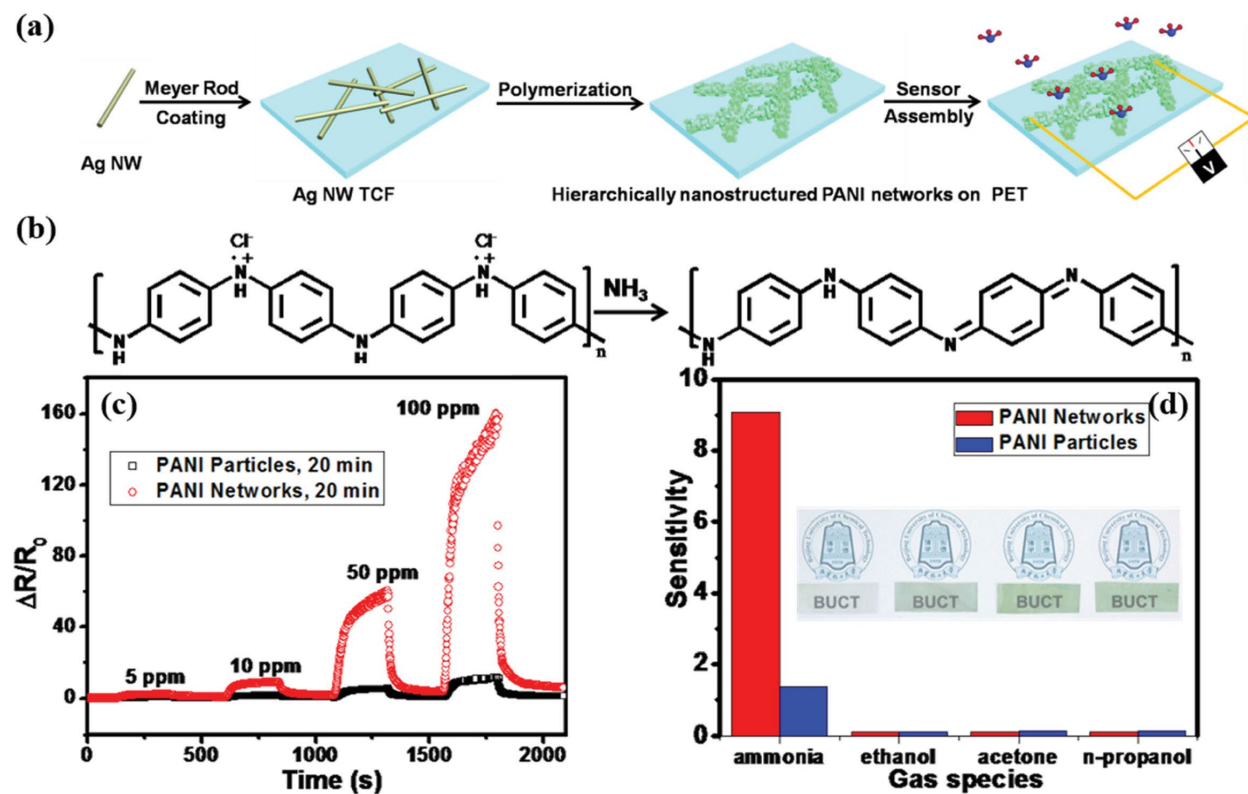
Figure 2-5. a) Scheme of fabrication of PANI networks based transparent conducting film on PET substrate. b) Sensing mechanism of acid-doped PANI toward NH_3. c) The gas sensing of the PANI network-containing transparent film (red) and the particle-like PANI (black) upon exposure towards NH_3. d) Gas sensing selectivity test of the PANI network-containing transparent film.

2.3 Breath analysis and disease diagnosis

Respiration is an uninterrupted vital biomechanical behavior that lasts throughout human's whole life, regardless of health condition. However, it has traditionally been an underutilized resource even though it encompasses profuse physiological information [18]. Compared with blood analysis and endoscopy, respiration analysis is a fast, non-invasive, painless, low-cost, and convenient approach for early illness diagnosis and real-time physiological monitoring [19]. Assessment of the diaphragmatic movement during breathing (dash line, as shown in Figure 2-6) can provide the early recognition of human diseases like abnormalities apnea, asthma, cardiac arrest, and lung cancer. Furthermore, the obstructive sleep apnea syndrome (SAS), arising from the collapse of the soft tissues at upper respiratory tract, poses a huge hazard in human health and safety and the potential causes for various diseases, such as diabetes, hypertension, stroke and even nocturnal death. Monitoring the respiratory behaviors and status favors the immediate alarms for SAS occurrence and appropriate treatment in time, which is of great significance to decrease the risk of respiratory diseases and possibility of sudden death [20]. Aside from the detection of physical respiratory biomechanical motions, respiration also dominates the air exchange process between alveolar spaces of the lung and the ambient atmosphere. The exhaled gases are a mixture of as many as 500 different chemical compounds, including carbon dioxide, nitrogen, oxygen, water vapor, and volatile organic components [21]. The constituents and concentration of the respiratory gases can serve as the biomarkers to provide a large amount of biochemical and physiological information on the bronchi and pulmonary alveoli for disease diagnosis and earlier intervention [22]. The ancient Greek physicians used to diagnose the potential diseases by smelling the odor of patient's breath. The Israel scientists proposed a method to predict the possibility of gastric cancer by identifying the concentration of five VOCs (2-propenenitrile, 2-butoxyethanol, furfural and 6-

methyl-5-hepten-2-one and isoprene) from the exhalation of patients via nanomaterial-based sensors [19]. Nowadays, with the rapid development of modern medicine, respiration monitoring has been proven to be a promising and useful approach for a variety of disease predictions, especially suitable for the underdeveloped countries. As shown in Figure 1, a variety of breathing gases have been utilized as the biomarkers for early illness prognosis of internal organs, that is, ammonia is the biomarker for kidney disease, [20-22] and ethanol can be employed as an indicator for liver cirrhosis. The methane (CH_4) breath test offers a facile, non-invasive and inexpensive means of identifying small intestinal bacterial overgrowth (SIBO) [23]. More than 30 ppb nitrogen monoxide indicates the possibility of asthma due to the airway inflammation. Approximately 22% of the 86 million people in the United States with prediabetes are unaware of their condition, and acetone concentration in their exhalation gas can be regarded as an indicator to reflect the illness status [24]. Furthermore, dimethyl sulfide and 1-methylthio-propane were found to be among the compounds able to distinguish lung cancer patients from healthy volunteers. Table 2-1 lists the physiologic origins of endogenous breath molecules [25].
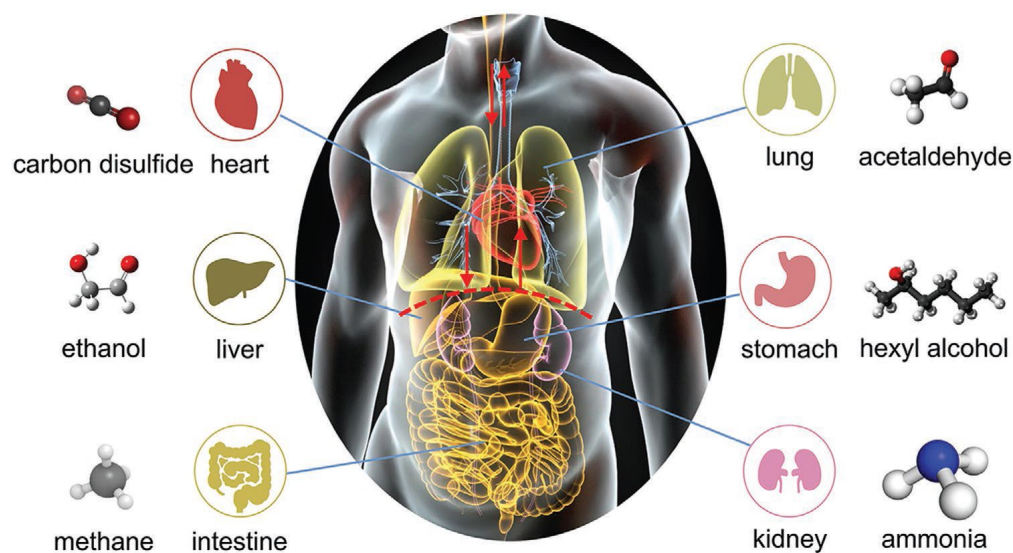
Figure 2-6. Respiratory gases for physiological and pathological assessment.

13

Table 2-1. Physiological origins and concentration of endogenous breath molecules.

Compound	Physiological basis	Concentration
Acetaldehyde	Ethanol metabolism	ppb
Acetone	Decarboxylation of acetoacetate	ppm
Ammonia	Protein metabolism	ppb
Carbon Disulfide	Gut bacteria	ppb
Carbon Monoxide	Production catalyzed by heme oxygenase	ppm
Carbonyl Sulfide	Gut bacteria	ppb
Ethane	Lipid peroxidation	ppb
Ethanol	Gut bacteria	ppb
Hydrocarbons	Lipid peroxidation/metabolism	ppb
Hydrogen	Gut bacteria	ppm
Isoprene	Cholesterol biosynthesis	ppb
Methane	Gut bacteria	ppm
Methanethiol	Methionine metabolism	ppb
Methanol	Metabolism of fruit	ppb
Methylamine	Protein metabolism	ppb
Nitric oxide	Production catalyzed by nitric oxide synthase	ppb
Pentane	Lipid peroxidation	ppb

2.4 Volatile sulfur compounds, volatile organic compounds detection

Human exhaled breath contains thousands of trace gases, except for 79% of nitrogen, 16% of oxygen, and 4% of carbon dioxide [26]. The concentration variations in these trace gases are related to specific pathologies [27]. Among them, volatile organic compounds (VOCs) are prominent air pollutants in both industrial processes and urban environments. These compounds can evaporate into the atmosphere at room temperature and standard atmospheric pressure, leading to the formation of harmful pollutants. Prolonged exposure to VOCs can adversely affect the human

nervous system, kidneys, and liver. VOCs encompass a variety of compounds, including alcohols, acids, ketones, aldehydes, ethers, and esters. Some of these have the potential to cause cancer and other severe health issues, posing long-term risks to human health and atmospheric quality [24, 27] Interestingly, trace levels of VOCs can also be detected in human exhalation. These trace compounds can act as biological indicators, offering valuable insight for non-invasive early disease diagnosis by providing key physiological and metabolic information. Ethanol, a commonly known VOC, is extensively used in various sectors such as biochemistry, pharmaceuticals, paint manufacturing, and the food and beverage industry. It's important to note that ethanol vapor is highly flammable and can present a significant explosion risk, with explosive concentrations ranging between 3.3–19.0%.

Besides, volatile sulfur compounds (VSCs), including hydrogen sulfide (H_2S), methyl mercaptan (CH_4S), and dimethyl sulfide (C_2H_6S) are considered to be indicators of halitosis. Volatile sulfur compounds (VSCs), dimethyl disulfide (DMDS), methyl sulfide (DMS), and carbon disulfide (CS_2) are serious concerns, as environmental pollutants because of their high neurotoxicity [28]. DMDS has an extremely unpleasant smell like pungent garlic and contact or inhalation of DMDS may irritate or damage the eyes and respiratory system. Exposure to high-concentration DMS in the short term may cause stomach pain and diarrhea, and even lung congestion. H_2S impairs cellular metabolism, causing the so-called "histotoxic hypoxia". At high concentrations, H_2S can cause respiratory paralysis with consequent asphyxia. Moreover, CS_2 affects the olfactory organs [29]. VSCs need to be detected in a highly sensitive and discriminative/selective manner because of its relevance to diagnosis of diseases and approach towards different treatment methods for human health. In nature, some mammals use about hundreds of receptors to identify elements to detect and discriminate thousands of different odors. Halitosis is related to periodontal diseases with

VSCs at trace amount of ppb-ppm [30]. Humans with halitosis have H_2S concentrations from 80 ppb (2.3 µM) up to 2 ppm (57 µM). Traditionally, trace VSCs in-breath are always determined by gas chromatography (GC) [31] and mass spectrometry (MS) [32]. However, these methods mostly require expensive instruments, complicated sample pretreatments, and long analysis time. Gas sensor [33] is another class for H_2S detection, but the sensor always needs to be heated to a high temperature. Therefore, there is a strong demand for developing a simple and portable device with high sensitivity for the real-time monitoring of VSCs in exhaled breath [34].

The greenhouse effect produced by industrial and human activity is currently a problem because it contributes to global warming, which changes the climatic patterns, affecting the marine life, agriculture activities, etc. One of the main greenhouse gases highly produced in the environment due to the consumption of fossil fuels is carbon dioxide (CO_2). The excessive presence of this gas is not convenient for the energetic equilibrium of the earth because it absorbs the short wavelengths reflected from the earth to the space, which provokes an increase of the earth's temperature. Consequently, the climate patterns also change, producing droughts, floods, and ice melting at the poles [30]. In addition, the high concentration of CO_2 in confined spaces causes a diminution of the oxygen available to breathe, which in turn, causes respiratory diseases such as asthma, allergies, and dizziness[35]. According to the American Society of Heating, Refrigerating and Air-Conditioning Engineers (ASHRAE), the maximum concentrations of CO_2 should be 350–800 ppm and 1000 ppm for outdoor and indoor places, respectively. If those limits are not respected, people can experience headaches, sore throat and nasal irritation [36]. Due to these reasons above, it is suitable the control, monitoring and detection of carbon dioxide concentration in places such as factories (where chemicals or cooling systems are produced), food industries related with

carbonated beverages, agro-industries related with the production of fertilizers, medical centers where incubators are employed and indoor places such as schools, offices, etc [37, 38].

2.5 2D materials

Two-dimensional (2D) materials, such as black phosphorus (BP), graphene, graphene oxide (GO), hexagonal boron nitride (h-BN), and transition metal dichalcogenides (TMDs), have also been employed in flexible gas sensors due to their versatile surface chemistry, low electronic noise, large specific surface area, and outstanding electrical properties. However, their relatively low sensitivity and interference from humidity limit their sensing applications. Comparably, ever since their discovery in 2011, 2D transition-metal carbides/nitrides (collectively denoted as MXenes) are attracting enormous research interests [39]. As illustrated in Figure 2-7, MXenes have a general formula of $M_{n+1}X_nT_X$, where n = 1, 2, or 3, representing three common structures. M stands for an early transition metal, such as Ti, Mo, and V, X refers to carbon/nitrogen, while T_X represents various surface terminations, for example, fluorine (−F), hydroxyl (−OH), and/or oxygen (=O) [40]. In case of double transition-metal MXenes, the M atoms can exist either in random (solid solution) or ordered arrangement, where the ordered phase is energetically more stable. Typically, MXenes possess excellent mechanical strength, good thermal conductivity, tunable bandgap from semiconducting to metallic, and hydrophilic surfaces with abundant functional groups that can be postmodified and solution processed [41]. These characteristics render MXenes an ideal platform as sensing materials for a number of applications.

At present, the commonly used strategy for preparing MXene nanosheets is the top-down etching from MAX phases ($M_{n+1}AX_n$), where A represents an A-group element (e.g., Al and Si). Generally, the M–A bond is considered to be metallic, whereas the M–X bond features multiple characters of ionic, metallic, and covalent. Therefore, in contrast to the exfoliation of graphene, the metallic M–

A bond is difficult to break by mechanical shearing. Nevertheless, it is feasible to be selectively etched rather than M–X bonds. The preparation of MXenes typically includes two steps, namely the selective etching of A and the delamination of MXenes.
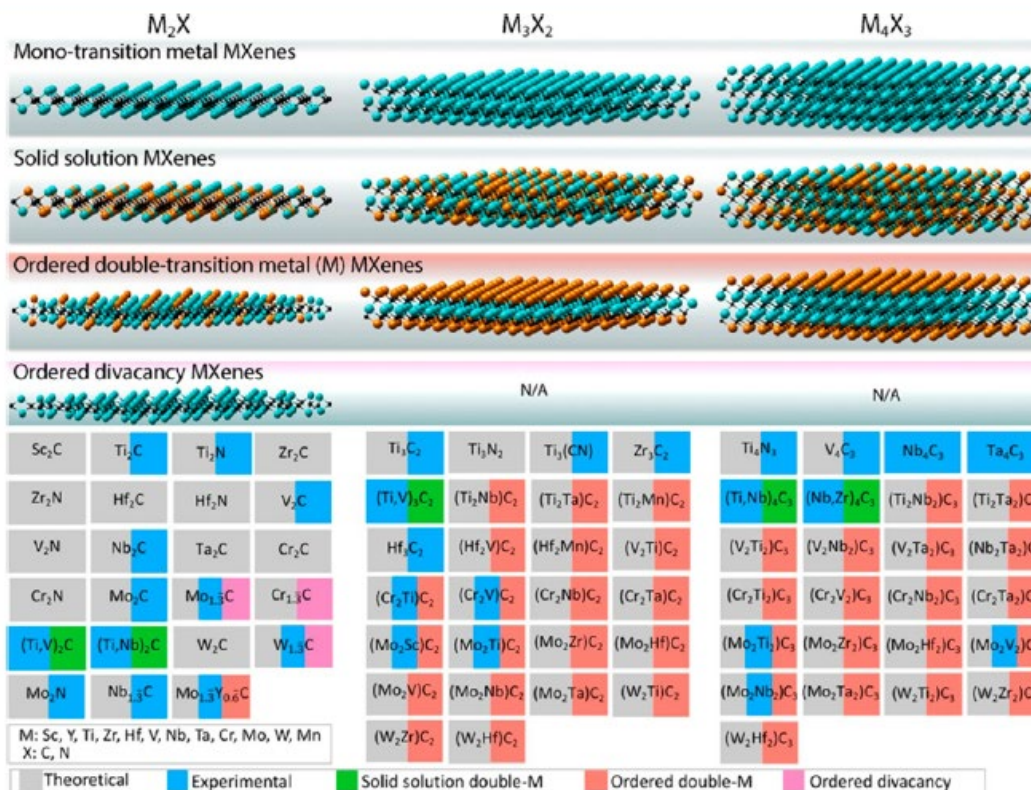
Figure 2-7. Compositions of MXenes were predicted theoretically and obtained experimentally.

The quantification of gaseous species, such as CO, NO, CO_2, NO_2, NH_3, H_2S, and SO_X, are of essential importance for human health, industry safety, emission, and air quality monitoring. Because of its 2D layered structure and adjustable surface terminations, MXenes are considered an ideal platform for gas sensing. The suitability of Ti_2CO_2 MXene as sensing material for NH_3 was predicted using DFT calculations by Yu and co-workers. Ti_2CO_2 [41] was the semiconductor and showed strong adsorption to NH_3 at Ti sites with a binding energy of -0.37 eV (Figure 2-8a). Comparably, due to the weak interaction, Ti_2CO_2 has no response to H_2, CO_2, O_2, CO, N_2, NO_2,

and CH_4 (Figure 2-8b). The suitability of semiconducting M_2CO_2 (M = Sc, Ti, Zr, Hf) for NH_3 sensing was also theoretically evaluated, and the results showed that the effective release/trapping of NH_3 on M_2CO_2 can be controlled by the charge state of M. This conclusion was supported by Khakbaz and co-workers [42] who analyzed the gas sensing performance of $Ti_3C_2T_x$ in the presence of different surface terminations and water molecules. The binding energy between NH_3 and the Ti sites near to O atoms is 60%–180% larger than that adjacent to F atoms, indicating that the $Ti_3C_2T_x$ with a low content of F terminations was preferred for NH_3 sensing.
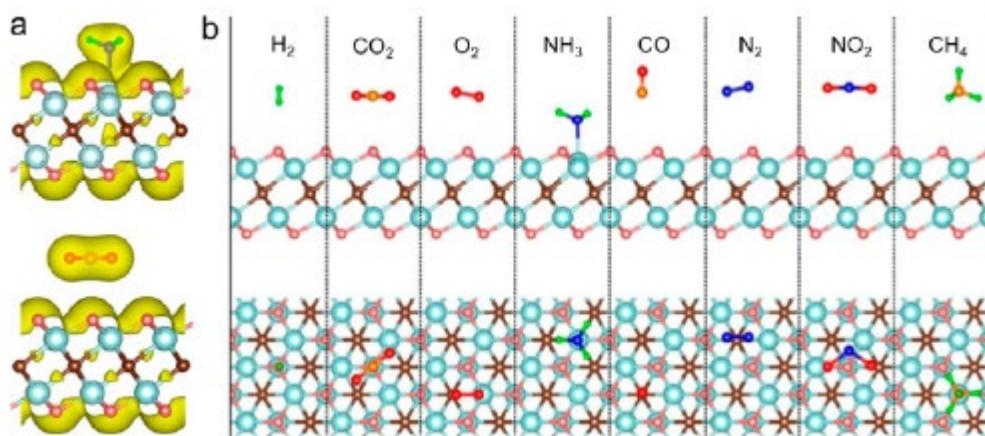
Figure 2-8. (a) The density of states of the single-layer Ti_2CO_2 upon the adsorption of NH_3 and CO_2. (b) The side and top views of the adsorption of H_2, CO_2, O_2, NH_3, CO, N_2, NO_2, and CH_4 on Ti_2CO_2.

2.6 Disposable masks and waste masks

At present, the number of COVID-19 infections is close to 300 million, which endangers more than 200 countries and regions in the world. A resource that attracts global attention is personal protection equipment (PPE), especially disposable surgical masks, which can prevent breathing droplets from entering the lungs and largely reduce the risk of infection. It is estimated that last

year, due to the popularity of COVID-19, Africa's daily masks exceeded 700 million, Asia's daily usage exceeded 2.2 billion, and the world's monthly masks exceeded 129 billion.

Disposable surgical masks, as a potential flexible substrate for gas sensors, have been ignored by people for a long time. During the COVID-19 pandemic, it was estimated that the daily use of surgical masks exceeded 130 billion all over the world per month [43]. Disposable surgical masks consist of non-biodegradable plastic, polypropylene (PP), which means that it costs hundreds of years to decompose in the environment [33]. The usual treatment methods for surgical masks include sending them to landfills or incinerated. These conventional ways will generate garbage and cause environmental pollution. It is worth noting that some reports have used waste masks for superior microwave absorption [44], desalinating seawater [45], and antibacterial applications [46], (as shown in Figure 2-9) in the past two years. Nevertheless, to our best knowledge, there is no report using surgical masks for gas sensors.
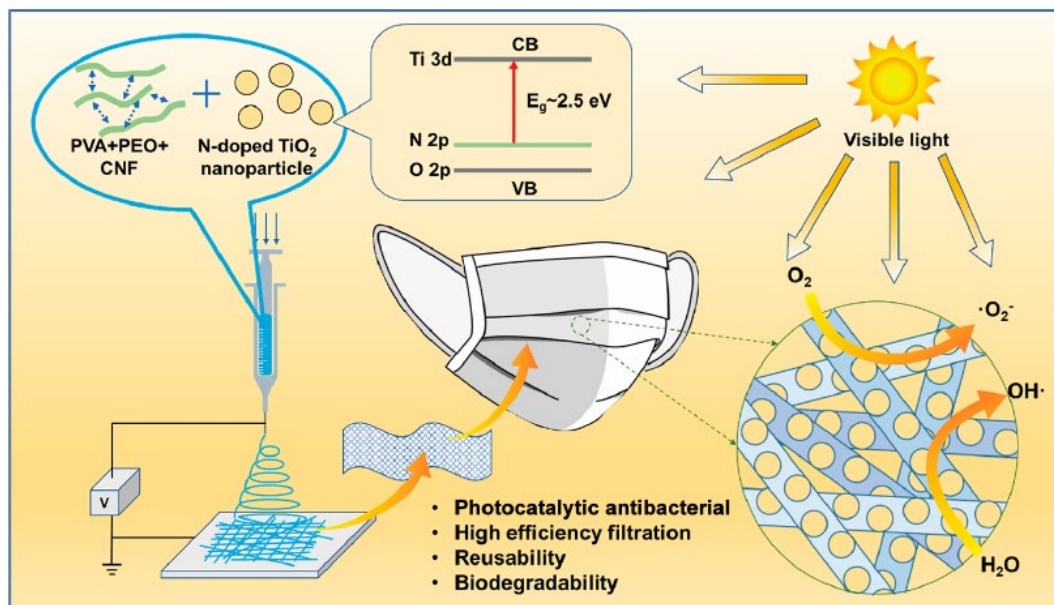
Figure 2-9. Concept of functional and structural designing of reusable mask. Biodegradable PVA, PEO, and nanocellulose were electro-spun into nanomeshes that was followed by depositing photocatalytic N-TiO$_2$.

Chapter 3 Flexible mask sensors based on CNT/PANI nanocomposite for ammonia sensing and breath analysis

3.1 Introduction

Respiration is an uninterrupted biomechanical behavior and one of the basic physiological parameters. Breath analysis with a low-cost, rapid, non-invasive, and painless early diagnosis method is of great significance for managing human health and reducing the risk of respiratory diseases [19, 21, 26, 47]. Real-time respiratory rate monitoring can serve as a vital reference index for the non-invasive detection of cardiac or arterial vascular function [18, 22]. Abnormal respiratory is an important indicator of deterioration in a patient's health [48]. It is also reported that abnormal respiratory rate physiological parameters can be used to monitor typical COVID-19 symptoms [49]. Breath analysis by identifying chemical compounds or biomarkers in exhaled human breath has been an efficient approach to assess metabolic disorders or dysfunction in the human body. Various volatile organic compounds (VOC) such as alcohols, ketones, aldehydes, acids and non-VOC such as ammonia, carbon dioxide, and NOx are related to physiological and metabolic processes in the human body [20, 50].

In particular, ammonia, an essential compound in exhaled gas, is considered a biomarker for the non-invasive clinical diagnosis of liver or kidney disease [5, 24, 51, 52]. The concentration of NH_3 in the exhaled breath of healthy individuals is about 0.4-1.8 ppm, while that in end-stage renal disease patients is around 0.8-14.7 ppm [53]. Currently, gas chromatography (GC) combined with mass spectrometry or ion mobility spectrometry is used to analyze exhaled gas. This method shows a ppb to ppm sensitivity with analysis of multiple compounds. However, such GC-based methods still have limits on their utility in healthcare applications due to bulky volume, high cost, and long diagnosing time by sample collection and pre-concentration procedures [54-56]. Hence, the

21

development of a portable and wearable device to measure trace concentrations of ammonia in exhaled breath can be of great significance for medical diagnosis.

For the past few years, conducting polymers, such as polyaniline (PANI), Polythiophene (PTh), poly(3,4ethylenedioxythiophene) (PEDOT), and polypyrrole (PPy) have been widely investigated as chemiresistive sensing materials for their integration into flexible and wearable technology [1, 57-59]. Such conducting polymers have demonstrated the potential for ammonia gas sensors due to their excellent electrical conductivity mechanical properties, and inherent compatibility with polymer substrates [10, 11, 60]. In particular, PANI has attracted more attention due to its ease of synthesis, high reactivity with ammonia gas, and low operating temperature [61]. It is also reported that surface charge characteristics can be easily improved by changing dopants during the polymerization process [62-64]. Bandgar et al. [65] synthesized a low-temperature ammonia sensor by in-situ polymerization of aniline, showing 99% reproducibility and rapid response with the response value of 26% in 100 ppm NH_3 atmosphere. However, PANI tends to deprotonate in the air, and the charge transfer between polymer chains is poor, so the conductivity of the prepared PANI film is significantly reduced after a few hours [62]. Besides, pure PANI-based gas sensors have apparent disadvantages such as poor long-term stability, low sensitivity, and long response time [66, 67]. As approaches to address the aforementioned issues, PANI-carbon series materials (CNT or reduced graphene oxide) or PANI-metal oxide semiconductor (MOS) materials have been investigated for high-performance conductive film-based ammonia gas sensors [68-70]. Ding et al. [71] fabricated a PANI-based composite sensor by aniline polymerization in 1-pyrenesulfonic acid-functionalized single-walled carbon nanotubes (SWCNTs) suspension, showing better sensitivity and stability than pristine PANI sensor. Liu et al. [72] developed a polyaniline-cerium dioxide (PANI-CeO$_2$) nanocomposite sensor on a polyimide substrate through in-situ self-assembly

method, the PANI-CeO$_2$ ammonia sensor exhibited higher response and shorter recovery time than the PANI one, good reproducibility, splendid selectivity, and low detection limit. Various recent studies have explored the incorporation of conducting polymers onto flexible substrates for gas sensors [17, 73-75]. However, it is still remaining a great challenge to develop a lightweight and flexible platform that can be implemented in wearable devices for sensitive and rapid detection of trace concentrations of ammonia in exhaled breath.

Herein, we fabricated flexible PANI-based composite gas sensors with multi-walled carbon nanotubes (MWCNTs) by incorporating composite sensing materials into polypropylene fibers of a disposable face mask. The nanocomposite sensor showed good sensitivity, fast sensing response/recovery time, room temperature operation, outstanding flexibility, and long-term stability by a uniform coating of PANI/CNT onto porous PP fibers. Besides, the p-PP/CNT/PANI nanocomposite sensor was able to demonstrate real-time human respiration for simultaneous assessing respiratory health and detecting biomarkers.
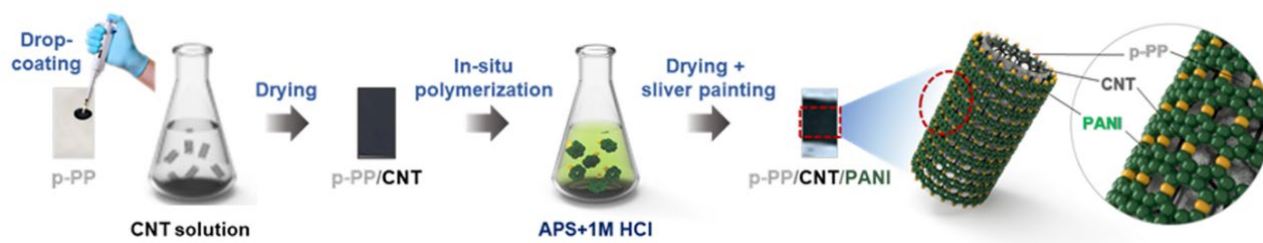
Figure 3-1. Schematic illustration of the preparation of p-PP/CNT/PANI composite film.

3.2 Experimental section

3.2.1 Materials

Disposable masks were obtained from the Zhejiang Stage Leather Apparel Company (Zhejiang, China), and the porous polypropylene non-woven filter layer (denoted as p-PP) of the disposable

mask (after a simple alcohol treatment) was used in this study. Ammonium persulfate (APS), 37% hydrochloric acid, sodium dodecyl benzene sulfonate (SDBS), aniline, and multi-walled carbon nanotubes were obtained from Sigma-Aldrich, USA. The silver painting was bought from VWR (127185-15G).

3.2.2 Preparation of p-PP/CNT composite film

CNT aqueous solutions with different concentrations (1 mg/mL, 0.5 mg/mL, 0.2 mg/mL) were prepared by mixing 0.03 g, 0.015 g, 0.006 g CNT with 30 mL deionized (DI) water through ultrasound (351OR-MTH, 330W) treatment for 20 min, respectively. During the mixing process, a small amount of SDBS was added to enhance the dispersion of CNTs [76, 77]. Afterward, the p-PP film was drop-coated by the as-prepared CNT suspension. After air drying, the p-PP film was drop-coated by the CNT suspension again for preparing the final p-PP/CNT composite film.

3.2.3 Preparation of p-PP/CNT/PANI composite film

Aniline monomer (0.2 mL, 0.4 mL, 4 mL, corresponding to approximate 0.85 mg/mL PANI, 1.7 mg/mL PANI, 17 mg/mL PANI) was added into 1 M HCl aqueous solution (200 mL) in a flask. APS (0.23 g, 0.46 g, 4.6 g) in precooled 1 M HCl solution (40 mL) was poured into the above monomer solution, which was shaken for 30 s and left at 25 °C. Then, a PP substrate and a PP/CNT composite film were immersed in the above solution, respectively. The in-situ polymerization was performed at room temperature for one hour with magnetic stirring (300 rpm). Afterward, the p-PP/CNT/PANI composite films were washed with DI water three times. After air drying, the composite films were cut into small pieces with the dimension of 8 mm by 12 mm. Finally, silver paint was coated on both sides of the specimen as an electrode material. The ratio of raw materials in the composites was calculated based on the weight percentage of p-PP, CNT, and PANI. The flow chart of the preparation procedure of p-PP/CNT/PANI film is illustrated in **Figure 3-1**.

3.2.4 Preparation of flexible mask sensor device

The inner layer of the disposable mask was cut by scissors, p-PP/CNT/PANI hybrid was pasted between the inner layer and the filter layer of the mask. Two wires were connected silver painting edges of the PP/CNT/PANI hybrid to the source meter, respectively. The schematic diagram is shown in **Figure 3-1a.** During the breath test, the tester wears the mask sensor device for short breath, long breath, and deep breath detection.

3.2.5 Gas-Sensing Measurements

To test the gas sensing properties, sensor samples were loaded into a test chamber connected with various gases controlled by mass flow controllers (MKS1179A, MKS Instruments, Andover, MA, USA), as shown in **Figure 3-2**. The different gases were introduced into the cylinder chamber to react with the sensor platform, and the resistance change was measured by a Kethley 2400 source meter. Before ammonia and CO gas sensing, the total gas flow was fixed at 100 sccm by combining two gases: pure nitrogen 80 sccm (MFC 1) and pure oxygen 20 sccm (MFC 2). When gas sensing, the total gas flow was fixed by combining three gases: pure nitrogen (MFC 1), pure oxygen (MFC 2), and 100 sccm of 106 ppm (C_{gas}) target gas diluted in nitrogen gas (MFC 3). The analyte concentration was calsulated by the following equation:

$$C_{analyte} = C_{gas} * MFC\ 3\ /\ (\ MFC\ 1 + MFC\ 2 + MFC\ 3) \qquad (1)$$

In this case, the concentration of ammonia ($C_{analyte}$) is about 50 ppm. For a 50 ppm concentration of acetone ($C_{analyte}$) gas sensing, 80 sccm of pure nitrogen (MFC 1), 20 sccm of pure oxygen (MFC 2), and 11 sccm of 500 ppm acetone diluted in nitrogen (MFC 3) were injected. For a 50 ppm methane gas sensing, 80 sccm of pure nitrogen (MFC 1), 20 sccm of pure oxygen (MFC 2), and 33 sccm of 200 ppm methane diluted in nitrogen (MFC 3) were injected. The bubbler was used to

generate analyte vapors (glycol, ethanol, ethylene glycol, isopropyl alcohol, and acetic acid). Synthetic air containing 80 sccm nitrogen and 20 sccm oxygen was continuously blown into the gas chamber. During bubbling, use a mass flow controller to divide 80 sccm of nitrogen into a carrier part and a dilution part. The gas carrier is bubbled through the liquid analyte of interest for target gas injection and then mixed with dilution air in the gas chamber. All operations were performed at room temperature (24 ± 1°C), and the data acquisition was controlled with a customized Labview program. The response of ammonia gas is defined as the normalized resistance change:

$$R = (R_g - R_0) / R_0 \tag{2}$$

Where R_g is the resistance of the sample after exposure to gas analytes, and R_0 is the initial resistance of the film in the ambient condition.
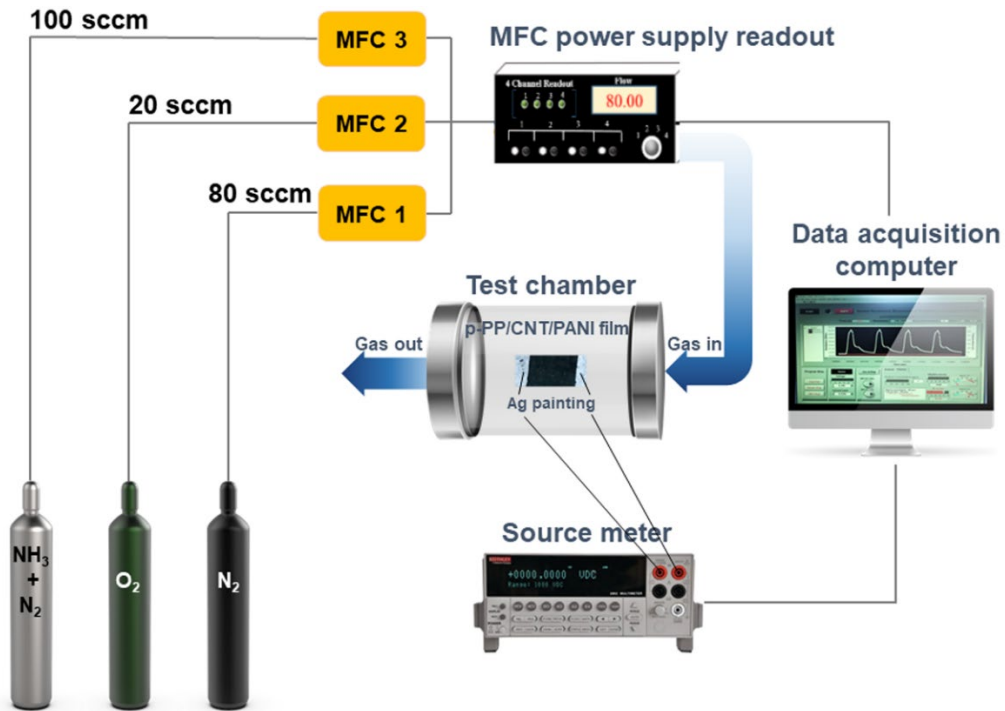
Figure 3-2. Schematic diagram of the gas sensing process.

3.2.6 Material Characterizations

The JEOL JSM-7000F scanning electron microscope (SEM) equipped with an energy dispersive spectrometer mapping (EDS-mapping) was used to examine the morphology of the composite film and qualitative elemental analysis, operated at an acceleration voltage of 20 kV.

The surface chemistry of the composite sensor was characterized by Fourier-transform infrared spectroscopy (FT-IR, Thermo Nicolet 6700). The spectra were recorded in the wavenumber ranging from 4000 to 400 cm^{-1} at a resolution of 4 cm^{-1}.

3.3 Results and discussion

3.3.1 Morphology and structure

The surface morphology of the p-PP, p-PP/CNT, p-PP/PANI, and p-PP/CNT/PANI films were characterized by SEM. As shown in **Figure 3-3a**, the pure p-PP sample consists of long-straight fibers with porous structure between different fibers. **Figure 3-3d** shows that the p-PP surface was evenly covered with a thin strip of CNT and exhibited relatively rough morphology compared with the pure p-PP sample. From **Figure 3-3b-c,** we can observe that a large amount of flocculent PANI uniformly covered the PP fibers. In **Figure 3-3e-f,** CNTs were coated with PANI nanoparticles, and noticeable pores appeared on the surface of the composite film. Compared with the p-PP/PANI film, the inter-connected p-PP/CNT/PANI network film with a large surface area and more voids can provide much more active adsorption sites, thereby promoting sensing properties [78]. To examine the dispersed state of the composite film, EDS mapping was conducted, and the results are shown in **Figure 3-3g-i**. It was found that the p-PP/CNT/PANI film contains three different elements. A large amount of C and N elements was observed in the composite film. In addition, a relatively small amount of chlorine was observed due to doping a small amount of Cl during the polymerization of the aniline monomer [62].

27
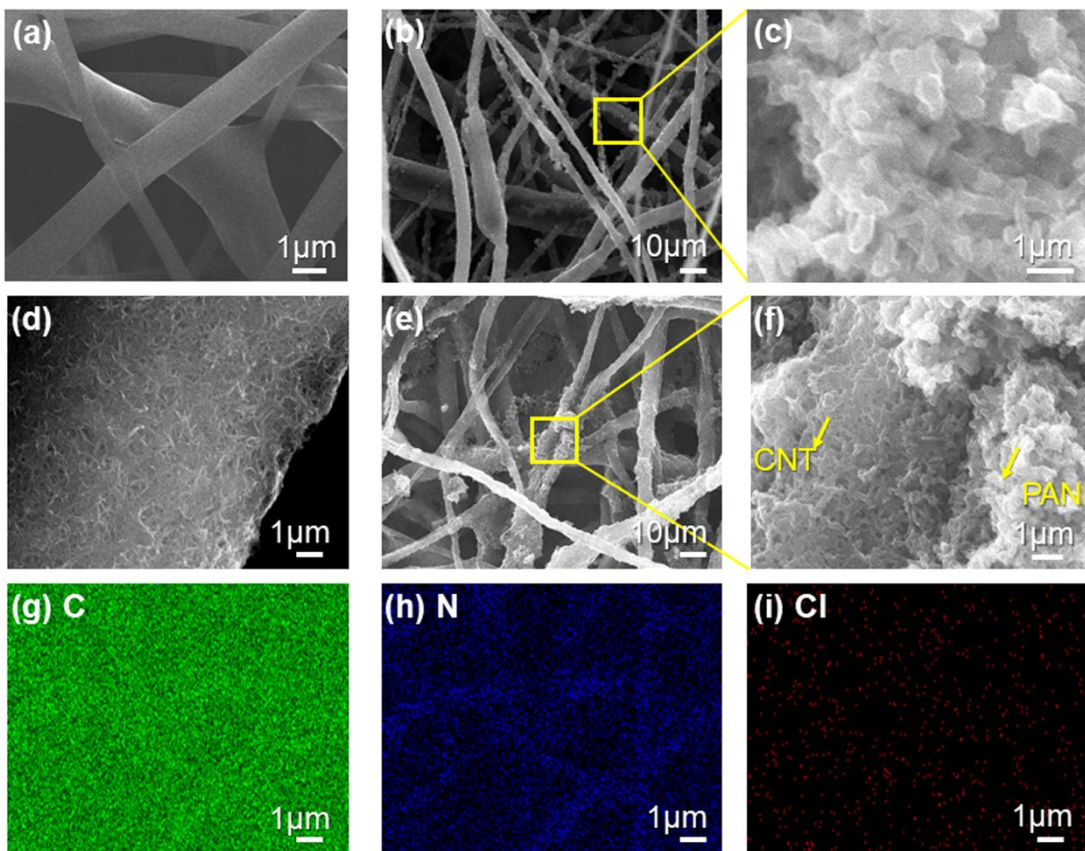
Figure 3-3. SEM images of (a) p-PP fibers, (b, c) p-PP/PANI (57:43) fibers, (d) p-PP/CNT (70:30) network, (e, f) p-PP/CNT/PANI (46:20:34) network, and (g, h, i) typical EDS elemental mapping of p-PP/CNT/PANI composite film.

FTIR spectra were further characterized to study the surface chemistry of the composites. As shown in **Figure 3-4**, all samples present polypropylene peaks. For the pure p-PP sample, the absorption peak located at 837 cm^{-1} represents C–CH$_3$ stretching vibration, the peaks at 989 cm^{-1} and 1160 cm^{-1} correspond to –CH$_3$ rocking vibration, the band at 1639 cm^{-1} is attributed to –CH$_3$ symmetric bending vibration and the peaks at 1452 cm^{-1}, 2830 cm^{-1}, 2916 cm^{-1} are attributed to –CH$_2$ symmetric bending, –CH$_2$ symmetric stretching and –CH$_2$ asymmetric stretching, respectively [79, 80]. For the p-PP/PANI sample, the band at 1560 cm^{-1} is due to C=C extension of

the quinoid ring, the peak at 1456 cm^{-1} represents the benzenoid ring, and the band at 1299 cm^{-1} is attributed to C−N stretching of the secondary amine, and the peak at 1129 cm^{-1} is due to in-plane bending of C-H [81]. For the p-PP/CNT/PANI composite, the absorption peaks centered at 1576 cm^{-1}, 1463 cm^{-1} and 1305 cm^{-1} can be attributed to the C=C stretching vibration of the quinoid ring, the benzenoid ring, and C−N stretch of the secondary amine in the PANI chains, respectively. The p-PP/CNT/PANI composite also presented the shift of these bands towards higher wavenumber compared with p-PP/PANI, indicating the interaction between CNT and PANI chain. The aromatic structure of PANI is expected to interact with the surface of the CNT via π-stacking [82, 83].These results confirmed the successful preparation of PP/CNT/PANI composite structures.
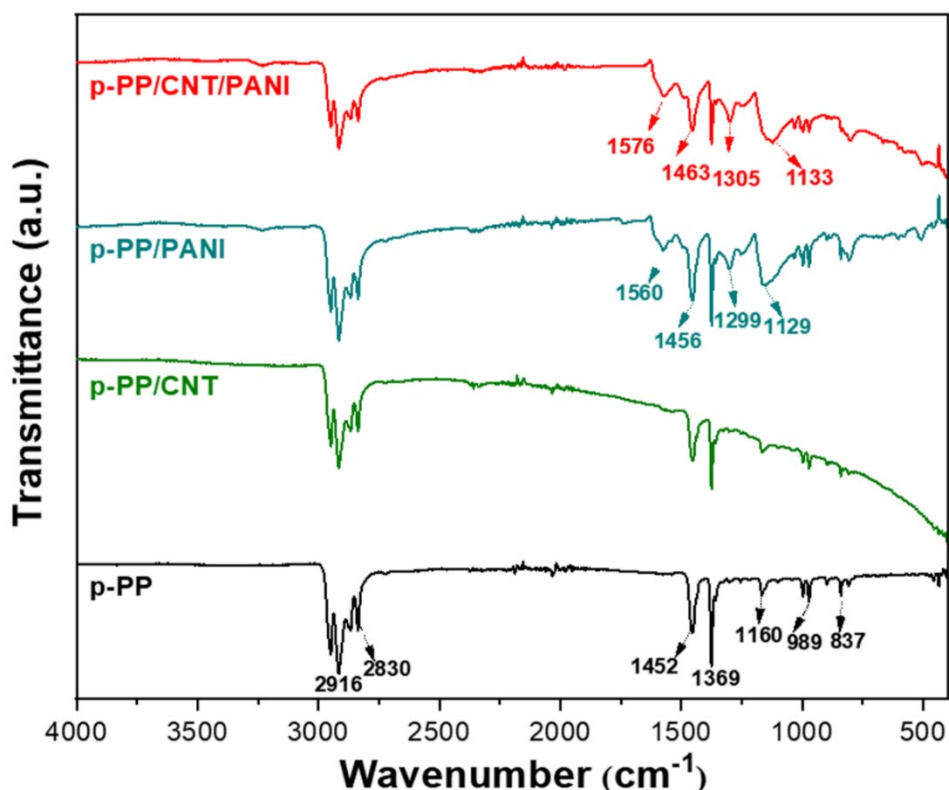
Figure 3-4. FTIR spectra of the p-PP, p-PP/CNT (70:30), p-PP/PANI (57:43), and p-PP/PANI/CNT (46:20:34) composite films.

3.3.2 Gas-sensing properties of p-PP/CNT/PANI composite sensor

The sensing performance of flexible p-PP/CNT/PANI composites was characterized under various NH$_3$ concentrations at room temperature. The effects of CNT concentrations incorporated into PANI on sensing properties were examined in **Figure 3-5**. As shown in **Figure 3-5a**, the CNT film sensor does not show the resistance change towards ammonia gas, proving that CNT alone does not respond to ammonia gas. With the increasing content of PANI in CNT/PANI composites, the resistance change towards ammonia gas increases. As shown in **Figure 3-5b**, the p-PP/PANI film has the lowest resistance change to ammonia gas. With the content of CNT increasing, the resistance change towards ammonia gas improves gradually. When the concentration of CNT is 0.5 mg/mL, the sensing response can be achieved as high as 452%. However, as CNT concentrations exceed 0.5 mg/mL, too many CNTs are accumulated on the composite surface, which may have negative effect on the sensing response value. In addition, the composite sensor with 0.5 mg/mL CNT and 1.7 mg/mL PANI is further investigated at different NH$_3$ gas concentrations. As shown in **Figure 3-5c**, the increase of NH$_3$ concentration from 500 ppb to 70 ppm resulted in a gradual increase of the resistance change, while the response time gradually decreased. After the NH$_3$ is introduced, the resistance falls back to the original state with little baseline drift, indicating a typical p-type semiconducting behavior of p-PP/CNT/PANI composite film and good reversibility of the sensor. As shown in **Figure 3-5d**, the response of the composite sensor shows a good linear relationship with NH$_3$ concentrations. **Figure 3-5e** shows the cycling test of the resistance change for the flexible sensor towards 70 ppm NH$_3$. The result suggests the sensor has good repeatability with a relatively fast response time (93 seconds) and recovery time (36 seconds).

Selectivity is a significant parameter of gas sensors, determining whether the sensor can be used in complex atmospheric environments. Therefore, various interfering gases , CO_2, CO and volatile organic compounds (VOCs), including acetone, methane, glycol, ethanol, ethylene glycol, isopropyl alcohol, and acetic acid, were examined for the selectivity evaluation of the p-PP/CNT/PANI sensor. The response and resistance change of the gas sensor towards 50 ppm CO_2 and CO are shown in **Figure3-6a**. The response values of the composite sensor toward the various gases are presented in **Figure 3-5f**. The p-PP/CNT/PANI sensor has the highest response to NH_3, which is at least 20 times higher than other interfering gases, proving that the flexible p-PP/CNT/PANI sensor has excellent selectivity on ammonia gas at room temperature.
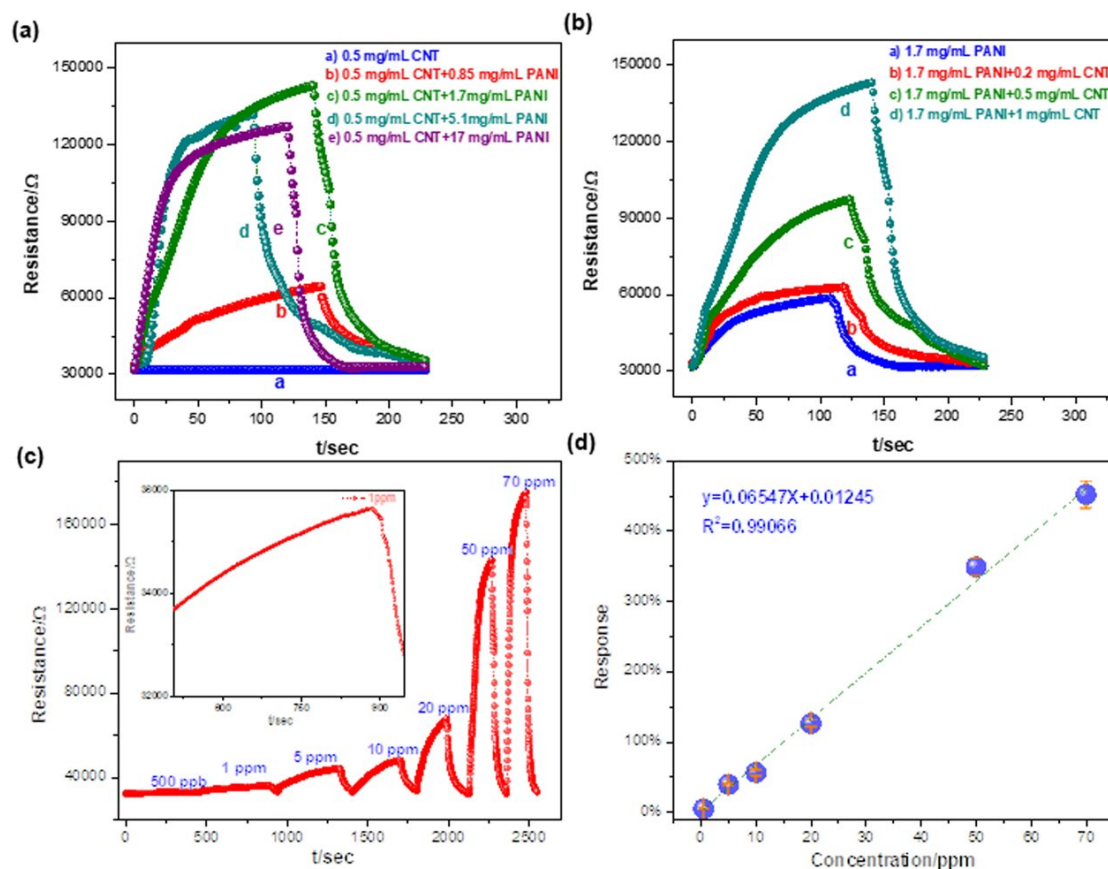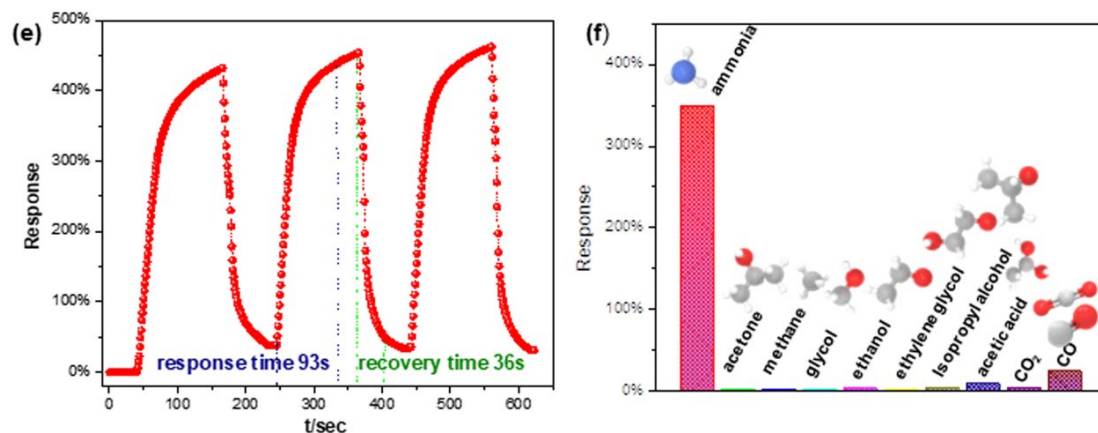
Figure 3-5. (a) 0.5 mg/mL CNT with varying concentrations of PANI film sensor towards 50 ppm NH$_3$. (b) 1.7 mg/mL PANI with varying concentrations of CNT film sensor towards 50 ppm NH$_3$. (c) Dynamic resistance changes of flexible p-PP/CNT/PANI (0.5 mg/mL CNT, 1.7 mg/mL PANI) composite sensor. (inset shows the resistance change towards 1 ppm NH$_3$ in detail) (d) Sensor response as a function of ammonia gas concentration. (e) The sensing cycling test for p-PP/CNT/PANI composite at 70 ppm NH$_3$. (f) Selectivity study to 50 ppm NH$_3$,CO$_2$, CO and volatile organic compounds for the flexible p-PP/CNT/PANI sensor at room temperature, the humidity of the test chamber is 18%-24%.

In order to investigate sensing properties of wearability and flexibility of sensors in breathing environments, the effects of temperature, humidity and bending states of the p-PP/CNT/PANI composites on the sensing response towards NH$_3$ were summarized in **Fig 3-6**. The effect of different temperatures on sensing response is shown in **Figure 3-6a**, with the increase in temperature, the sensor response presented a stepwise increase trend due to the improved ammonia gas absorption and desorption process at a higher temperature[84]. The initial resistance change of the p-PP/CNT/PANI sensor in the air around room temperature is shown in **Figure 3-6b**. The sensor response as a function of operating temperature towards NH$_3$, indicating the 1℃ temperature change has a smaller effect on sensor signal than 1 ppm of ammonia concentration change. The resistance change of the p-PP/CNT/PANI sensor under 0-80% RH circumstances in the air was observed in **Figure 3-6c**. The resistance will decrease with an increase the humidity

32

due to the further protonation of PANI through absorbed water or the generation of hydrogen ions [85, 86]. However, the resistance of the p-PP/CNT/PANI sensor will increase with the increase of humidity when exposing 10 or 70 ppm NH_3, as shown in **Figure 3-6, c, d.** This was attributed to the water adsorption leading to the PANI swelling, chains distorting, and an increase in disorder at high humidity, which improves the resistance [87]. Moreover, the sensing response to various concentrations of ammonia in different humidity was compared in **Figure 3-6e**, suggesting the influence of humidity under high concentrations of ammonia is larger than under low concentrations. Nevertheless, the 1% RH change has a much smaller effect on sensor signal than 1 ppm of ammonia concentration change.

The long-term stability of the sensor in the period of continuous 20 days in the air and target gas at room temperature were shown in **Figure 3-6f**. The p-PP/CNT/PANI sensor has demonstrated a stable resistance or response for 20 days, indicating the excellent stability. The resistance change of the p-PP/CNT/PANI sensor at different bending angles is shown in **Figure 3-6g.** The response of the p-PP/CNT/PANI sensor under different bending states is observed in **Figure 3-6h**. The response value of the p-PP/CNT/PANI sensor has an only slight increase with the increase of bending angles, suggesting the excellent flexibility of the composite sensor. Finally, the sensing properties of the developed p-PP/CNT/PANI composite sensor were compared with other flexible ammonia sensors, and the results are shown in **Table 3-1**. The p-PP/CNT/PANI sensor exhibits excellent ammonia sensing performance and can be used for respiratory rate detection.
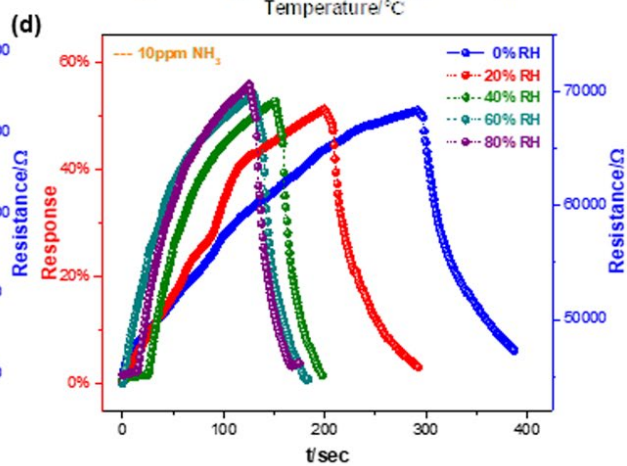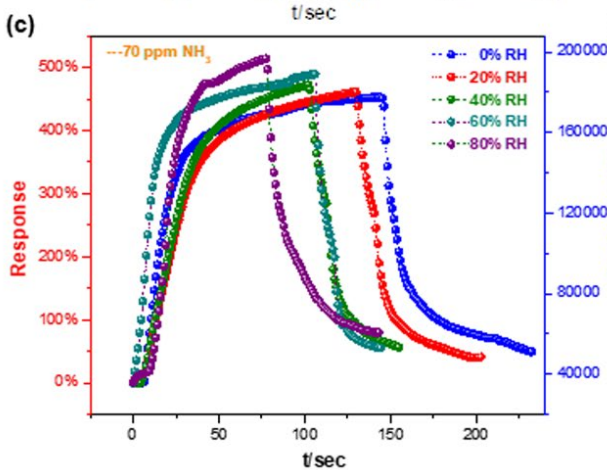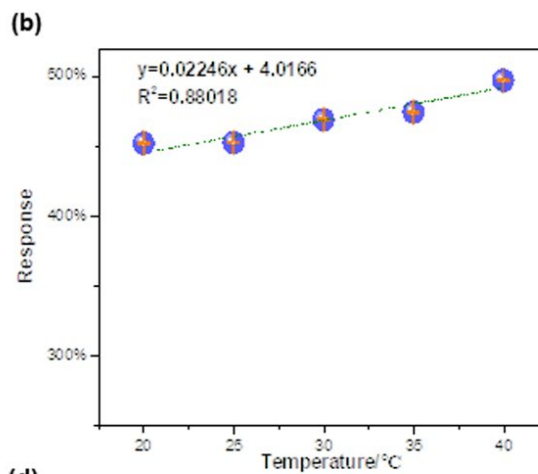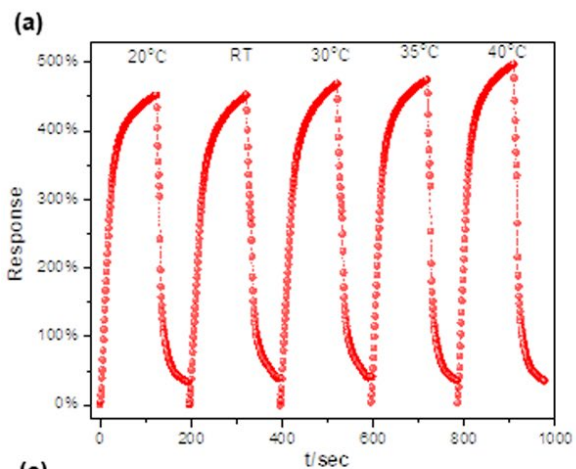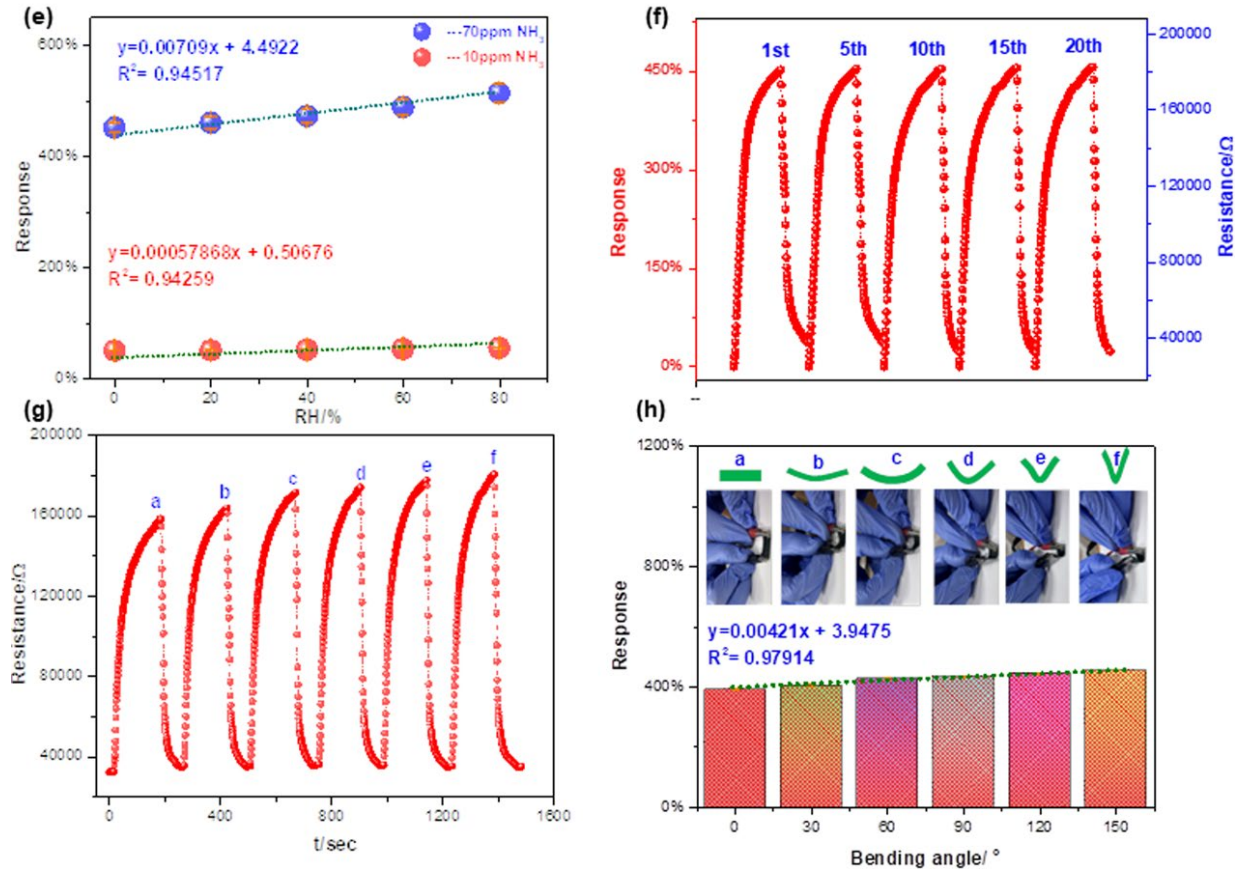
Figure 3-6. The effect of different temperature, humidity conditions, and bending states on sensor response towards NH$_3$ gas. (a) The response of the p-PP/CNT/PANI sensor under 20-40°C towards 70 ppm NH$_3$ at different temperatures, RT is room temperature. (b) Sensor response as a function of operating temperature. (c) The response and resistance change of the p-PP/CNT/PANI sensor under 0-80% RH circumstance towards 70 ppm NH$_3$ at room temperature. (d) The response and resistance change of the p-PP/CNT/PANI sensor under 0-80% RH circumstance towards 10 ppm NH$_3$. (e) Sensor response as a function of humidity towards 10 ppm and 70ppm NH$_3$ at room temperature. (f) Long-term stability of the sensor in the period of continuous 20 days towards 70 ppm NH$_3$ at room temperature. (g) Resistance change of the p-PP/CNT/PANI sensor under 70 ppm of NH$_3$ at different bending angles, a-f represent 0, 30, 60, 90, 120, and 150 bending angles, respectively. (h) Response of the p-PP/CNT/PANI sensor under 70 ppm of NH$_3$ at different bending states at room temperature.

Table 3-1. Comparison of sensing performance for the PANI-based flexible gas sensors synthesized in this work and some other previously reported.

Ref	Substrate	Response value	Testing gas	Res /Rec Time	Studied Detection Range	Sensing Materials	RT	Flexible
1	PET	0.25 (50ppm)	NH_3	85/50s	5-1000ppm	PANI	√	√
2	fabric	0.40 (8ppb)	NH_3	/	1-8 ppb	PANI/ fabrics	√	√
3	PET	0.26 (100ppm)	NH_3	19s/36s	10-100ppm	PANI	√	√
4	PET	25 (50 ppm)	NH_3	85/20s	0.2-50 ppm	PANI/MWCNT	√	√
5	fabric	0.62 (20 ppm)	NH_3	9/30s	0.2-100 ppm	PANI/MWCNT	×	√
6	PET	1.17 (50 ppm)	NH_3	47/60s	30-100 ppm	PANI/MWCNT	√	√
7	PVDF	0.32 (1ppm)	NH_3	76/26s	0.2-1ppm	PANI/MWCNT - PVDF	√	√
This work	p-PP	4.52 (70ppm)	NH_3	93s/36s	0.5-70ppm	PANI/MWCNT	√	√

3.3.3 Sensing mechanism of p-PP/CNT/PANI composite sensor

Polyaniline is a well-known p-type semiconductor in the form of emeraldine salt [2, 30]. NH_3 molecule acts as a dopant for PANI. When the ammonia gas is introduced, the ammonia molecules react with the N-H group of PANI to form NH_4^+ and cause the localization of the polaron of PANI. Thereby, the conductivity of the composite material is reduced. The reaction process is shown in **Figure 3-7a**. Upon pausing the flow of ammonia, emeraldine salt form was recovered by

desorption of adsorbed NH_3 molecules. The reversible reaction proceeded to the left, and the NH_4^+ decomposed into NH_3 and protons, restoring conductivity, and the PANI became doped.

The sensing mechanism of NH_3 molecules on p-PP/CNT/PANI film was illustrated in **Figure 3-7b**. Firstly, the p-PP/CNT/PANI composite film shows a relatively high surface area compared to the p-PP/PANI film (as indicated in the SEM results), which is helpful to NH_3 adsorption corresponding to enhanced sensing response. Secondly, the p-PP/CNT/PANI composite film has a unique interconnected network worked as efficient sensing channels to promote charge transfer efficiency. Besides, the p-PP/CNT/PANI film has a porous structure, which means the film has sufficient space for easy penetration of gas molecules and more adsorption sites to improve sensing performance [88].
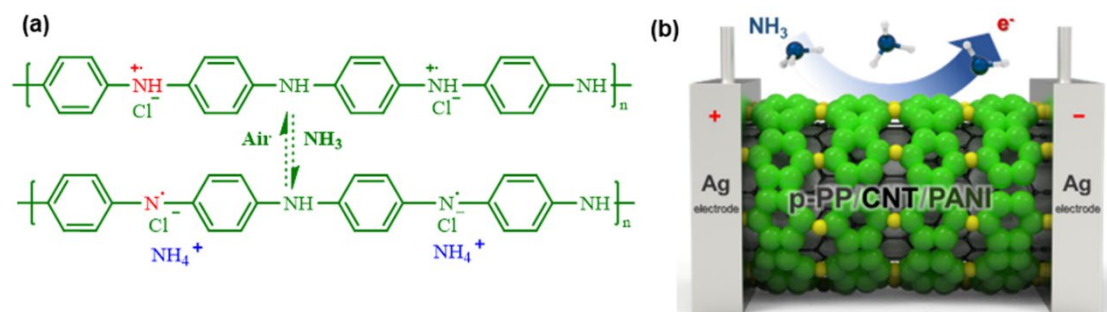
Figure 3-7. (a) The protonation and deprotonation process of PANI. (b) The proposed gas sensing mechanism of p-PP/CNT/PANI composite.

3.3.4 Wearable and flexible Sensor and breath monitoring

Respiratory rate detection was investigated for potential monitoring of breathing-related health issues. As shown in **Figure 3-8a**, we designed a wearable breath sensor by integrating the p-PP/CNT/PANI film into a disposable surgical mask. As shown in **Figure 3-8b,** breaths with different durations and intensities influence the signals with different shapes and responses. When the p-PP/CNT/PANI composite sensor detects short breaths at room temperature, the response

value is only about 1.6%. However, during a long or deep breath, the response value can be raised to 3.2% or 5.0%, respectively. We studied 1 ppm of ammonia concentration change, 1°C temperature change, 1% RH change, and 1° bending angle change have effect on sensor response, the slopes of factors were 0.06547, 0.02246, 0.00058, 0.00421, respectively. So the ammonia gas concentration is the most important factor in response signal compared with other factors. Besides, according to Figure S1c, the extremely high humidity (90% RH) must have a huge effect on resistance change. Therefore, the breath signal may mainly cause by water and ammonia. The higher intensity of breathing, the higher humidity (for breath analysis, the relative humidity condition >90%RH), which leads to less resistance of the mask sensor, and different curves can be observed. It should be noted that the curves went down with time, this is due to too many water molecules getting adsorption on the mask sensor and they cannot be desorbed in a short time. In addition, all breath tests of different durations and intensities exhibit fast response (only several seconds) and recovery time. These results demonstrate that the p-PP/CNT/PANI sensor can be used for real-time respiratory rate detection, showing great potential for human health monitoring applications.
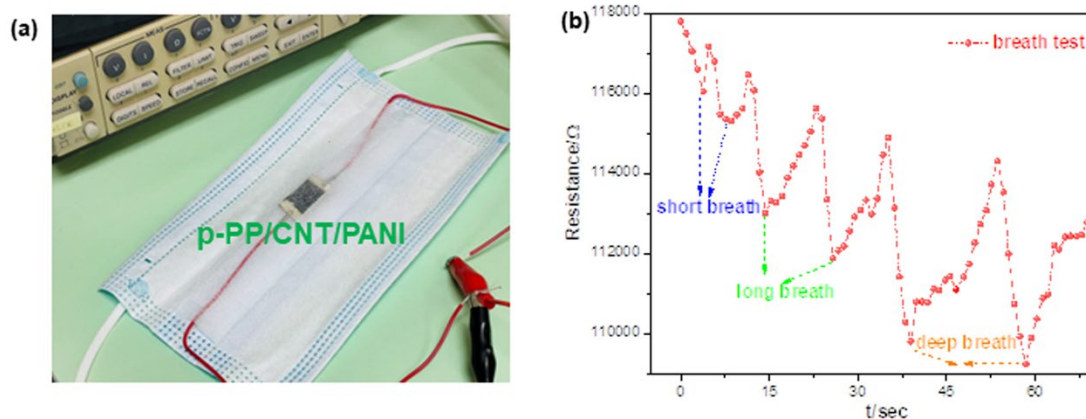
Figure 3-8. (a) Photograph of wearable breath sensor devise. (b) The Resistance-time curve of the human breath test.

3.4 Conclusion

This work used disposable masks as flexible substrates to fabricate p-PP/CNT/PANI gas sensors for ammonia detection and breath monitoring. The fabricated sensors exhibited good sensitivity ranging from 500 ppb to 70 ppm, fast response/recovery time, room temperature operation, reliable flexibility and stability, and excellent selectivity to NH_3 compared to other VOC gases. The excellent sensing performance of the p-PP/CNT/PANI composite sensor is mainly attributed to the p-PP/CNT/PANI interconnected network, which provides an improved relatively specific surface area and efficient sensing channels to facilitate charge transport. Furthermore, the demonstrated simple and real-time human breath testing device based on the p-PP/CNT/PANI composite film shows a potential application for health assessment.

Chapter 4 Graphene/PANI functionalized mask sensors for ammonia and volatile sulfur compounds detection

4.1 Introduction

Breath analysis is becoming a vital non-invasive diagnostic method for assessing human health conditions. Recently, monitoring COVID-19 through breath analysis was reported [25]. Human exhaled breath contains nitrogen, oxygen, carbon dioxide, water, and thousands of trace gases [23]. Their changes in the content of different trace gases correspond to specific pathologies [89]. Among them, volatile sulfur compounds (VSCs), including methyl mercaptan (CH_4S), dimethyl sulfide (C_2H_6S), and hydrogen sulfide (H_2S), are vital markers for the detection of halitosis related to periodontal disease and kidney failure [29, 90]. The concentration of VSCs in the exhaled breath of patients with halitosis can range at ppm level [91]. In addition, ammonia (NH_3), one of the trace gases in exhaled breath of humans, can be used as a typical biomarker for specific diseases and is often used in non-invasive clinical diagnosis, such as end-stage renal disease (ESRD) monitoring [27], detection of pylorus helicobacter [36], diagnosis of hepatic encephalopathy [92], etc. According to the Occupational Safety and Health Administration (OSHA), the minimum amount of NH_3 found to be irritating to the most sensitive individuals' eyes, throat, skin, and respiratory tract is 50 ppm [85]. Moreover, the concentration of NH_3 in human breath gas is deficient, approximately 400–2000 ppb for healthy individuals and 800–15000 ppb for ESRD patients [24]. Traditionally, various techniques such as gas chromatography (GC), mass spectrometry (MS), and selected ion flow tube mass spectrometry (SIFT-MS) can be utilized for breath monitoring [32, 93]. However, these methods are unsuitable for portable and real-time monitoring of low-concentration gases due to complex processing, high price, bulky size, and long analysis time. Therefore, it is urgent and significant to

develop a simple, real-time, portable device with high sensitivity, the low detection limit for VSCs and ammonia analysis in exhaled breath and health assessment.

In the past decade, metal oxide semiconductors (MOSs) such as SnO_2, ZnO, WO_3, and MoO_3 have been used as sensing materials for NH_3 or VSCs gas sensors [94-96]. Nevertheless, MOS-based sensors have obvious drawbacks of high operating temperature (100-300°C), high energy consumption, and rigid and brittle nature [97]. In recent years, the development of flexible and room temperature gas sensors has become a research hotspot. Carbon-based nanomaterials, graphene oxide (GO), and carbon nanotube (CNT), have been investigated for gas sensors due to their unique electrical, physical, chemical properties and excellent stability, but the interference from humidity and long recovery limit the performance [13, 98, 99]. Conducting polymers, such as polyaniline (PANI) [100, 101], polypyrrole (PPy) [8, 16, 102], and poly(3,4ethylenedioxythiophene) (PEDOT) [4], have also attracted extensive attention in the development of flexible gas sensors, in light of the facile synthesis process, excellent electrical properties, mechanical flexibility, good biocompatibility, inherent compatibility with polymer substrates, unique protonation and deprotonation processes. Among them, PANI shows promising properties for preparing flexible NH_3 sensors. Nevertheless, pure PANI still suffers from several disadvantages, such as poor long-term stability, slow response time, and prolonged recovery time [103]. Therefore, PANI-based composites, such as PANI/SnO_2, PANI/WO_3, PANI/rGO, and PANI/CNT, have been investigated for NH_3 sensing applications [104-107]. Fan et al. [61] demonstrated a room temperature PANI/WO_3 composite sensor via in-situ polymerization assisted by an ultrasonic spray method. The PANI/WO_3 sensor presented a 10 times higher response to NH_3 gas than the pure PANI sensor. Guo et al. [108] prepared a hierarchically nanostructured PANI/rGO composite sensor using polyethylene terephthalate as substrate. The hybrid sensor exhibited over five times higher response than the pristine PANI sensor towards 100

ppm NH_3 gas with reliable transparency (90.3% at 550 nm) and fast response/recovery time.

It is worth noting that disposable masks, mainly made up of polypropylene (PP) fibers, could be potential flexible substrates for gas sensors. The Journal of Environmental Science and Technology estimated that 129 billion masks are used and discarded each month globally during the COVID-19 pandemic [43]. However, disposable masks are not biodegradable, which will cause severe environmental damage to the ecosystem and its inhabitants after incorrect disposal. In the past three years, there have been several reports of using waste disposable masks for microwave absorption [44], desalination of seawater [109], and antibacterial materials [46]. However, to our best knowledge, there is no report of using waste masks for gas sensors in well-known journals.

Herein, for the first time, we fabricated a flexible PP/G/PANI hybrid gas sensor through dip-coating and followed in-situ polymerization using a waste disposable mask as a flexible substrate. The PP/G/PANI hybrid sensor exhibits excellent sensitivity and selectivity towards ammonia gas, fast sensing response/recovery time, long-term stability, and ppb-level detection limit. Moreover, comparing the different signals in the exhaled breath of the tested volunteer before and after ingesting raw garlic, we found that the PP/G/PANI sensor can be used to detect the VSCs in the exhaled breath at room temperature, showing the potential application for developing an odor sensing system for detecting malodorous gases in exhaled breath for kidney disease diagnosis.
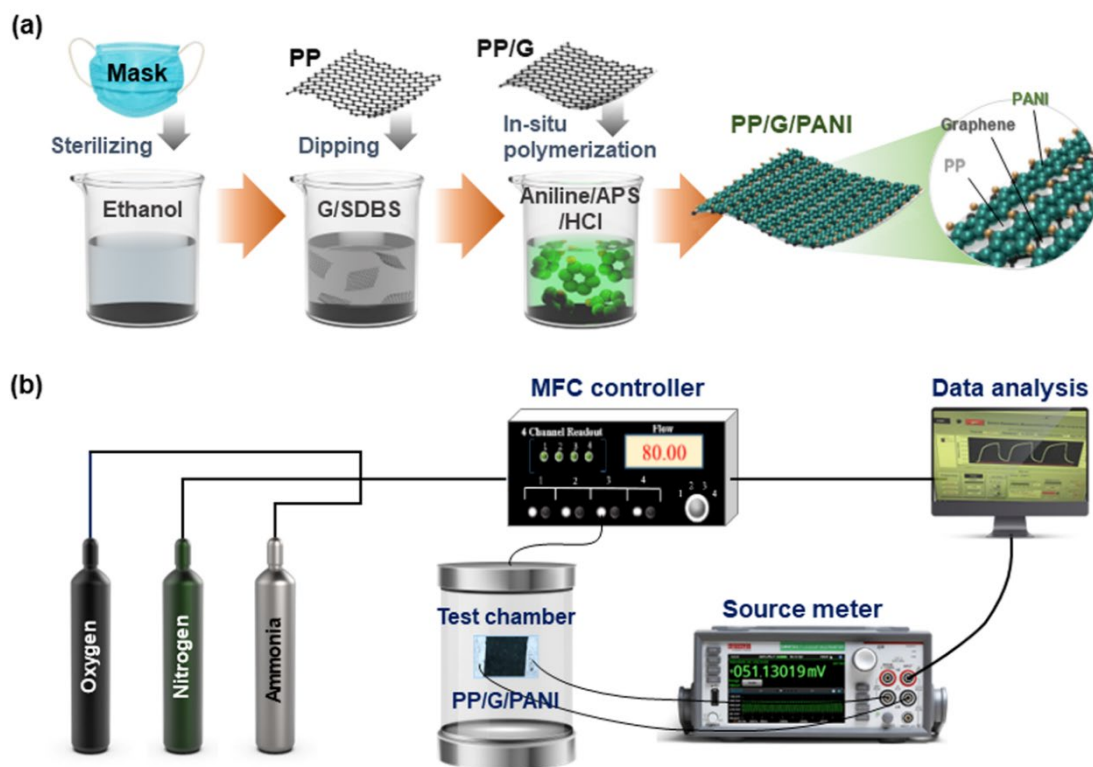
Figure 4-1. (a) Schematic illustration of the flexible PP/G/PANI hybrid sensor preparation process. (b) The scheme of gas sensing testing system.

4.2 Experimental section

4.2.1 Materials

Disposable masks were obtained from Jiangsu Excellence Medical Supplies Company (Changzhou, Jiangsu, China). The filter layer (denoted as PP, after a simple steam and ethanol treatment) of the waste disposable mask was used in this study. Ammonium persulfate (APS), 36.5%-38% hydrochloric acid, sodium dodecyl benzene sulfonate (SDBS), and aniline monomer were purchased from Sigma-Aldrich, USA., Graphene nanoplatelets aggregates (Z04G007) and Tedlar bags were purchased from Alfa Aesar, USA, and sliver painting was purchased from VWR (127185-15G).

4.2.2 Fabrication of PP/G composite

Graphene aqueous solutions were prepared by mixing 0.15 g graphene nanoplatelets aggregates with 30 mL DI water. SDBS with 0.15 g was added to the suspension to enhance graphene dispersion [76, 77]. Then, the graphene suspension was treated by ultrasound (351OR-MTH, 330W) for 30 min. Finally, the PP film was socked in the prepared graphene suspension for 3 h. After air drying, the PP film was soaked in the graphene suspension again for fabrication of the PP/G composite.

4.2.3 Materials Fabrication of PP/G/PANI composite

Aniline monomer with 0.4 mL was added into 200 mL 1 M HCl aqueous solution in a beaker (300 mL). A 0.46 g portion of APS was dissolved in precooled 1 M HCl solution (40 mL), and then the APS-HCl solution was poured into the monomer-HCl suspension. The solution was shaken for less than 1 min and left at room temperature. Afterward, the PP sample and PP/G hybrid sample were soaked in the above mixed suspensions, respectively. The in-situ chemical polymerization was stirred magnetically at 25°C for 60 min. The PP/PANI and PP/G/PANI hybrid films were washed four times with DI water to remove the excess amount of hydrochloric acid and dried in an oven at 30 °C for 8 h. The hybrid film was cut into 10 mm*10 mm and doped with silver painting on both sides to decrease the connect resistance. The fabrication process of PP/G/PANI composite film is shown in **Figure 4-1a**.

4.2.4 Gas-Sensing Measurements

The sensor samples were loaded into a closed chamber connected with various gases controlled by a mass flow controller (MKS1179A, MKS Instruments, Andover, MA, USA), as shown in **Figure4-1b**. The target gases were introduced into the test chamber to react with the sensor platform, and the change of resistance was detected by Kethley 2400 source meter. Before gas

sensing, the total gas flow was fixed at 80 sccm nitrogen (MFC 1) and 20 sccm oxygen (MFC 2). When gas sensing, the total gas flow was fixed by combining all the mass flow controllers: MFC 1, MFC 2, and 100 ppm of ammonia (methane, hydrogen sulfide gas) diluted in nitrogen gas (MFC 3). A bubbler generated vapors of volatile organic compounds (acetic acid, acetone, ethanol, methanol, and benzene). A hygrometer was used to measure the humidity in the test chamber. The gas humidity was precisely controlled using the programmable MFC where carrier nitrogen gas passes through a bubbler. All operations were carried out at room temperature (24.5±1°C) under atmospheric conditions, and the data acquisition was controlled with a customized Labview program [75, 110]. The sensor response of the sample was calculated from the normalized resistance change:

$$R = (R_g - R_0)/R_0 \hspace{5cm} (1)$$

where R_0 and R_g are the initial resistance of the sample in the ambient condition and the resistance of the sample after exposure to the target gas, respectively.

4.2.5 Sensing of VSC contained in expired breath before and after ingesting raw garlic

The fresh breath of a healthy volunteer was exhaled into a 1 L Tedlar bag sealed tightly around the mouth as a baseline sample. Afterward, the volunteer was asked to ingest 1.0 g of raw garlic, and his exhaled breath was collected in a Tedlar bag after 10 minutes for sensor tests. Exhaled gas was passed through two drying tubes filled with anhydrous calcium sulfate to reduce the interference of high humidity on sensor results.

4.2.6 Material Characterizations

The morphology and qualitative elemental analysis of the samples were characterized by a scanning electron microscope (SEM, JEOL JSM-7000F, USA) equipped with an energy dispersive spectrometer mapping (EDS-mapping) at acceleration voltage of 20 kV. The surface chemistry of

the testing samples was examined using Fourier-transform infrared spectroscopy (FT-IR, Thermo Nicolet 6700). The spectra were recorded in the wavenumber range from 2000 to 400 cm^{-1}.

4.3 Results and discussion

4.3.1 Morphology and structure

The morphology of PP, PP/G, PP/PANI, and PP/G/PANI samples were observed by SEM, and the results are shown in **Figure 4-2**. The pure PP film displays straight fibers with a smooth surface. From **Figure 4-2b,** we can see that the graphene particles are aggregating on the PP fibers. As shown in **Figure 4-2c**, a large amount of flocculent PANI uniformly covered the PP surface. In **Figure 4-2d**, it can be found that lots of graphene particles are surrounded by PANI, suggesting good chemical bonds between graphene and PANI polymer molecules. In addition, the PP/G/PANI hybrid exhibited a porous network structure, which can effectively improve specific surface area to promote gas adsorption of target gas molecules, thereby improving the sensing performance [107].
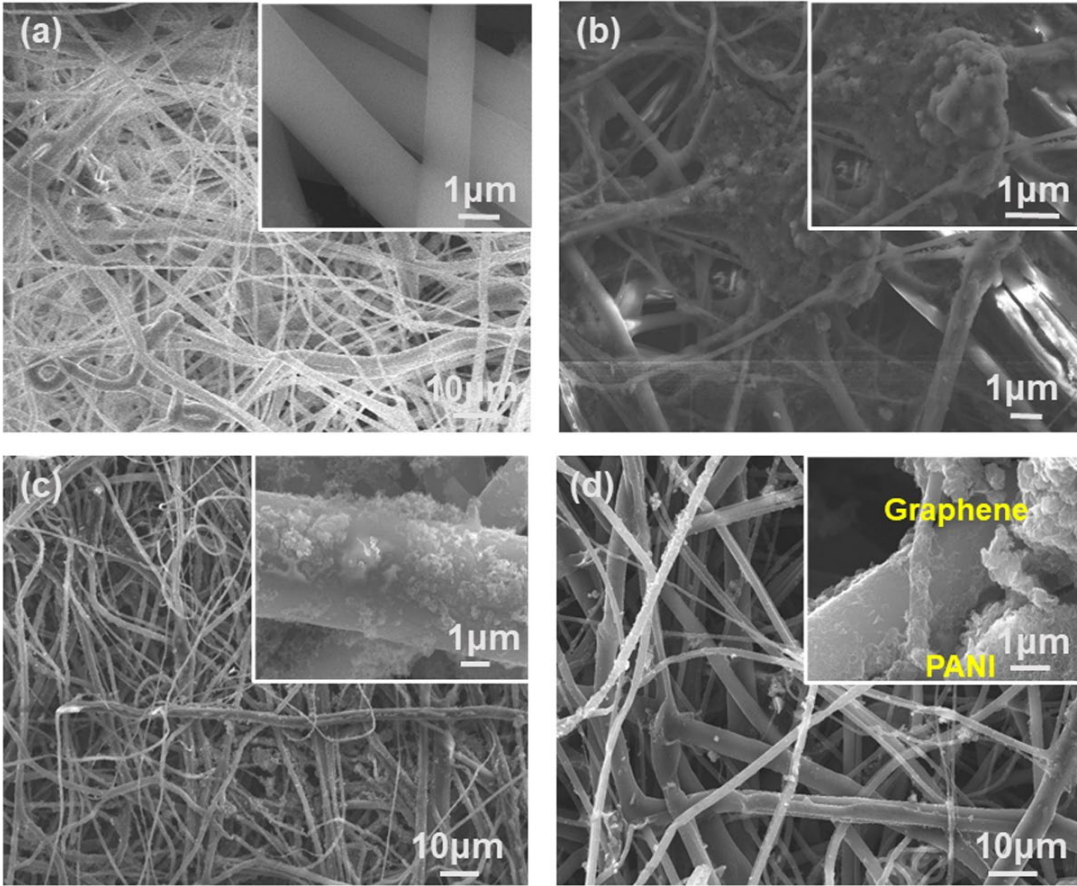
Figure 4-2. SEM images of (a) PP film, (b) PP/G film, (c) PP/PANI network, (d) PP/G/PANI network.

To explore the dispersed state of the surface elements in the PP/G/PANI hybrid, the EDS mapping characterization was performed, and the results are shown in **Figure 4-3**. It can be observed that the PP/G/PANI hybrid contains three different elements. A large amount of carbon and nitrogen elements were found in the composite film. Besides, a small amount of chlorine was also detected, which indicated that the chlorine element was doped during the in-situ polymerization process of PANI [62].
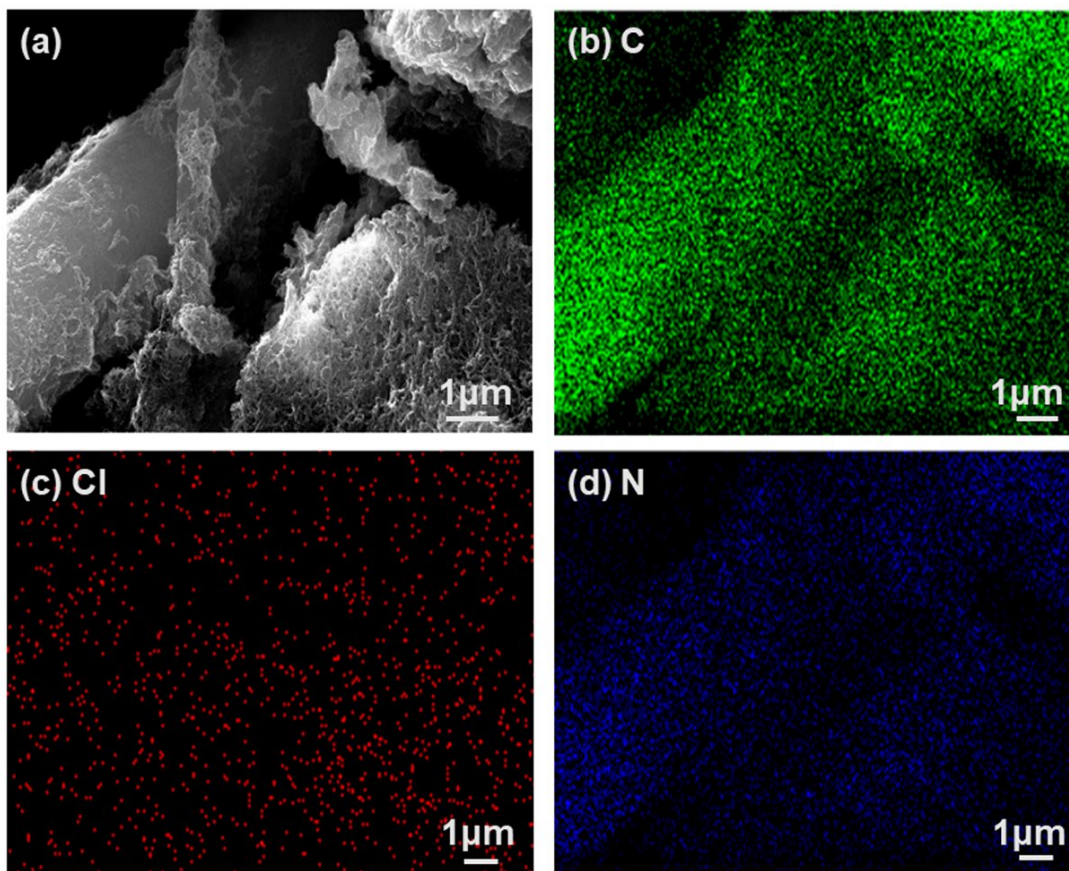
Figure 4-3. EDS-mapping of PP/G/PANI hybrid network. (a) Magnetified SEM of **Figure 4-2d**. (b, c, d) Distribution of C, N, and Cl elements.

To examine the change in surface chemistry, the functional groups of hybrid samples were confirmed by FTIR as shown in **Figure 4-4**. All four samples present pronounced polypropylene peaks. For a pristine PP film, the characteristic peak located at 847 cm^{-1} corresponds to C–CH$_3$ stretching vibration. The bands at 969 cm^{-1} and 1160 cm^{-1}, 1639 cm^{-1}, and 1452 $cm^{-1}$are are attributed to –CH$_3$ rocking vibration, –CH$_3$ symmetric bending vibration, and –CH$_2$ symmetric bending, respectively [79, 80]. The prominent characteristic peaks of PP/PANI are described below: absorption peak at 1537 cm^{-1} (C=C stretch of the quinoid ring), 1453 cm^{-1} (benzenoid ring), demonstrating the emeraldine form as an oxidation state of PANI. The peak was at 1300 cm^{-1}

(C−N stretch of the secondary amine), and 1163 cm^{-1} (in-plane bending of C-H). For PP/G/PANI composite film, the main absorption peaks centered at 1301 cm^{-1}, 1460 cm^{-1} and 1540 cm^{-1} can be ascribed to the C−N stretch of the secondary amine, the benzenoid ring, and the C=C stretching vibration of the quinoid ring, respectively. These characteristic peaks prove that the PP/G/PANI hybrid has been successfully prepared.
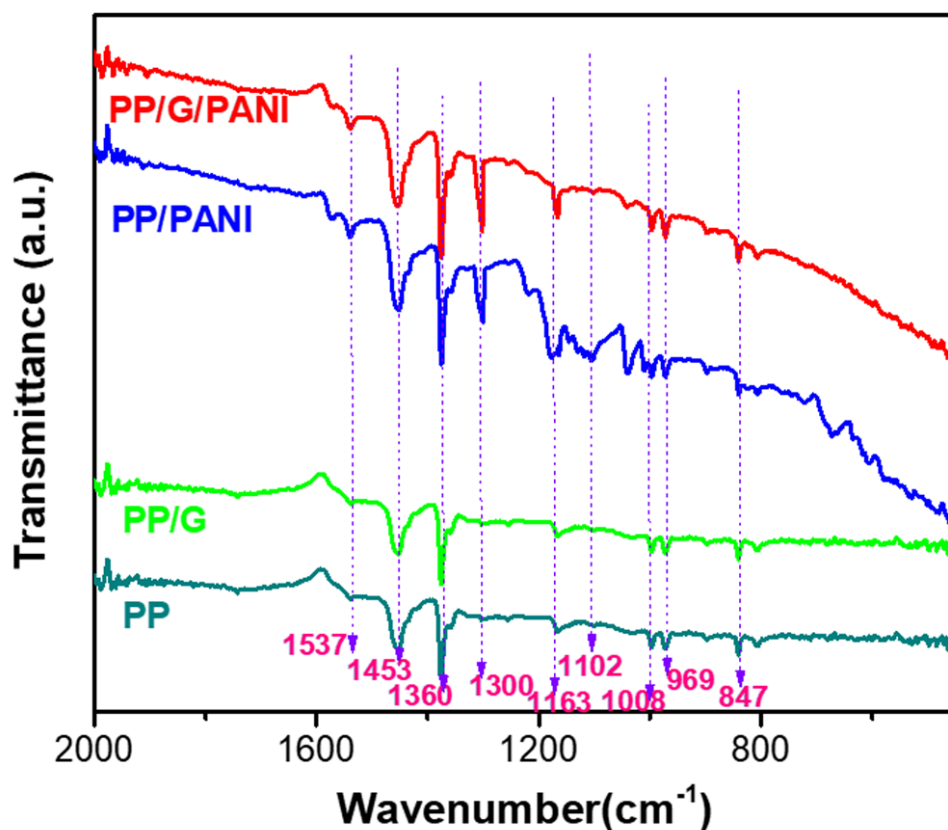
Figure 4-4. FTIR spectra of the PP, PP/G, PP/PANI, PP/G /PANI hybrids.

4.3.2 Gas sensing performance of flexible composite films

The sensing performance of the flexible gas sensors based on PP/G, PP/PANI, and PP/G/PANI hybrid sensors were measured at room temperature. **Figure 4-5a** presents the dynamic response-recovery curves of the PP/G, PP/PANI, and PP/G/PANI hybrid sensors towards various NH$_3$

concentrations ranging from 100 ppb to 75 ppm at room temperature. There was almost no sensing response for the PP/G film due to no reaction between graphene and NH_3 molecules. When the PP/PANI and PP/G/PANI hybrid sensors showed the noticeable response at a higher concentration than 1 ppm. However, the PP/G/PANI hybrid sensors showed obvious response at low concentration of ppb range. The PP/G/PANI hybrid sensor exhibited higher response values than the PP/PANI sensor at all concentrations (for example, the response of the PP/G/PANI hybrid sensor is 250% towards 50 ppm NH_3, which is four times higher than that of the PP/PANI sensor). These results imply that combining PANI with graphene was an effective strategy to improve the sensor response. The response-concentration fitting curves of the PP/G/PANI hybrid sensor as depicted in **Figure 4-5b**. The sensor exhibited outstanding linearity from 100 ppb to 75 ppm.

Selectivity is a critical parameter for evaluating gas sensor performance for practical applications. Therefore, the selectivity of the PP/G/PANI hybrid sensor was characterized by comparing the response to various gases, including NH_3, H_2S, acetic acid, acetone, ethanol, methanol, benzene, and methane. It was evident from **Figure 4-5c** that the PP/G/PANI hybrid sensor exhibited strong specific adsorption of NH_3. The response value for NH_3 gas was at least 30 times higher than other detection gases, demonstrating excellent selectivity of the as-fabricated PP/G/PANI hybrid sensor. Furthermore, **Figure 4-5d** indicated the sensor possessed excellent repeatability. (The original dynamic resistance changes of flexible PP/G/PANI composite towards 50 ppm NH_3 and H_2S at room temperature were shown same tendency). Meanwhile, the response and recovery times of the PP/G/PANI hybrid sensor towards NH_3 and H_2S were calculated to be 114 s / 138 s and 23 s / 22 s, respectively.
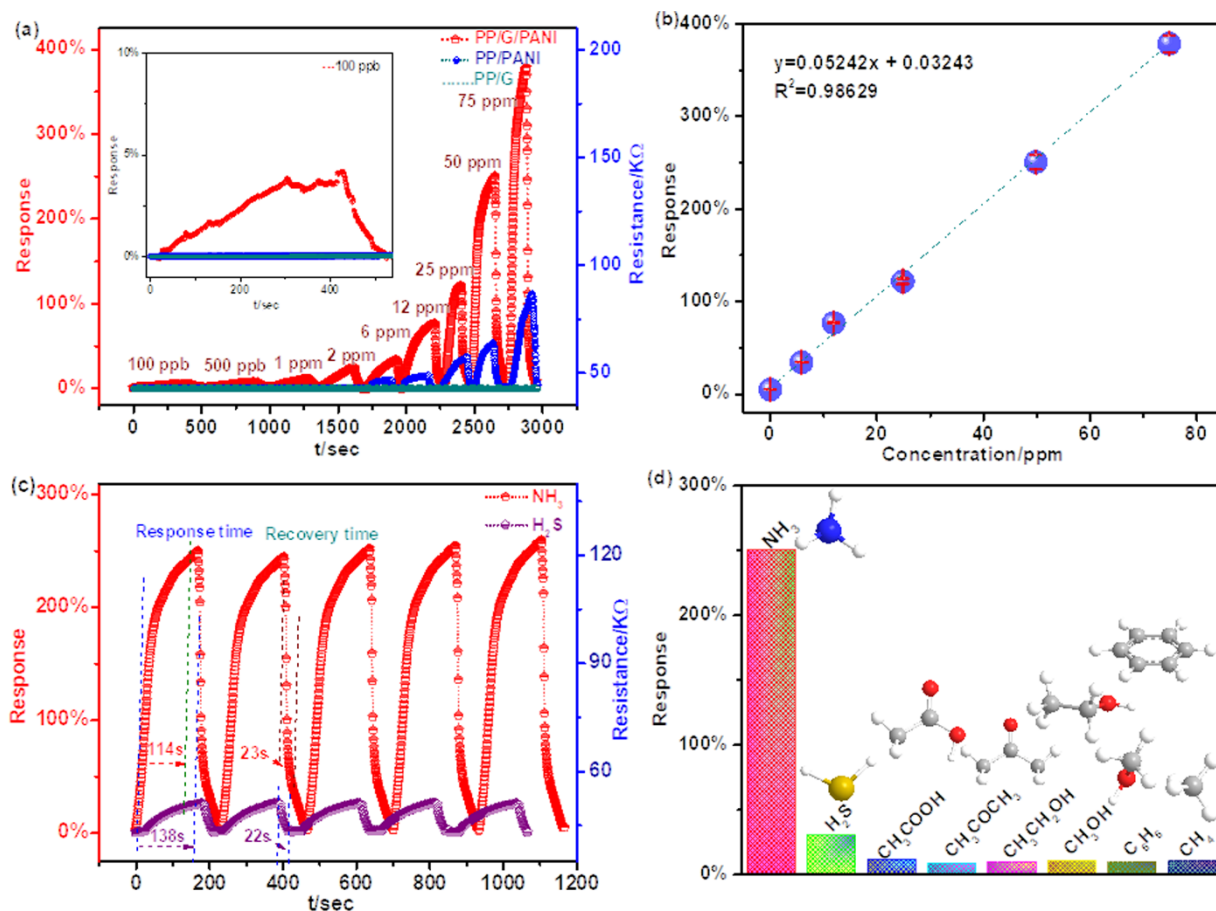
Figure 4-5. (a) Dynamic response of flexible PP/G, PP/PANI, and PP/G/PANI hybrid sensor (inset shows 100 ppb NH_3 response curve in detail). (b) Sensor response as a function of NH_3 gas concentration. (c) Selectivity of flexible PP/G/PANI sensor towards 50 ppm NH_3, H_2S and other organic gases. (d) The sensing reproducibility test for PP/G/PANI composite towards 50 ppm NH_3 and H_2S at room temperature, the humidity in the test chamber is 18%-23%.

To further investigate the gas sensing performance of the PP/G/PANI hybrid sensor, we studied the effect of different temperatures, humidity, and degree of bending angles on the sensor response. **Figure 4-6a** shows the response plots as a function of time for PP/G/PANI hybrid sensing at 15⁰C, room temperature, and 35⁰C towards 50 ppm NH_3 gas. With the increase of temperature, the sensor response presented a stepwise increase trend due to the promoted NH_3 gas adsorption at a higher temperature [84]. The effect of relative humidity on NH_3 sensing performance of the PP/G/PANI

hybrid sensor was further investigated, and the results are shown in **Figure 4-6b**. The response increased with increasing relative humidity in the range of 20–60%. The result may be related to the further protonation of PANI through absorbed water or the generation of H_3O^+ [111].

As shown in **Figure 4-6c**, the flexibility properties of the PP/G/PANI hybrid sensor were evaluated at 50 ppm NH_3 at room temperature. The results showed that the response value of the sensor showed negligible change in different bending states, which proves the excellent flexibility of the hybrid sensor. Furthermore, long-term stability is an important index to assess the reliability of gas sensors. **Figure 4-6d** showed the sensor response value was still close to 250% even after 30 days, indicating high stability of the PP/G/PANI hybrid sensor.

Finally, the sensing performances of the PP/G-PANI hybrid film sensor and the other flexible ammonia gas sensors reported previously were compared, as shown in **Table 4-1**. It was obvious that the PP/G/PANI hybrid sensor possesses a good response value, short recovery time, and low detectable concentration towards NH_3 gas.
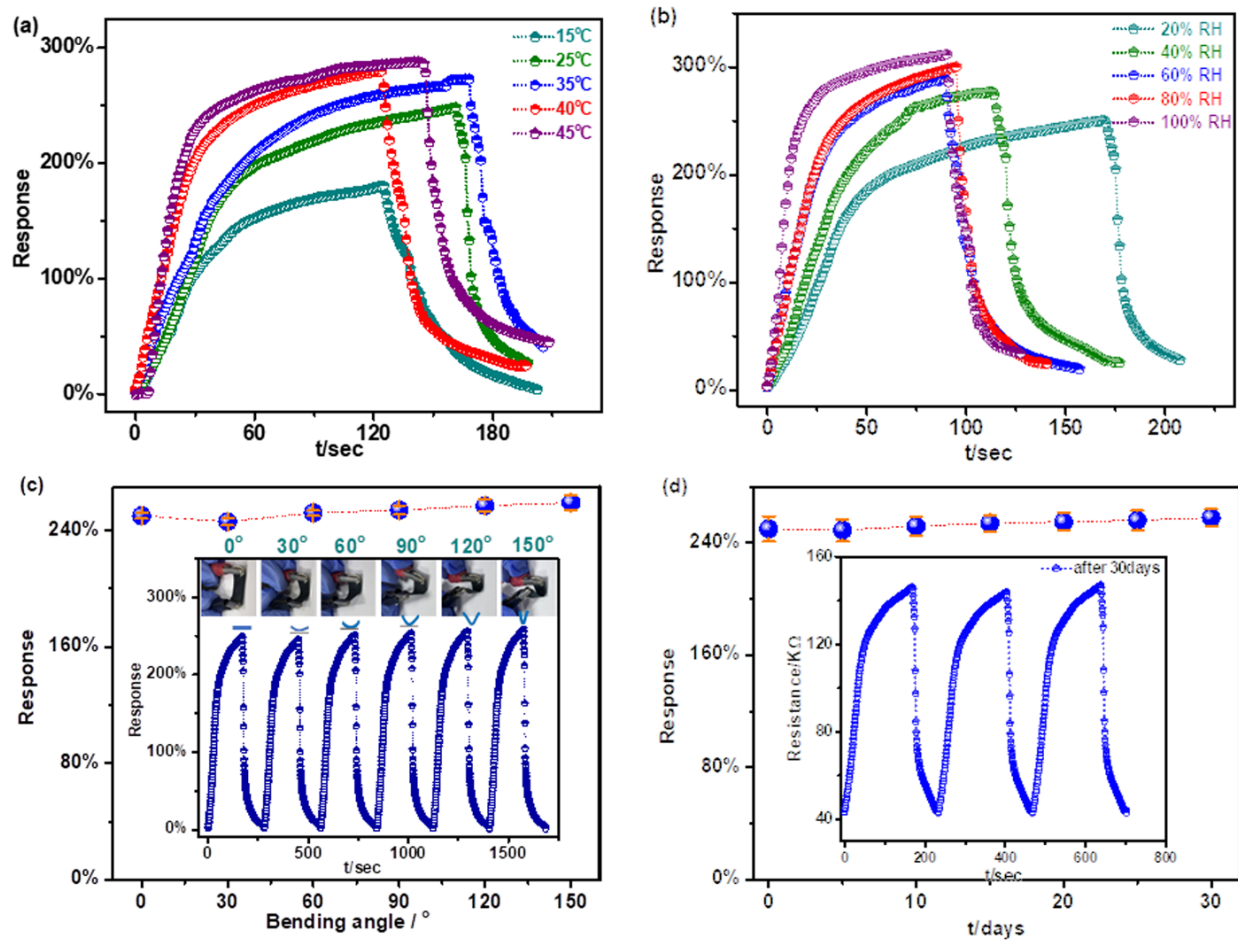
Figure 4-6. (a)The response of PP/G/PANI sensor at different temperatures towards 50 ppm NH₃, RT is room temperature. (b) The response of the PP/G/PANI sensor at different humidifies towards 50 ppm NH₃ at room temperature. (c) The effect of bending state on PP/G/PANI sensor. (Inset shows the response curves of the composite sensor at different bending angles ranging from 0-150°.) (d) Long-term stability of the PP/G/PANI sensor at room temperature.

Table 4-1. Comparison of ammonia gas sensing performance for the PANI-based flexible gas sensors fabricated reported in previous literatures with the present work results.

Ref.	Response Value	Response Time	Recovery Time	Detection Range	Sensing Material	RT	Flexible
[112]	386% (25 ppm)	213s	98s	25-200 ppm	PET/PANI	yes	yes
[113]	20% (4 ppb)	>60s	/	1-8 ppb	Fabrics/ PANI	yes	yes
[114]	31.8% (50 ppb)	145s	302s	0.05-100 ppm	PET/GO-PANIHs	yes	yes
[115]	92% (100 ppm)	9s	30s	0.2-100 ppm	Fabric/CNT/PANI	no	yes
[88]	60% (1 ppm)	46s	198s	0.1-5 ppm	PVDF/GP-PANI	yes	yes
[116]	101% (5 ppm)	75s	1050s	0.1-5 ppm	PVDF/PANI	yes	yes
This work	250% (50 ppm NH$_3$)	114s	23s	0.1-75 ppm	PP/G/PANI	yes	yes
	28% (50 ppm H$_2$S)	138s	22s	10-50 ppm			

4.3.3 Sensing mechanism of the PP/G/PANI hybrid sensor

The sensing mechanism of PANI is reflected in the change of sensor resistance in the ammonia atmosphere, which is related to the protonation/deprotonation process. When the protonated polyaniline was exposed to NH$_3$ gas circumstance, the NH$_3$ molecules took away the protons in the acidified polyaniline, resulting in the reduction of PANI from the conductive emeraldine salt

state (PANI-ES) reduced to non-conductive intrinsic emeraldine base state (PANI-EB), its electrical conductivity was significantly reduced, and the resistance increased. Conversely, the reaction process was reversed when the sensor was exposed to the air atmosphere. The emeraldine base state was converted into the emeraldine salt state, leading to a decrease in resistance [84, 114]. The reaction process is as follows:

$$PANI-NH (ES) + NH_3 \leftrightarrow PANI (EB) + NH_4^+ \tag{2}$$

The sensing mechanism of the PP/G/PANI hybrid film is depicted in **Figure 4-7**. The enhanced sensing performance of the PP/G/PANI sensor should be attributed to the following three synergistic effects: the reversible acid-base doping/de-doping process of PANI, the sensing enhancement effect of the efficient conducting paths formed by the G/PANI interconnected-network structure, and the hierarchical porous microstructure of the PP substrate. When PANI covers the graphene surface evenly, the graphene layer on the peripheral wall of the PANI may lead to the formation of covalent bonds at defect sites and increase the conductivity of the composite upon exposure to ammonia molecules [33]. In addition, the G/PP network structure can form efficient conducting sensing paths and enhance charge transfer efficiency [116]. Furthermore, the hierarchical porous microstructure of the PP/G/PANI hybrid provides more space and vacancies. Therefore, the relevantly large contact area may be able to provide sufficient NH_3 gas diffusion pathways and abundant active adsorption sites, which improves the sensing performance of the PP/G/PANI sensor [78].
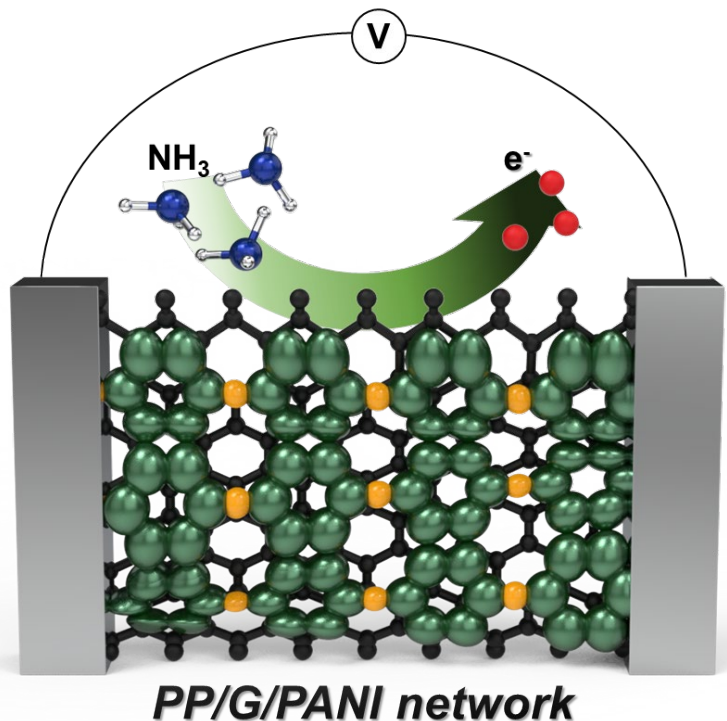
Figure 4-7. The proposed gas sensing mechanism of the PP/G/PANI hybrid sensor.

4.3.4 Volatile sulfur compounds contained in the exhaled breath monitoring

To confirm that the fabricated hybrid sensor can be used for practical detection of VSCs contained in exhaled breath, we investigated the sensing response of the PP/G/PANI hybrid sensor to the exhaled breath of healthy volunteers before and after ingestion of raw garlic. Studies have shown that garlic breath contains a variety of sulfur-containing gases, such as methyl mercaptan, dimethyl sulfide, allyl mercaptan, allyl methyl sulfide, dimethyl disulfide, etc. [34]. Therefore, garlic breath is a good sample for evaluating the sensing ability of exhaled VSCs and can be used as a detection target. The sensing results are shown in **Figure 4-8**. (The original resistance changes of flexible PP/G/PANI sensor towards VSCs in exhaled breath, pure H_2S, and NH_3 are shown same tendency). When the PP/G/PANI hybrid sensor detects fresh breath at room temperature, the response value

is only lower than 2%, which is due to the fresh breath of a healthy volunteer maintaining a tiny amount of sulfur-containing gas. Notably, when detecting garlic breath of the healthy volunteer, the response value can be reached 10%, which is close to pure H_2S (10 ppm) and one-seventh of the response of NH_3 (10 ppm). It should be noted that the response and recovery time of detecting garlic breathing is only about 20 seconds. These results prove that the PP/G/PANI hybrid sensor can effectively detect VSCs in exhaled garlic gas, suggesting the potential application in breath monitoring and kidney disease diagnosis.
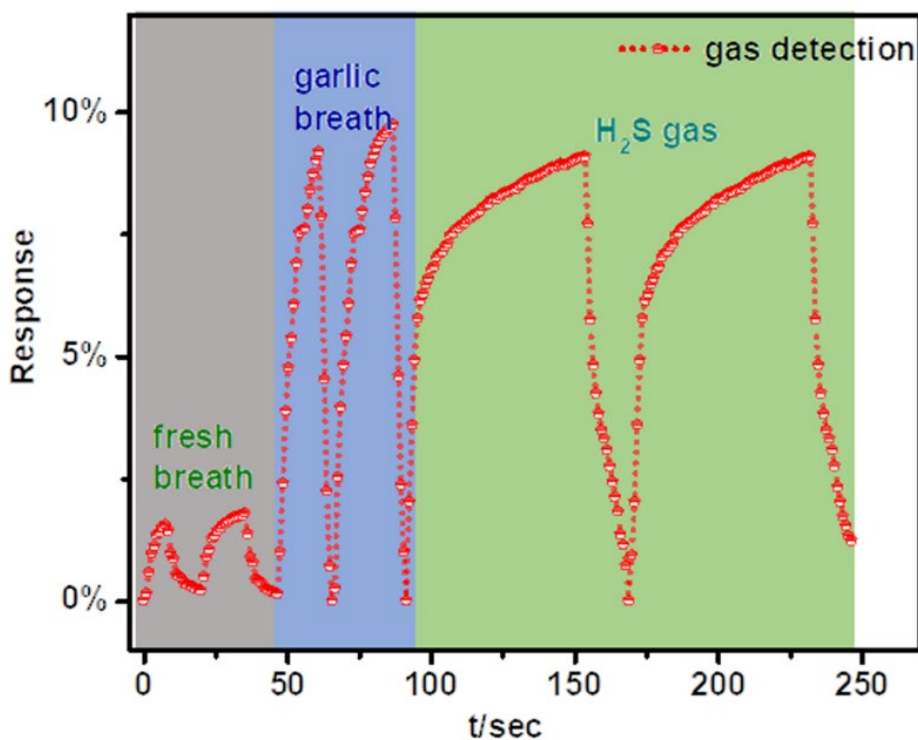
Figure 4-8. Photograph of flexible PP/G/PANI sensor for VSCs in exhaled breath, pure H_2S and NH_3 gas detection.

4.4 Conclusion

In this work, flexible PP/G/PANI hybrid gas sensors were fabricated using the waste disposable

mask as the flexible substrate. It is observed that the flexible hybrid gas sensor exhibits ppb-level detection limit, high response (378% towards 75 ppm NH_3), remarkable response time, and recovery time. The flexible PP/G/PANI hybrid gas sensor presents good repeatability, long-term stability, and selectivity towards ammonia gas compared with H_2S gas and other organic gases. Moreover, the degree of bending angles has no apparent effect on the sensing results, which strongly proves the excellent flexibility of the hybrid sensor. The enhancing sensing performance of the hybrid sensor should be ascribed to the synergistic effects of the G/PANI interconnected-network structure and the porous microstructure of the PP substrate. In addition, the PP/G/PANI sensor can be used to detect VSCs contained in exhaled breath at room temperature, demonstrating the potential application of the hybrid sensor for kidney disease diagnosis.

Chapter 5 Conductive $Ti_3C_2T_x$/PANI-PP composite sensor for CO_2 gas and human respiratory rate detection

5.1 Introduction

Human respiration analysis is a rapid, painless, inexpensive, and non-invasive method for maintaining health and diagnosing early illnesses [47, 117-119]. It has been widely used for keeping track of heart failure, lung cancer, asthma, and respiratory abnormalities. Such breath analysis is essential for reducing respiratory diseases and preventing sudden death [26, 120]. There have been publications in recent years on the monitoring and detection of COVID-19 in human breath [25, 121]. Human exhaled breath includes over 500 different compounds, such as oxygen, carbon dioxide, nitrogen, water vapor, volatile organic components, and so forth [122, 123]. The concentration and composition of these compounds carry a wealth of biochemical and physiological information, making them potential biomarkers for disease and metabolic process assessment [18, 21, 54, 124]. Among them, CO_2 as one of the greenhouse gases, has been of great interest in monitoring air quality in enclosed crowded spaces and respiratory diseases. The American Society of Heating, Refrigerating, and Air-Conditioning Engineers (ASHRAE) recommends that the CO_2 concentrations in indoor spaces should not exceed 1000 ppm, while outdoor spaces should not exceed 350-800 ppm [125]. Concentrations over 1000 ppm may cause headaches, nasal or respiratory inflammation, and fatigue [126]. Additionally, recent research has shown that SARS-CoV-2/COVID-19 can be transmitted through aerosols, making indoor transmission easier than outdoor transmission [127, 128]. The risk of infection is increased by excess CO_2 indoors, which is primarily caused by human exhalation. But the specific level of CO_2 associated with COVID-19 infection risk is largely unknown due to insufficient data on measured CO_2 conditions [128, 129]. A variety of measuring techniques have been used for CO_2 detection, including optical spectroscopy [130], gas

chromatography (GC) [93, 131], surface and bulk acoustic waves [132], and nondispersive infrared (NDIR) spectroscopy [19, 133]. However, these methods have limitations on bulky size, high price, complex processing, external power supply, etc. Therefore, the development of low-cost, portable, and wearable devices for the detection of CO_2 is essential for environmental and human health state assessment.

For the past few decades, metal oxide semiconductors (MOSs) and ceramic materials such as Al_2O_3, CdO, ZnO, TiO_2, SnO_2, NiO, and $BaTiO_3$ have been utilized in the development of CO_2 sensors using chemi-resistive sensing technology [134-136]. Kanaparthi et al. [137] fabricated a resistive gas sensor based on ZnO nanoflakes to detect CO_2 gas, exhibiting highly sensitive, reversible, and ultrafast detection with excellent sensitivity (0.1125) and a fast response time (less than 20 s) at 250°C. Joshi et al. [138] synthesized an $Ag@CuO/BaTiO_3$ composite by a simple hydrothermal method. It was demonstrated that the obtained composite CO_2 sensor exhibited exceptional stability and sensitivity, high repeatability and accuracy, and a rapid recovery time at 120 °C. However, these MOSs and ceramic materials suffer from drawbacks, such as their rigid and brittle nature, high operating temperature, and large energy consumption [13, 68, 94].

Conducting polymers (CPs), such as polyaniline (PANI) and poly(3,4ethylenedioxythiophene) (PEDOT), have been investigated as flexible and room temperature CO_2 sensing materials due to their desirable mechanical and electrical properties, unique protonation and deprotonation processes, and facile synthesis process [4, 60, 70, 139]. Nevertheless, pure CP presents disadvantages, such as sluggish response time, prolonged recovery time, and limited stability [140]. Therefore, CP-based composites have been explored to improve sensing characteristics. Barde et al. [141] developed a CO_2 sensor based on $PANI/NaO_2$ composite films using an ex-situ technique, and the composite sensor exhibited a rapid response time and a higher response value (60%) when compared to the

pure PANI (38%) sensor. Sonker et al. [142] prepared a CO_2 sensor based on PANI-TiO_2 nanocomposite film *via* a spin coating technique, which showed a response and response/recovery time of 53% and 6.2/5.7 min to 1000 ppm CO_2 at 30°C, respectively. The sensing response was 20 times higher than pristine TiO_2 and 7 times higher than pristine PANI.

Two-dimensional (2D) materials, such as graphene [143, 144], black phosphorus [145], and MoS_2 [146] [147], have shown excellent performance as gas sensors due to their high specific surface area, versatile surface chemistry, low electronic noise, and good stability at room temperature. Although the practical application of these 2D material-based gas sensors can be limited by long recovery time and interference from humidity conditions, the unique 2D materials can diversify the synthesized structure via a composite form and enhance their sensing properties [74, 110]. MXenes are a new family of 2D materials composed of transition metal carbides and nitrides. They have been extensively studied in the sensor field due to their high sensitivity to acetone, ammonia, methane, and ethanol, thanks to their metallic conductivity, favorable hydrophilicity, and abundant surface functional groups [40, 42, 148, 149]. Moreover, MXenes were used for CO_2 selective reduction or adsorption through its spontaneous crossing of transition states [150, 151]. Therefore, MXenes can be excellent candidates for CO_2 sensing material. Combing MXene with PANI can provide a flexible and wearable sensing device for high-performance CO_2 detection and human respiratory monitoring.

Herein, we demonstrate $Ti_3C_2T_x$/PANI-PP composite sensor to present rapid response and recovery time, reliable long-term stability, ppm-level detection limit, admirable selectivity and sensitivity towards CO_2. Besides, we report wearability study by investigating the effect of humidity, temperature, different bending and folding states on the sensing properties. Finally, the fabricated wearable wireless Bluetooth sensing devices demonstrate the capability of detecting

human respiratory rate, indicating the potential application of this $Ti_3C_2T_x$/PANI-PP composite for developing a breath sensing system for early respiration disease diagnosis.
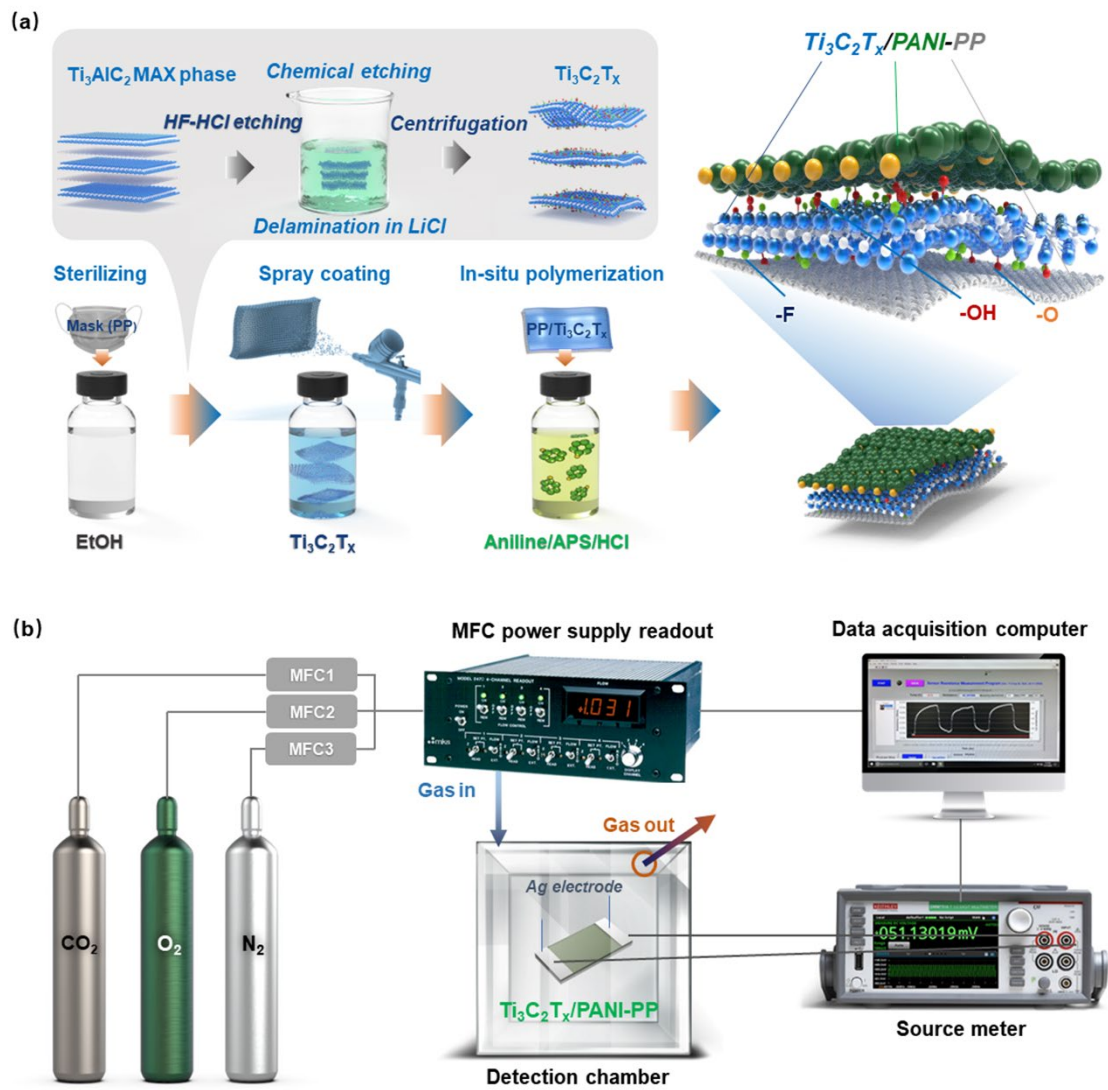
Figure 5-1. (a) The schematic of preparation of the delaminated Ti3C2Tx and Ti3C2Tx/PANI-PP composite. (b) Schematic diagram of the CO2 sensing system.

5.2 Experimental section

5.2.1 Materials

Disposable masks were purchased from Guangzhou Montana West Industrial Company (Guangzhou, Guangdong Province, China). The filter layer (denoted as PP) of the mask was used as the flexible substrate in this study. Ammonium persulphate (APS, 98% purity), aniline monomer, hydrochloric acid (36.5-38%, ACS grade, BDH), copper sheet and sliver paint (127185-15G) were purchased from VWR. Titanium powder (325 mesh, 99.5%), aluminum powder (325 mesh, 99.5%), titanium carbide powder (99.5%, Alfa Aesar), and lithium fluoride (325 mesh, 98.5%) were purchased from Alfa Aesar.

5.2.2 Synthesis of the Ti_3AlC_2 MAX Phase

Ti_3AlC_2 was synthesized by mixing TiC powder, titanium powder, and aluminum powder, in a molar ratio of 2:1:1. The above mixture was ball milled with zirconia balls for 18 h and heated in a furnace at 1400 °C for 4 h at a heating rate of 5°C/min. The resulting mixture was milled to 400 mesh and the Ti_3AlC_2 Max Phase was obtained.

5.2.3 Synthesis of $Ti_3C_2T_x$ MXene Solution

Delaminated $Ti_3C_2T_x$ was prepared in a mixed acid environment, as reported in literature [61]. Briefly, 1 g of Ti_3AlC_2 was slowly added to a 20 mL mixture of HF (49 wt%), HCl (12 M), and deionized water (DI) water with a molar ratio of 1:6:3. The mixture was stirred using a Teflon-coated magnetic stirring bar at 35°C for 24 h. After etching, the multilayer $Ti_3C_2T_x$ was washed with DI water and centrifugated at 3500 rpm for 5 min until the pH of the supernatant was close to 6. The sediment was then mixed with a 50 mL solution containing 1 g of LiCl and stirred for 18 h at room temperature. Finally, the solution was centrifuged at 3500 rpm until a dark supernatant

remained, indicating complete delamination of $Ti_3C_2T_x$ in water. The obtained $Ti_3C_2T_x$ solution was stored in a refrigerator for further use.

5.2.4 Fabrication of $Ti_3C_2T_x$-PP Composite

PP was utilized as the flexible substrate for composite sensors. The PP film was soaked in ethanol solution and then in DI water to remove contaminants. Afterward, the PP film was spray-coated using the $Ti_3C_2T_x$ MXene solution on both sides. After air drying, the $Ti_3C_2T_x$-PP composite was obtained.

5.2.5 Fabrication of $Ti_3C_2T_x$/PANI-PP Composite

Aniline (0.8 mL) was dissolved in 200 mL of 1 M HCl solution (solution A) and stirred for 10 min. 0.92 g of APS was dissolved in precooled 40 mL of 1 M HCl solution (solution B). The *in-situ* polymerization of aniline was initiated by slowly adding solution B to solution A. The PP sample and $Ti_3C_2T_x$-PP composite sample were soaked in the above-mixed solutions, respectively, and then stirred magnetically at 30°C for 60 min. The obtained PANI-PP and $Ti_3C_2T_x$/PANI-PP composite samples were washed several times with DI water to remove the extra hydrochloric acid and dried at room temperature overnight. The composite samples were cut into 15 mm × 10 mm pieces and a small amount of silver paint was coated on both sides of the samples to reduce the connection resistance. The weight percentage of each material in the composite samples was determined to measure the ratio of PP, $Ti_3C_2T_x$, and PANI. The synthesis process of the flexible $Ti_3C_2T_x$/PANI-PP composite is illustrated in **Figure 5-1a**.

5.2.6 Gas-Sensing Measurements

The $Ti_3C_2T_x$/PANI-PP sensor was placed in a closed test chamber connected with target gases that were precisely controlled by a separate mass flow controller (MFC), as illustrated in **Figure 5-1b**. The change of electrical resistance of the sensor samples was monitored using a Kethley 2400

source meter. Various concentrations of CO_2 gas were generated by manipulating the ratio of gases introduced into the test chamber. This was done by mixing synthetic air, comprised of 80 sccm N_2 and 20 sccm O_2, with a predetermined amount of CO_2 gas. During the gas introduction for the sensing process, the resistance value of the gas sensor was continuously monitored until it reached a steady state and remained consistent over a specific duration. Once a stable resistance was obtained, the carbon dioxide control valve was closed. To expedite the removal of the target gas, the chamber was purged and refilled with air. Throughout the entire sensing process, the sensor's position was held constant while ensuring stable air pressure, humidity, and temperature. Different humidity conditions were achieved using a programmable MFC, where carrier N_2 passed through a bubbler. All the sensing experiments were carried out at room temperature ($24.0\pm1°C$), fitting of the impedance data was performed using a customized Labview program. The gas sensing response value can be calculated following the equation below:

Response (%) = $\triangle R/R_0 \times 100\%$ (1)

where R_0 and $\triangle R$ are the original resistance of the sensor in air and the change of resistance after exposure to the target gas compared with in air, respectively.

5.2.7 Human Respiration Rate Real-time Monitoring

The $Ti_3C_2T_x$/PANI-PP composite sensor was pasted on the filter layer of the disposable mask. One end of the wireless sensing module was connected to the $Ti_3C_2T_x$/PANI-PP sample, and the other end was connected to a 5V power supply. The sensor system transmitted all electrical signals via Bluetooth, and the data analysis was done through the WeChat applet "Wireless Bluetooth Sensor". To mitigate the effect of extreme humidity on sensing signals, a layer of non-woven fabric filter film was wrapped around the sample.

5.2.8 Materials Characterization

The morphology and qualitative elemental analysis of the PP, $Ti_3C_2T_x$-PP, PANI-PP, and $Ti_3C_2T_x$/PANI-PP samples were characterized using a JEOL JSM-7000F scanning electron microscope (SEM) equipped with energy-dispersive spectrometer mapping, operating at an acceleration voltage of 20 kV. Further surface chemistry analysis of the sensing materials was performed by Fourier Transform Infrared Spectroscopy (FT-IR) on a Thermo Nicolet 6700. The instrument was set to record spectra in the wavenumber range from 2000 to 400 cm^{-1} at a resolution of 4 cm^{-1}. Nitrogen (N_2) adsorption-desorption isotherms were applied to determine the Brunner-Emmett-Teller (BET) surface area. Surface topography of the $Ti_3C_2T_x$ was evaluated using Atomic Force Microscopy (AFM) in non-contact mode on a Park Instruments NX10 AFM. X-ray photoelectron spectroscopy (XPS) analysis was performed using a K-alpha instrument from Thermo Scientific Inc., U.K, equipped with a 180° double focusing hemispherical analyzer and a 128-channel detector, was operated under a vacuum of 4.8×10^{-9} mbar. The analysis involved exposure to monochromatic Al X-rays with a step size of 1 eV, concentrated on a sampling area of 400 μm in diameter. For the interpretation of the core-level spectra, a specific software package 'AVANTAGE' was utilized. The Shirley function was applied for background removal prior to quantification. The materials structure was explored with a Bruker X-ray diffractometer (XRD), using LYNXEYE technology, operating at 40 kV and 40 mA with Cu Kα radiation.

5.3 Results and discussion

5.3.1 Morphology and structure

The morphology of the synthesized $Ti_3C_2T_x$-PP, PANI-PP, and $Ti_3C_2T_x$/PANI-PP samples was observed by SEM, and the results are shown in **Figure 5-2**. In **Figure 5-2a**, the PP sample shows the cylindrical fiber structure with a smooth surface. As shown in **Figure 5-2b**, the PP substrate

surface is covered by flocculent PANI particles. **Figure 5-2c** shows that the $Ti_3C_2T_x$ nanoflakes are wrapped around the PP substrate. The AFM analysis further confirmed the single-layer or few-layer structure of the synthesized $Ti_3C_2T_x$ with the thickness of 2.13 or 2.18 nm. It can be clearly seen that these $Ti_3C_2T_x$ nanoflakes are mixed with the PANI particles randomly in **Figure 5-2d**. Moreover, to study the dispersed state of different surface elements in the $Ti_3C_2T_x$/PANI-PP sample, EDS mapping analysis was further performed (**Figure 5-3b–i**). The element weight and atomic percentage are summarized in **Figure 5-3i**. F, Cl, C, O, N, and Ti elements were distributed uniformly in the whole $Ti_3C_2T_x$/PANI-PP composite. The uniform dispersion of these elements will be beneficial for promoting the gas adsorption performance [62].
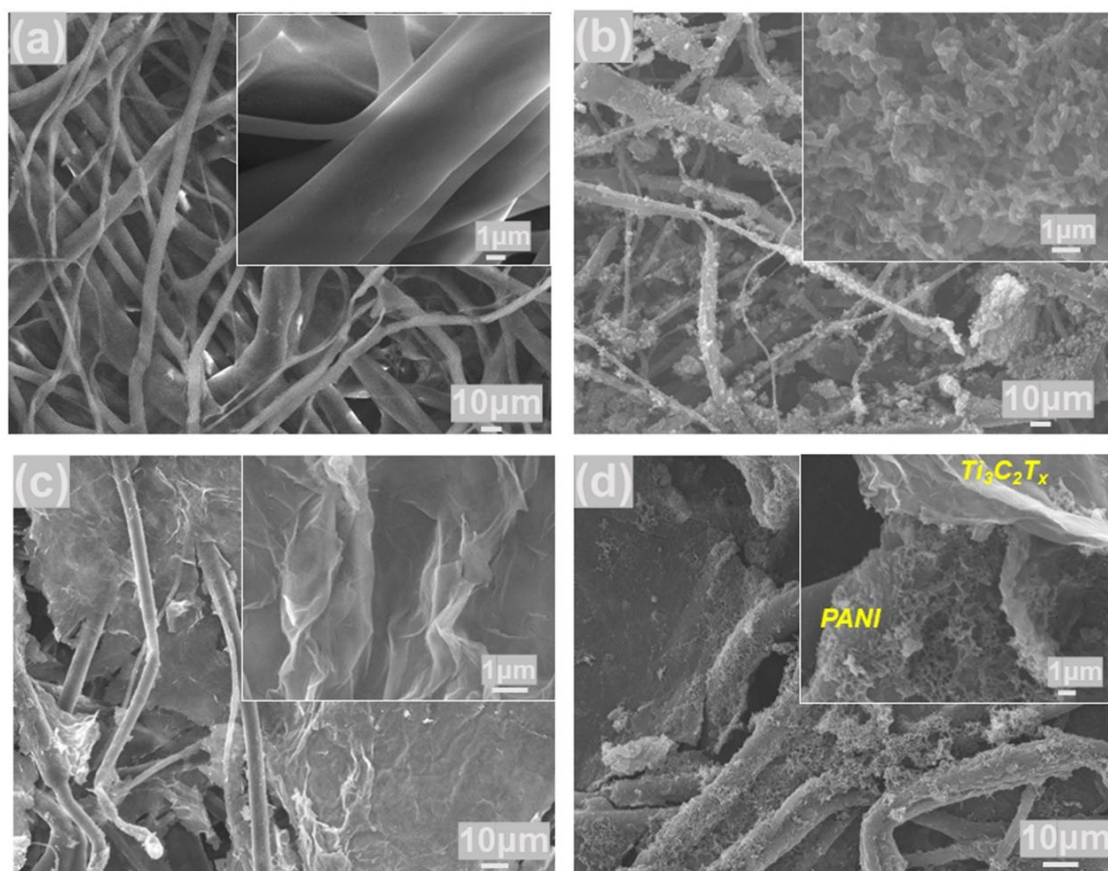
Figure 5-2. SEM images of (a) PP, (b) PANI-PP (80:20), (c) $Ti_3C_2T_x$-PP (80:20), (d) $Ti_3C_2T_x$/PANI-PP (40:40:20) network.
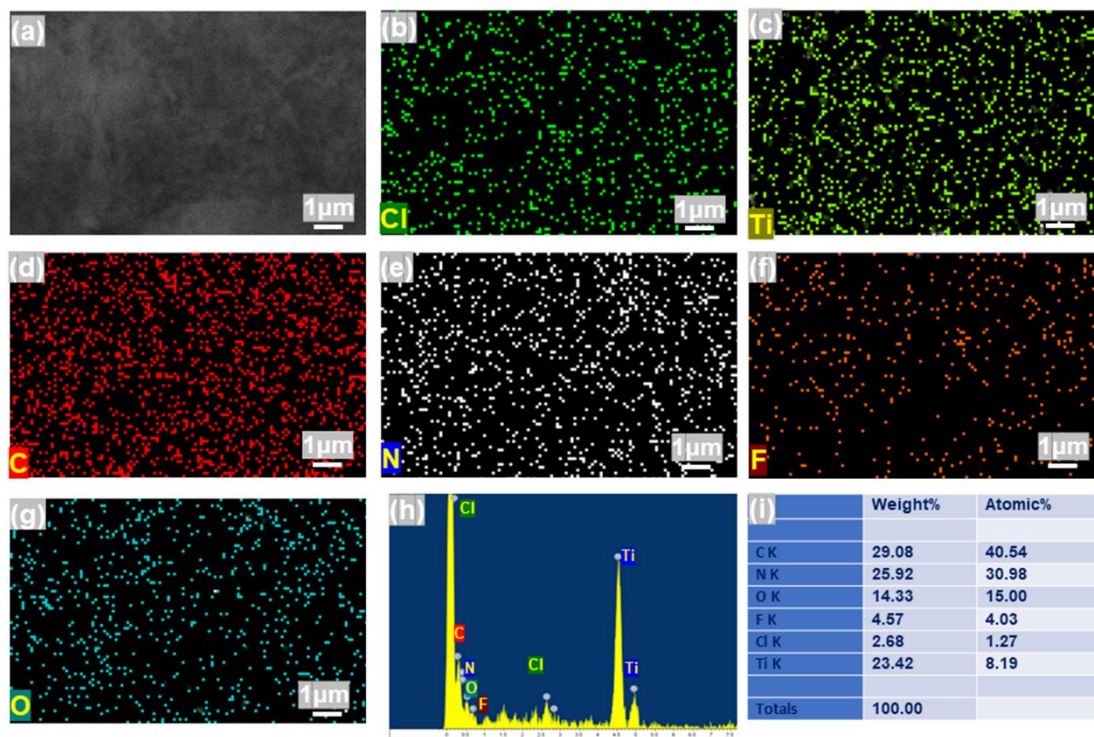
Figure 5-3. (a) Magnetified SEM image, (b–h) EDS elemental mapping (F, Cl, C, O, N, and Ti elements) of $Ti_3C_2T_x$/PANI-PP (40:40:20). (i) The element weight percentage and atomic percentage of $Ti_3C_2T_x$/PANI-PP.

The N_2 adsorption/desorption isotherms of $Ti_3C_2T_x$-PP and $Ti_3C_2T_x$/PANI-PP composites are shown in Figure S2a-2b. The observed adsorption/desorption isotherms for these samples were close to parallel, and likely demonstrated uniform pore estimation. As shown in Figure S2c, the surface areas of pristine PP, $Ti_3C_2T_x$-PP, PANI-PP, and $Ti_3C_2T_x$/PANI-PP composite were calculated to be 70.641, 79.233, 86.356, 102.892 m^2/g, respectively. When PANI is combined with $Ti_3C_2T_x$, the abundant surface functional groups and oxygen atoms of $Ti_3C_2T_x$ provide numerous sites for interaction with PANI. These interactions may include hydrogen bonding, ionic bonding, π-π stacking, and others, potentially leading to the formation of a more complex structure in the PANI/$Ti_3C_2T_x$ composite, thereby increasing the surface contact area. Notably, the porous

$Ti_3C_2T_x$/PANI-PP composite shows a much larger surface area than other samples, which might be helpful to enhance gas sensing performance.

To investigate the surface chemistry, different functional groups of the fabricated films were measured by FTIR, as shown in Figure S3a. The absorption peaks of polypropylene can be observed at 843 cm^{-1}, 1002 cm^{-1}, 1385 cm^{-1}, and 1456 cm^{-1}, which correspond to C–CH$_3$ stretching, –CH$_3$ rocking vibration, –CH$_3$ symmetric bending, and –CH$_2$ symmetric bending vibration, respectively [63, 64]. Compared with PP, new peaks appeared in the spectrum of the PANI-PP sample, the absorption peaks at 1300 cm^{-1} and 1165 cm^{-1} are attributed to C−N stretch of the secondary amine and C–H in-plane bending, respectively [65, 66]. Additionally, the $Ti_3C_2T_x$-PP displayed new characteristic bands at 1079 cm^{-1}, 1227 cm^{-1}, 1364 cm^{-1}, and 1644 cm^{-1} are ascribed to C–F vibration, oxygen vibration, O–H vibration, and C=O bonding, respectively [67, 68] the O–H functional groups may have good reactivity with target gas to improve the sensing performance. It should be noticed that the main absorption peaks (e.g., 995 cm^{-1}, 1163 cm^{-1}, 1223 cm^{-1}, 1381 cm^{-1}, 1452 cm^{-1}, 1642 cm^{-1}) of $Ti_3C_2T_x$/PANI-PP slightly shift towards lower wavenumber compared with $Ti_3C_2T_x$-PP and PANI-PP, this may be due to the weak interaction (e.g., Van der Waals forces) between PANI and the functional groups of $Ti_3C_2T_x$ [69]. The XRD patterns for the Ti_3AlC_2 MAX phase and $Ti_3C_2T_x$ film are depicted in Figure S3b. After the complete Al removal from MAX phase and successful $Ti_3C_2T_x$ delamination, all Ti_3AlC_2 MAX phase-related peaks vanished post-etching, excluding the peak for the (002) plane. This (002) peak shifted to lower angles, revealing an expansion in the d-spacing and c-lattice parameter (c-LP) of the formed $Ti_3C_2T_x$ compared to the initial Ti_3AlC_2 MAX phase, corroborating previously report findings [70].

XPS analysis was further carried out to determine the types and relative abundance of functional groups in the fabricated $Ti_3C_2T_x$/PANI-PP composite. As shown in **Figure 5-4a**, the survey spectra confirmed the successful synthesis of $Ti_3C_2T_x$/PANI-PP composites. The N 1s spectrum of PANI-PP (**Figure 5-4b**) displays distinct peaks at 399.1, 399.9, 400.8, and 402.2 eV that are attributed to =N, –NH–, =NH$^+$–, and –NH$_2^+$–, respectively [58, 71]. The N 1s spectrum of the $Ti_3C_2T_x$/PANI-PP composite (**Figure 5-4c**) exhibits lower content of =N– and higher content of N$^+$ (–NH$^+$– and –NH$_2^+$–) when compared to the PANI-PP sample. The increased N$^+$ amount indicates enhanced protonation of PANI in the $Ti_3C_2T_x$/PANI-PP composite by the introduction of delaminated $Ti_3C_2T_x$ during PANI polymerization [58, 72]. The C 1s spectrum (**Figure 5-4d**) shows binding energies concentrated around 282.8, 283.7, 284.7, 286.1, and 287.4 eV, corresponding to C–Ti, C=C, C–C, C=N, and C=N$^+$, respectively [73, 74]. The O 1s spectrum (**Figure 5-4e**) displays peaks at 529.5, 530.6, and 532.6 eV that correspond to O–Ti, OH–Ti, and N–O–Ti, respectively, indicating the presence of oxygen, hydroxyl groups, and possible TiO$_x$ species due to the partial oxidation of $Ti_3C_2T_x$ [74, 75]. **Figure 5-4f** exhibits the Ti 2p core level fitted with Ti 2p$_{1/2}$, and Ti 2p$_{3/2}$ peaks at 455.2, 456.4, and 457.7 eV, which are assigned to Ti–C (Ti$^+$), Ti^{2+}/Ti^{3+}, and Ti–O (Ti^{4+}), respectively, suggesting that the $Ti_3C_2T_x$ MXene was slightly oxidized during the transfer process [76, 77]. The F 1s spectrum of the composite depicted peaks at 683.1 and 684.4 eV, corresponding to Ti–F and C–F, respectively.
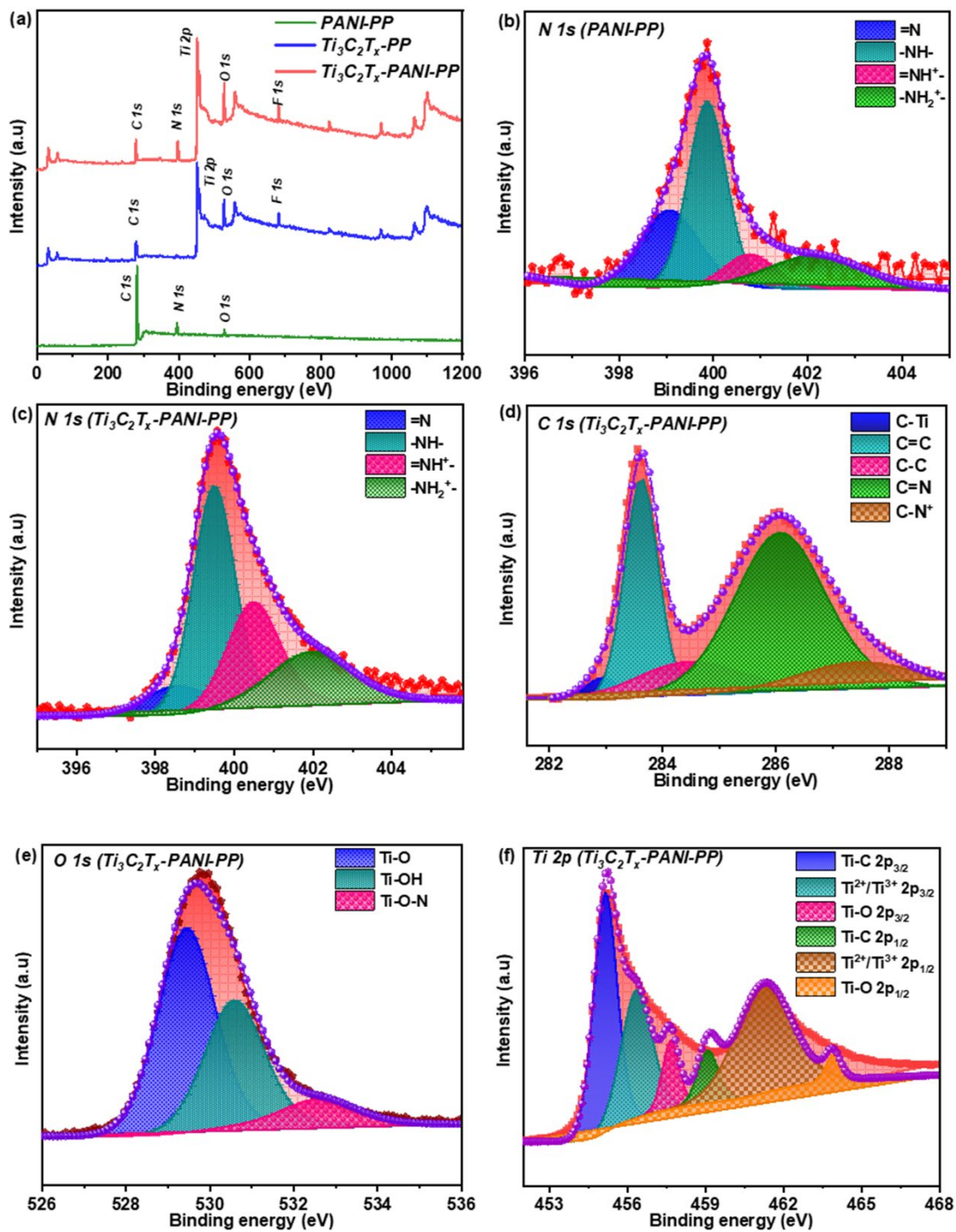
Figure 5-4. The XPS spectra of (a) survey scan of PANI-PP, $Ti_3C_2T_x$-PP, and $Ti_3C_2T_x$/PANI-PP composites. (b) N 1s spectrum of PANI-PP (c–f) N 1s, C 1s, O 1s, Ti 2p spectra of $Ti_3C_2T_x$/PANI-PP composite.

5.3.2 Gas-sensing properties

The sensing properties of the flexible composite sensors based on $Ti_3C_2T_x$-PP, PANI-PP and $Ti_3C_2T_x$/PANI-PP films were investigated at room temperature. **Figure 5-5a** depicts the dynamic response changes toward CO_2 (25–500 ppm) at 24°C. With the increase in CO_2 concentration, the response of all these three sensors increased. In particular, the response of the $Ti_3C_2T_x$/PANI-PP sensor is 15.2% towards 500 ppm CO_2, which is 2.35 times higher than the PANI-PP sensor and 6.52 times higher than the $Ti_3C_2T_x$-PP sensor. The original baseline resistance of sensors changes over time is shown in Figure S5a. After combining PANI with $Ti_3C_2T_x$, the initial resistance of the $Ti_3C_2T_x$/PANI-PP was reduced from 82030 Ω to 30410 Ω. These results indicate the hybridization of PANI with MXene was an effective way to modulate electrical resistance. Besides, the $Ti_3C_2T_x$/PANI-PP composite sensor has the lowest detection limit (25 ppm) compared to the $Ti_3C_2T_x$-PP sensor and PANI-PP sensor. The relationship between CO_2 gas concentrations and response at room temperature is shown in **Figure 5-5b**, and the results indicate that all the $Ti_3C_2T_x$-PP, PANI-PP and $Ti_3C_2T_x$/PANI-PP composite sensors exhibit outstanding linearity. Further tests were carried out to evaluate the reproducibility of the $Ti_3C_2T_x$/PANI-PP composite sensor in response to CO_2 concentrations of 500 and 200 ppm, with the results presented in **Figure 5-5c, 5d**. For instance, **Figure 5-5c** illustrates the consistent response and recovery behavior throughout five testing cycles of the sensor when exposed to 500 ppm of CO_2. This consistent dynamic variation in the transient resistance of the $Ti_3C_2T_x$/PANI-PP composite sensor suggests its good reproducibility. The response/recovery time of the $Ti_3C_2T_x$/PANI-PP composite sensor towards 500 ppm CO_2 was 115/26 s.
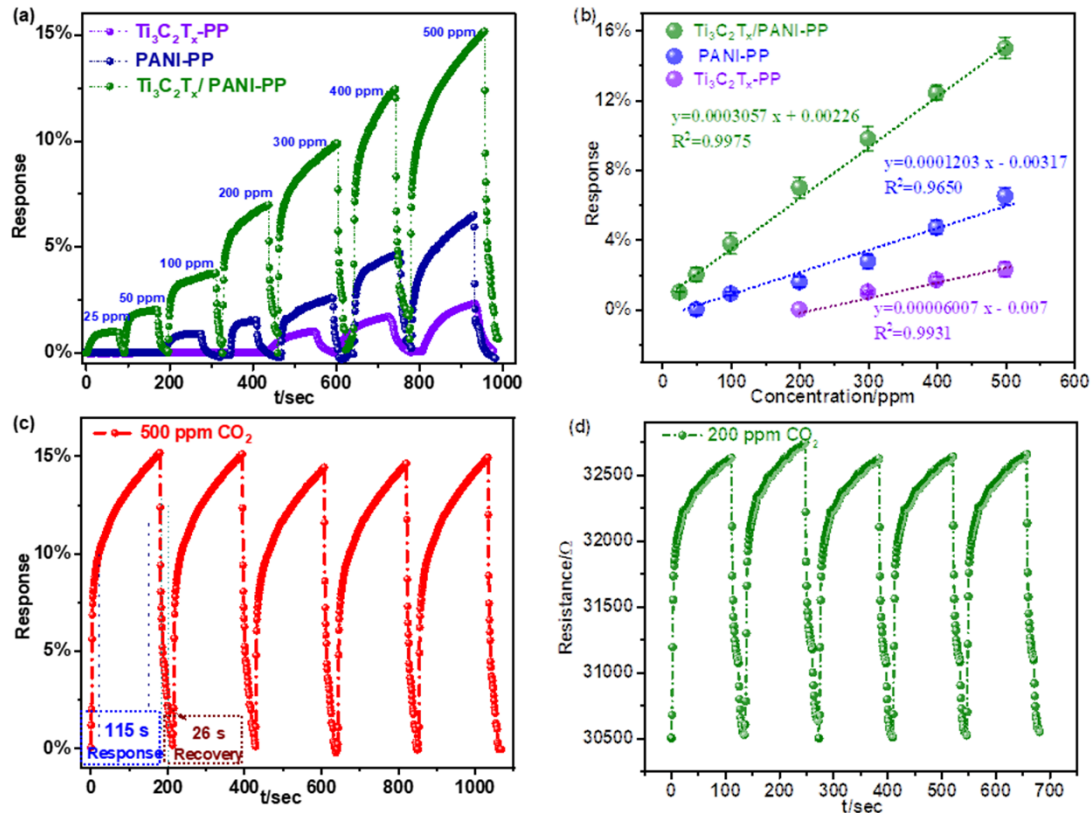
Figure 5-5. (a) The dynamic response-recovery curves of flexible sensors based on $Ti_3C_2T_x$-PP, PANI-PP, and $Ti_3C_2T_x$/PANI-PP composites. (b) Response-concentration fitting curves of flexible sensors based on $Ti_3C_2T_x$-PP, PANI-PP, and $Ti_3C_2T_x$/PANI-PP composites toward 25–500 ppm CO_2 at room temperature. (c) Reproducibility cycles test for the $Ti_3C_2T_x$/PANI-PP composite sensor towards 500 ppm CO_2. (d) Reproducibility cycles test for the $Ti_3C_2T_x$/PANI-PP composite sensor towards 200 ppm CO_2, the RH in the test chamber is 11%–19%.

To investigate the sensing performance at high concentration conditions, the response and resistance changes of the $Ti_3C_2T_x$/PANI-PP sensor under 500–1500 ppm CO_2 were investigated as shown in **Figure 5-6a**. The sensor response and the actual resistance values presented a stepwise increase trend with increasing concentration, and the response can be achieved 22.48% under 1500 ppm CO_2 circumstance. The selectivity of the $Ti_3C_2T_x$/PANI-PP sensor was characterized by comparing the response to interference volatile organic compounds (VOCs), such as benzene, acetone, acetic acid, methanol, ethylene glycol, and methane. Interestingly, among various VOCs,

73

methane, as a greenhouse gas, shows a better sensing response than the others. (The initial resistance of $Ti_3C_2T_x$/PANI-PP composite changes towards 200 ppm CH_4 as shown in **Figure 5-5c**). It was evident from **Figure 5-6b** that the response to CO_2 gas was 2 to 5 times higher than other organic gases, implying the excellent selectivity of the as-prepared $Ti_3C_2T_x$/PANI-PP sensor. This could be attributed to the fact that PANI, as the primary sensing material, exhibits superior reactivity with CO_2 as compared to VOCs such as C_6H_6 and CH_4. When CO_2 interacts with the PANI, it leads to the swelling and distortion of the polymer chain, resulting in significant resistance changes. Furthermore, $Ti_3C_2T_x$ is noted for its excellent metallic properties that enhance charge transport. The presence of abundant defects and functional groups, such as –O and –OH, on its surface may increase the density of effective active sites, facilitating reactions with CO_2 gas [70]. Comparatively, the $Ti_3C_2T_x$/PANI-PP composite sensor demonstrates superior selectivity to CO_2 compared to its $Ti_3C_2T_x$-PP and PANI-PP counterparts. This could be due to the formation of heterojunctions between $Ti_3C_2T_x$ and PANI, which improve the sensor's response to the target gas. In addition, the effect of temperature on the CO_2 gas sensing performance was explored. As shown in **Figure 5-6c**, a slight increase in resistance was observed with the rise of temperature toward CO_2 gas. This result might be attributed to the promoted gas adsorption at a relatively higher temperature. Similarly, an increasing resistance was observed when the sensor was tested in the air (**Figure 5-6d**).
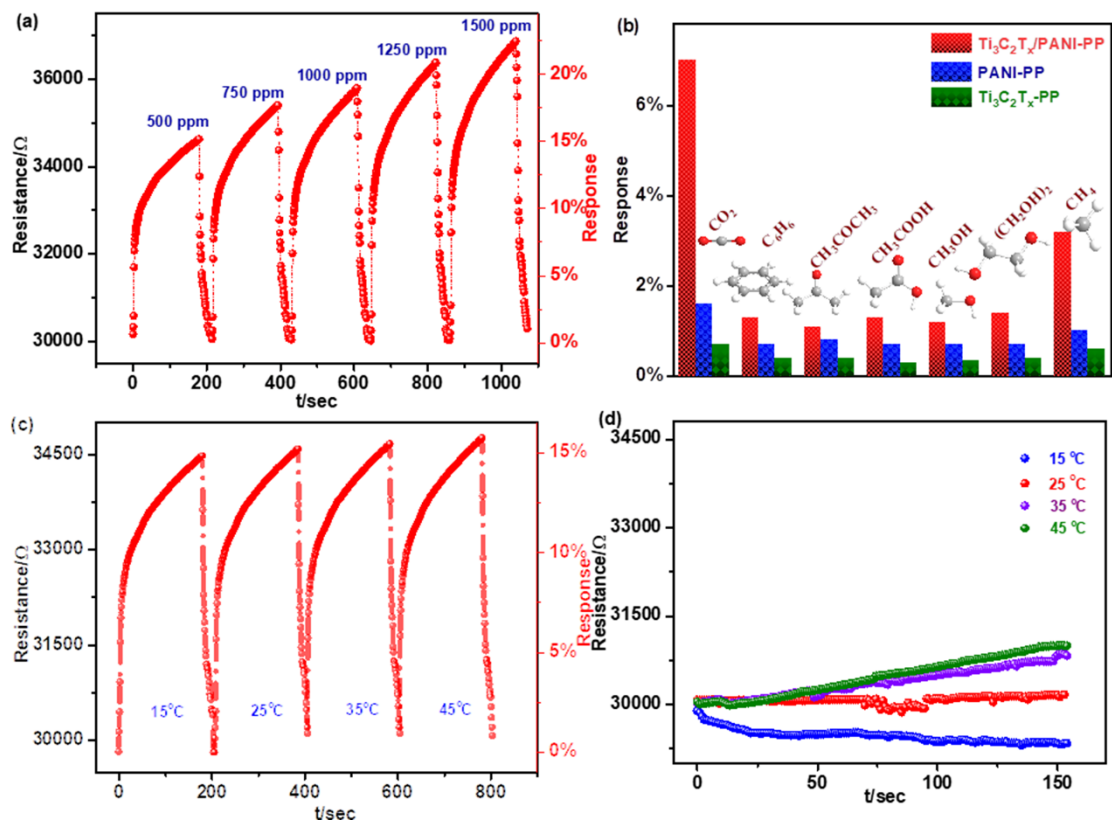
Figure 5-6. (a) The response-recovery of the $Ti_3C_2T_x$/PANI-PP sensor towards 500–1500 ppm CO_2. (b)The selectivity of the $Ti_3C_2T_x$/PANI-PP composite sensor to 200 ppm CO_2 and other various testing gases. (c, d) the temperature effect on the resistance changes of the $Ti_3C_2T_x$/PANI-PP sensor in 500 ppm target gas (c) and in the air (d).

To investigate the flexibility of the $Ti_3C_2T_x$/PANI-PP sensor, we conducted tests on the impact of folding and bending on its sensing properties. As shown in Figure S5b, there is no discernible change in response after folding the samples 10–30 times. The effect of bending states on the $Ti_3C_2T_x$/PANI-PP sensor was further examined, and the results were summarized in **Figure 5-7a**. There was only a slight difference observed among various bending degrees (0–120º), indicating the excellent flexibility of the $Ti_3C_2T_x$/PANI-PP sensor. Additionally, the long-term stability of the sensor was demonstrated in **Figure 5-7b**, where the response of the $Ti_3C_2T_x$/PANI-PP sensor

dropped from 15.2% to 14.2% after nine days, suggesting reliable stability. The slight decrease in response could be attributed to the partial oxidation of the $Ti_3C_2T_x$ MXene.

The influence of humidity on the $Ti_3C_2T_x$/PANI-PP sensor was further examined with and without CO_2 gas, as illustrated in **Figure 5-7c, 7d,** under an ambient environment (without target gas), the sensing response (negative value) of the $Ti_3C_2T_x$/PANI-PP sensor increased from 1.89% to 31.6% as the humidity increased from 12% to 90%. It is reported that the resistance of a sensor decreases as humidity increases due to the protonation of PANI by the additional hydrogen ions in the absorbed water [78, 79]. Besides, under CO_2 circumstance with the RH below 20%, an increase in humidity led to a continuous drop in the response curves. Interestingly, the response values exhibited an intriguing shift from positive numbers to negative as the humidity level increased from 50% to 70% RH in the presence of 1000 ppm CO_2. A similar shift was observed at different CO_2 concentrations, but lower CO_2 concentrations showed the shifting of resistance response at lower humidity levels (i.e.,200 ppm CO_2 presented the shift of response from 20% to 30%), as shown in Figure S6b. From the investigation of sensing response at different CO_2 and RH conditions, CO_2 concentration plays an important role in the generation of positive signals or increased resistance of the composite materials. This phenomenon may be due to the reaction between charged sites, such as H-bond accepting/donating sites [79, 80] (e.g., $-NH_2^+$, $-NH-$, $=NH^+$) and water molecules, the reaction between CO_2 and water molecules at varying humidity levels. When sensing 1000 ppm CO_2 at relatively low humidity levels (12%–50%), water molecules react with $-NH_2^+$ and CO_2 to generate H^+, which protonates PANI and reduces resistance. However, the high concentration of CO_2 is the primary factor causing distortion of the PANI chain and its absorption by MXene, leading to an increase in resistance. Therefore, the response remains positive even though resistance decreases with increasing humidity. Nevertheless, at very high

76

humidity levels (70%–90%), an excess of water molecules reacts with $-NH_2^+$ and CO_2, generating

a large number of H^+ ions that highly protonate PANI, leading to a significant reduction in

resistance and a negative response value. The relevant chemical reactions are shown in the

following Equations:

$$NH_2^+ + H_2O \rightarrow NH + H_3O^+ \qquad (2)$$

$$CO_2 + H_2O \leftrightarrow H^+ + HCO_3^- \qquad (3)$$
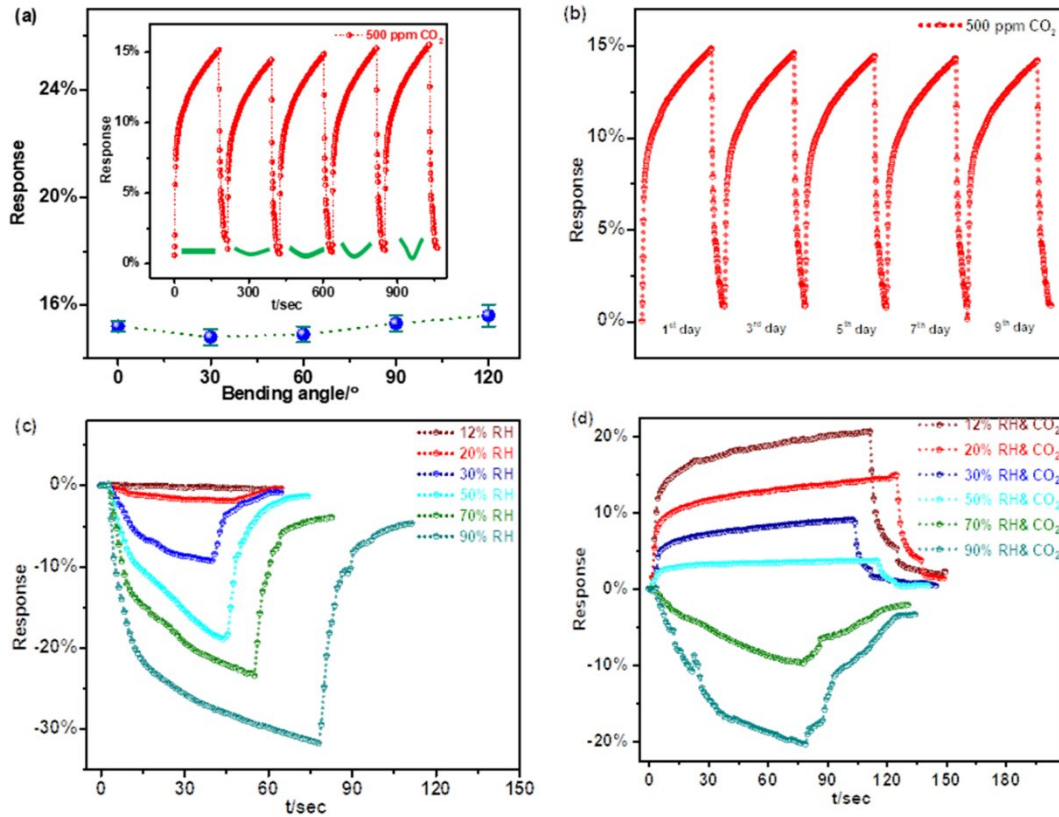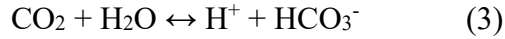
Figure 5-7. (a) The response of the $Ti_3C_2T_x$/PANI-PP sensor at different bending angles, (Inset is real-time response changes of the composite sensor towards 500 ppm CO_2 at 0, 30, 60, 90, 120 bending angles). (b) Stability of the $Ti_3C_2T_x$/PANI-PP sensor towards 500 ppm CO_2 at room temperature. (c) The response of the $Ti_3C_2T_x$/PANI-PP sensor under 12–90% RH conditions at room temperature (without target CO_2). (d) The response curves of the $Ti_3C_2T_x$/PANI-PP sensor under 12–90% RH conditions towards 1000 ppm CO_2 at room temperature.

Furthermore, the CO_2 gas sensing properties of PANI-based or $Ti_3C_2T_x$-based sensors in current work with previous studies were compared, as shown in **Table 5-1**. It is obvious that the $Ti_3C_2T_x$/PANI-PP sensor presents a good response value and short recovery time towards CO_2 gas, which are comparable and even better than previously reported results. The limit of detection (LoD) of the $Ti_3C_2T_x$/PANI-PP composite and other references. The results demonstrate that our composite sensor displays better CO_2 sensing performance than most of the previously reported CO_2 sensors. Moreover, by utilizing disposable masks as a flexible substrate for room-temperature sensing, we may contribute to reducing environmental pollution associated with mask waste.

Table 5-1. Comparison of the CO_2 gas sensing characteristics for PANI-based or $Ti_3C_2T_x$-based sensors in current work with previous studies.

Ref	Material	Response	Res	Substrate	RT
81	PANI/Cu	6.0% (10 ppm)	/	glass	√
42	PANI/NaO$_2$	60.0% (4200 ppm)	900/600 s	/	×
43	PANI/TiO$_2$	53% (1000 ppm)	9.2/5.7 min	glass	×
82	PANI/SnO$_2$	47.40% (5000 ppm)	35/43 s	epoxy	√
83	PANI/CLBC-AmG	10.0% (50 ppm)	20/75 s	cellulose	×
84	$Ti_3C_2T_x$-F	1.0% (30 ppm)	/	PI	√
85	Mo_2CT_x	1.14% (50 ppm)	/	Si	×
This work	$Ti_3C_2T_x$/PANI	15.2% (500 ppm)	115/26 s	PP	√

5.3.3 Sensing mechanism of $Ti_3C_2T_x$/PANI-PP sensor

The mechanism of a $Ti_3C_2T_x$ sensor can be based on the surface reactions of gaseous molecules with both defects and surface terminations. Specific sensing species attach to the structural defects of the $Ti_3C_2T_x$ MXene, while others bond and interact with surface functional groups, including $-O$ and $-OH$ [46]. As for our experiments, the p-type semiconducting behavior of the $Ti_3C_2T_x$-PP sensor can support that electron donor molecule of CO_2 are attributed to charge transfer from adsorbate CO_2 gas to the $Ti_3C_2T_x$, resulting in the decreased concentration of charge carriers or increased resistance [46]. Another reaction between oxygen species attached to the $Ti_3C_2T_x$ (e.g., Ti_3C_2O) MXene surface and CO_2 may be considered, resulting in the generation of $(CO_3)^{2-}$ and the release of thermal energy, as shown in Equation (4). This reaction decreases the electron density on the surface during the CO_2 sensing process, which leads to an increase in resistance [85, 86].

$$CO_2 + Ti_3C_2O_{x-y} + V_{Oy}^{¨} + \tfrac{1}{2} O_2 + 2e- \leftrightarrow (CO_3)^{2-} + Ti_3C_2O_x \quad (4)$$
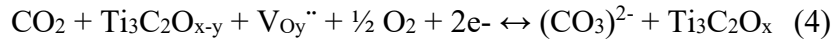
$V_{Oy}^{¨}$ is a Kröger-Vink notation of oxygen vacancies, which have two positive charges and are filled by the remaining 'x-y' surface oxygen atoms from the MXene.

The PANI sensor displays an increase in resistance when exposed to CO_2 in low humidity conditions (e.g., 12%). This phenomenon is likely caused by the reaction between the amino group of PANI and CO_2, as illustrated in Equation (5) and **Figure 5-8b**. CO_2 is an oxidizing gas that could form weak bonds with amine group on the PANI surface. The insertion of CO_2 to PANI sensor can cause the polymer structure to swell, negatively affecting the inter-chain conducting paths of charge carriers. Additionally, the weak bonding between COO^- group and PANI, resulting in polymer inter-chain swelling and intra-chain distortion, could also lead to an increase in resistance for the charge carrier transfer [38].

$$2R–NH + CO_2 \rightarrow R–NH_2^+ + R–NCOO^- \qquad (5)$$
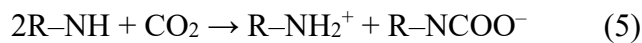
In addition, PANI, recognized as a well-known p-type semiconductor, has the majority of charge carriers in the form of polarons and bipolarons [87, 88]. It serves as the primary sensing material for CO_2 detection. **Figure 5-8c** illustrate the acid doping and de-doping process of PANI and the reversible reaction of PANI emeraldine base (EB) to emeraldine salt (ES) towards CO_2 gas under humidity conditions. Under high humidity circumstances (70–90%), the proton effect of hydrogen ions generated by water and carbonic acid (generated from the reaction between H_2O and CO_2) plays an important role in sensing mechanism [89]. The hydrophilic $Ti_3C_2T_x$ may also contribute to improving water molecule adsorption to accelerate those proton effects, leading to a continuous decrease in resistance with increased humidity [50].

Figure 5-8a, 8d, and 8e illustrate the improved sensing performance resulting from the $Ti_3C_2T_x$/PANI-PP composite structure, which can be attributed to the following synergistic effects: (1). Heterojunction between PANI and $Ti_3C_2T_x$: Several pieces of literature have indeed mentioned the formation of a Schottky junction at the interface between $Ti_3C_2T_x$ and PANI [62, 63, 70]. According to the literature [62], the work function of $Ti_3C_2T_x$ was measured to be 4.31 eV from the UPS results, in comparison to PANI's 4.8 eV. In another study [70], the work functions of $Ti_3C_2T_x$ and PANI/$Ti_3C_2T_x$ composite nanofibers were calculated to be 2.99 eV and 3.44 eV, respectively. The p-type semiconductor of PANI possesses a higher work function than $Ti_3C_2T_x$ [63]. In the presence of air, a Schottky junction forms at the interface of $Ti_3C_2T_x$ and PANI, creating a narrow hole depletion layer in PANI [62,71]. During the gas sensing process, CO_2 molecules are adsorbed by PANI, reducing the concentration of majority charge carriers and expanding the hole depletion region at the interface of the $Ti_3C_2T_x$/PANI-PP composite. This phenomenon restricts the conducting path, thereby boosting the sensing response. Furthermore, a p-n junction and a narrowed depletion layer may form between the n-type TiO_2 (originating from the partial oxidation

of $Ti_3C_2T_x$) and PANI at the composite interface [90-94], as depicted in Figure S9. The depletion layer's widening, resulting from the decrease in majority charge carriers by CO_2 molecules, enhances the heterojunction effects, thereby improving the sensing response of $Ti_3C_2T_x$/PANI-PP compared to $Ti_3C_2T_x$-PP or PANI-PP sensors. (2). Influence of $Ti_3C_2T_x$'s Properties: $Ti_3C_2T_x$, with its excellent metallic properties and the presence of abundant defects and functional groups such as –O and –OH on its surface, enhances charge transport and the density of efficient active sites. Additionally, these features facilitate reactions with CO_2 gas [50]. The XPS analysis shows that the content of –NH– groups increase after integrating $Ti_3C_2T_x$ during the PANI polymerization process. Consequently, more CO_2 is adsorbed, and the distortion of PANI chains intensifies, leading to significant resistance changes, and thus the $Ti_3C_2T_x$/PANI-PP composite shows superior sensing performance compared to pure PANI. (3). Impact of Porous Interface Structure: The porous interface structure of the $Ti_3C_2T_x$/PANI-PP composite increases the specific surface area, providing ample pathways for target gas diffusion and numerous adsorption sites. This, in turn, boosts the sensing performance [95].
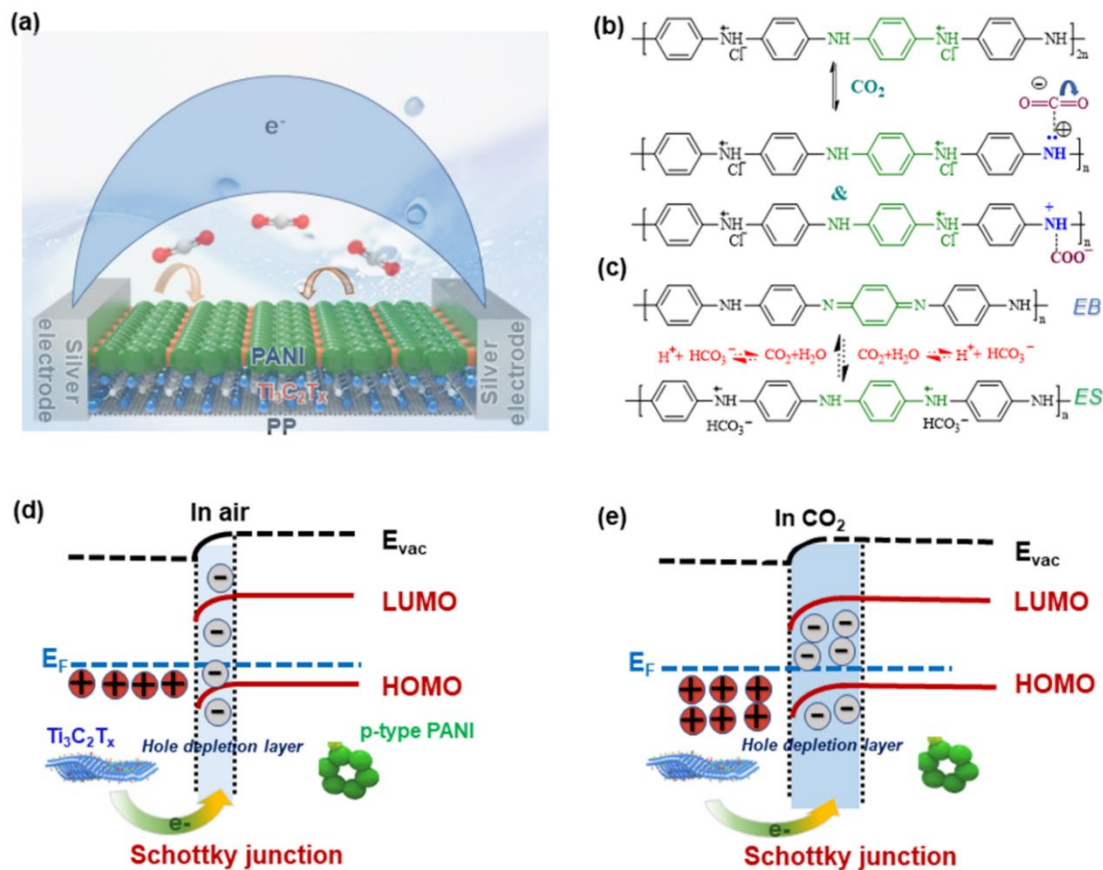
Figure 5-8. (a). The proposed CO_2 sensing mechanism of the $Ti_3C_2T_x$/PANI-PP composite. (b). The proposed chemical reaction between PANI-ES and CO_2 under dry or low humidity (< 20% RH) conditions. (c). The proposed chemical reaction between PANI and CO_2 under humidity conditions. The proposed Schottky junction of the $Ti_3C_2T_x$/PANI-PP composite sensor in air (d) and in CO_2 (e).

5.3.4 Wearable wireless Bluetooth sensing device for breath monitoring.

The human respiration rate can be monitored for potential respiratory issues and early breath-related disease diagnosis. To achieve this, we developed a wearable wireless Bluetooth sensing device by integrating the $Ti_3C_2T_x$/PANI-PP composite into a disposable mask, as illustrated in **Figure 5-9a**. The interface of WeChat applet "Wireless Bluetooth Sensor" is shown in Figure S10b, the resistance over time curve of human breath detection under high humidity conditions is illustrated in **Figure 5-9b** and Video S1. Different durations and intensities of exhaled breath have

a strong impact on the sensing response values and shapes. The average sensing response of the $Ti_3C_2T_x$/PANI-PP composite sensor towards fast, normal, and deep breaths was calculated as -9.26%, -15.38%, and -20.11%, respectively. The sensing performance of the $Ti_3C_2T_x$/PANI-PP composite is mainly attributed to the humidity and the CO_2 concentration (The concentration of CO_2 in exhaled breath of a human can exceed 3000 ppm at maximum) in exhaled breath, as temperature and bending angles have little effect on the sensing property. CO_2 gas molecules cause the sensor's resistance to increase, while humidity leads to a decrease in resistance due to the proton effect of water molecules. The negative signals indicate that humidity is the influencing factor for breath detection. Moreover, the higher the intensity of breath, the larger the humidity circumstance of the sensing device, which generates a stronger signal. Interestingly, the response curves went done with time due to the sluggish desorption of the composite sensor under extremely moist environments [38]. To measure CO_2 gas on human respiration rate detection without deconvolution of sensing signals, we utilized a non-woven fabric to reduce humidity (lower than 30% RH). As shown in **Figure 5-9c** and Video S2, the average response of the composite sensor towards fast, normal, and deep breaths was 4.55%, 14.94%, and 37.03%, respectively. These data demonstrate that the concentration of CO_2 plays an important role in respiration frequency monitoring. Additionally, as displayed in Figure S11, the $Ti_3C_2T_x$/PANI-PP composite sensor can maintain normal working within 10 min of the breath test, proving the ability to monitor respiratory rate with good stability of signals. All breath signals illustrate the rapid response/recovery time (a few seconds to a dozen). The wearable wireless Bluetooth sensing device we have developed is suitable for real-time monitoring of respiratory frequency, exhibiting significant promise for applications in respiratory system health care. Its ability to sensitively detect both CO_2 and humidity levels is essential for its utilization in respiratory healthcare. By carefully isolating the

influence of CO_2 and minimizing the impact of humidity, our system provides a sophisticated and novel approach to the real-time observation of respiration.
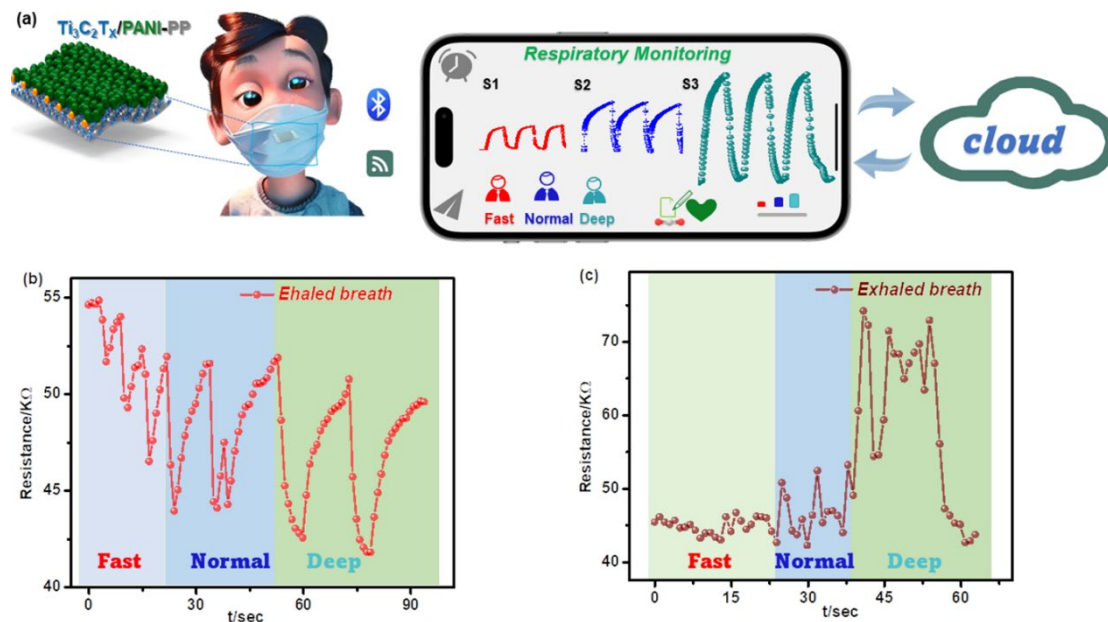
Figure 5-9. Schematic illustration of the $Ti_3C_2T_x$/PANI-PP-based wearable wireless Bluetooth sensing device for respiration monitoring. (a) Schematic of the disposable mask sensor device for wireless breath monitoring using a smartphone, with the ability to transmit various breath data to a portable device and update it to the cloud. (b) Resistance-time curve of human breath detection under high humidity conditions (> 90% RH). (c) Resistance-time curve of human breath detection under low humidity conditions (< 30% RH).

5.4 Conclusion

This study demonstrated a $Ti_3C_2T_x$/PANI-PP composite sensor by combing delimitated $Ti_3C_2T_x$ with PANI on a mask substrate. The optimized $Ti_3C_2T_x$/PANI-PP composite sensor displayed a superior response of 22.48% to 1500 ppm CO_2, high selectivity, satisfactory long-term stability and low limit of detection (2.21 ppm) at room temperature. More importantly, different degrees of resistance change were observed as a function of humidity levels and CO_2 concentrations. This phenomenon can be attributed to the reactions among the H-bond accepting/donating sites and

CO_2 gas on water molecules. The promoted sensing performance of the composite sensor can be mainly attributed to the Schottky junction between $Ti_3C_2T_x$ and PANI, and the enlarged specific surface area of the composite sensor. In addition, we demonstrated a wearable wireless Bluetooth sensing device to detect human exhaled breath, suggesting the $Ti_3C_2T_x$/PANI-PP composite sensor can be applied to human breath monitoring in real-time.

Chapter 6 Wearable Ethanol Sensor for Drunk Driving Monitoring Based on Ti$_3$C$_2$T$_x$/Polypyrrole Functionalized Face Mask

6.1 Introduction

Volatile organic compounds (VOCs) are significant hazardous air contaminants in industrial production and metropolitan life [152]. They evaporate into the environment at room temperature and atmospheric pressure, producing various harmful pollutants that can negatively affect the human nervous system, kidneys, and liver [153]. VOCs mainly include alcohols, acids, ketones, aldehydes, ethers, esters, etc., which can potentially lead to cancer and other major diseases, having long-term aggressive impacts on human health and air quality [154-156]. Besides, trace amounts of VOCs are present in the exhaled gases of the human body. They can serve as active biological markers for efficient early non-invasive disease analysis and diagnosis owing to their important physiological and metabolic-related information [76, 157, 158]. Among the VOCs, ethanol is the most widely used in biochemistry, pharmaceuticals, paints, and food and beverage industries [157, 159, 160]. Ethanol vapor is flammable that poses a vital risk of explosion and combustion, with an explosion limit of 3.3– 19.0% [161, 162]. According to the Occupational Safety and Health Administration (OSHA), exposure to ethanol vapor above 1000 ppm can cause headaches, drowsiness, difficulty in breathing, and adverse stimulation to the liver and eyes [163]. In addition, long-term exposure to ethanol environments as low as 25 ppm, may have negative effects on the human respiratory system, throat, and nervous systems, seriously threatening human health [164]. Furthermore, according to the accident survey conducted by the World Health Organization, approximately 50% to 60% of traffic accidents are attributed to drunk driving, which has been identified as the primary cause of fatalities in such incidents [165]. Therefore, detecting the ethanol content in air condition and in the

exhaled gases of vehicle drivers plays an important role in ensuring human health and avoiding drunk driving [166, 167].

Various methods such as tuning fork [168], photo-ionization detector (PID) [169], mass spectrometry (MS) [32], high performance liquid chromatography (HPLC) [170], micro gas chromatography [171], and quartz crystal microbalances (QCM) [172] are widely used for precise detecting VOCs. However, these conventional techniques have some significant drawbacks, such as their large volume, time-consuming analysis, high energy consumption, and expensive and complicated equipment requirements [54, 55, 93]. Over the past two decades, researchers have shown considerable interest in developing gas sensors for monitoring inflammable, toxic, and harmful gases using p-type metal oxide semiconductors (MOSs) such as NiO [173], CuO [135], and Co_3O_4 [174], n-type MOSs like ZnO [175], TiO_2 [13], and SnO_2 [176], and perovskite-structured materials such as $LaCoO_3$ [177] and $BaMnO_3$ [178]. For instance, Zoolfakar et al. [179] developed an ethanol vapor gas sensor based on a highly crystalline and nanostructured p-type CuO , which was fabricated through radio frequency sputtering at a supply power of 200 W at 120°C. This sensor demonstrated remarkable sensing performance with a response value of 2.2 towards 12.5 ppm ethanol at an optimum operating temperature of 180°C. Qin et al. [180] synthesized a $LaCoO_3$/ZnO nano-flake composite through a sol-gel method. The $LaCoO_3$/ZnO sensor exhibited a response value of 55 towards 100 ppm ethanol at 320°C, which is six times higher than a pristine ZnO gas sensor. Nevertheless, these MOSs and perovskite-structured gas sensors have striking limitations, including high energy consumption, inflexible and fragile characteristics, and a requirement for high-temperature operation [94, 95, 97].

Currently, there is significant interest in developing portable, flexible, and room-temperature gas sensors for trace ethanol detection [181, 182]. Intrinsic conducting polymers (ICPs), such as polyaniline (PANI) [140, 144], poly(styrene sulfonate) (PSS) [183], and polypyrrole (PPy) [102], have attracted substantial attention in gas sensors due to their easy synthesis, low operating temperature, good mechanical properties and electrical conductivity. However, the poor long-term stability and slow response time have limited their potential applications [140]. To address these issues, ICP-based composites, such as PANI/silver [184], PANI/TiO$_2$ [185], PPy/PVA [186], and PPy/MoO$_3$ [187], have been developed for ethanol sensing. For example, Yenorkar et al. [188] synthesized a PPy-MoO$_3$ composite film sensor for ethanol detection. The results showed that the composite sensor exhibited a sensitivity of 70%, which is 3.5 times higher than that of the pure PPy sensor.

Two-dimensional (2D) materials, such as black phosphorus (BP), graphene, graphene oxide (GO), hexagonal boron nitride (h-BN), and transition metal dichalcogenides (TMDs), have also been employed in flexible gas sensors due to their versatile surface chemistry, low electronic noise, large specific surface area, and outstanding electrical properties [50, 153, 189, 190]. However, their relatively low sensitivity and interference from humidity limit their sensing applications. MXenes are relatively newly discovered 2D materials that have attracted wide attention in various fields, including sensors, biosensors, water purification, electromagnetic shielding, and energy storage devices due to their exceptional electronic and magnetic properties, high flexibility, and favorable hydrophilic surface, and their surface functionalities can be adjusted to various requirements [148, 191]. Kim et al. [192] prepared a Ti$_3$C$_2$T$_x$ MXene sensor via vacuum filtration method on SiO$_2$/Si substrate, showing a response value of 1.7% to ethanol gas, remarkable selectivity, and a ppb-level detection limit at room temperature. However, pristine MXenes suffer from shortcomings, such as relatively low sensing response and low stability under oxidative environments [42]. Therefore,

MXene-based composites are being investigated to improve sensing performance. Zhang et al. [193] synthesized a $MoO_3/Ti_3C_2T_x$ nanocomposite ethanol sensor by hydrothermal method, achieving a low-concentration limit of 1 ppm, outstanding selectivity and reproducibility, and a high response of 5.42 towards ethanol gas, which is over twice higher than the sensing response of pure MoO_3 or $Ti_3C_2T_x$ sensors. Bu et al. [194] fabricated a $Co_3O_4/Ti_3C_2T_x$ hybrid ethanol sensor by calcining the ZIF-67 precursor grown on the $Ti_3C_2T_x$ sheets, demonstrating an ultra-high response (190 towards 50 ppm ethanol, which is at least 15 times higher than that of pristine Co_3O_4 or $Ti_3C_2T_x$ sensor).Recently, the fabrication of composites (e.g., $PPy/Ti_3C_2T_x$) based on ICPs and MXenes has been investigated for various applications such as supercapacitor [195], electromagnetic interference shielding [196], rechargeable batteries [197], and anticorrosive bipolar plates [198]. To the best of our knowledge, there is no previous attempt at the synthesis of $PPy/Ti_3C_2T_x$ composites for ethanol sensing applications. It is hypothesized that combing PPy with $Ti_3C_2T_x$ might be an efficient approach for making high-performance ethanol sensors due to the synergistic effects between redox-active PPy and highly conductive $Ti_3C_2T_x$.

Henein, we developed a flexible $PP/Ti_3C_2T_x/PPy$ composite sensor by drop-coated $Ti_3C_2T_x$ MXene suspension and chemical polymerization of pyrrole on a disposable face mask (mainly made up of polypropylene (PP)) surface. The resulting sensor demonstrated excellent sensing properties. Besides, we investigated the impact of humidity, synthesis orders, bending states, and temperature on the sensing performance of the composite sensor. Finally, we designed a portable and wearable Bluetooth sensor module for detecting alcohol in human breath, indicating that the $PP/Ti_3C_2T_x/PPy$ sensor can be utilized for human drunk driving monitoring.
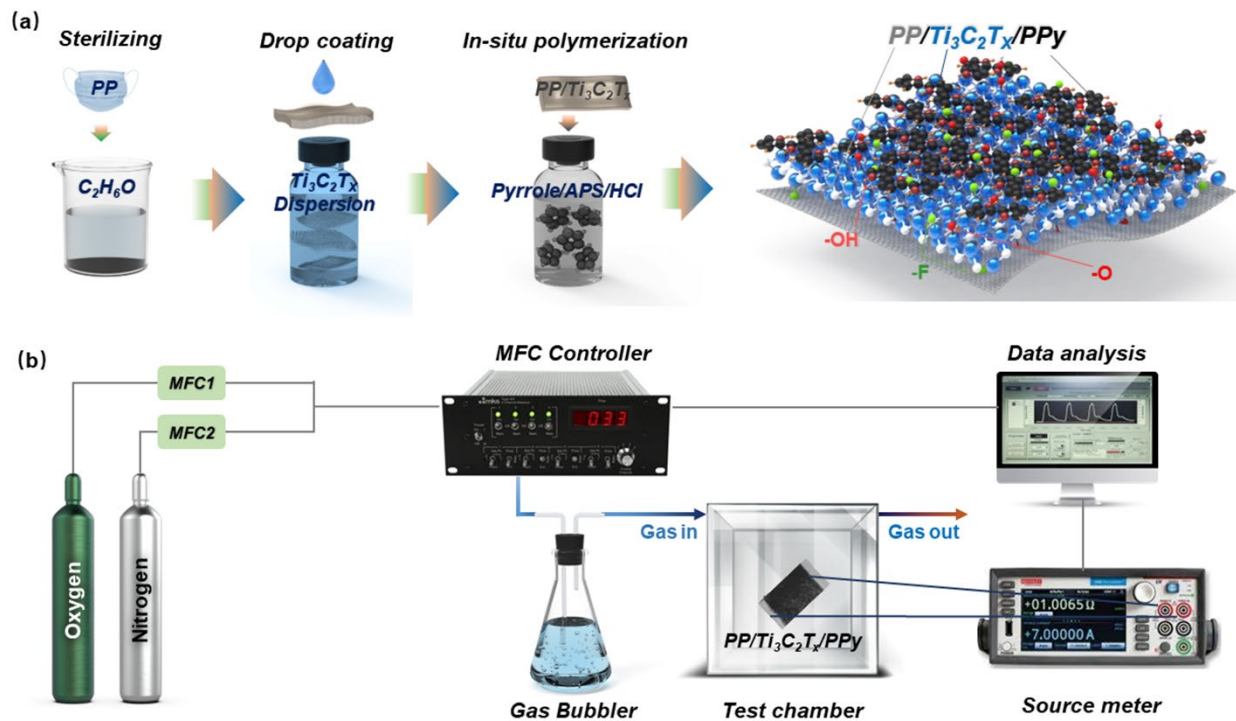
Figure 6-1. (a) Schematic of the wearable PP/Ti$_3$C$_2$T$_x$/PPy fabric sensor synthesis process. (b) Schematic diagram of the gas sensing setup.

6.2 Experimental section

6.2.1 Materials

Disposable face masks were obtained from Wenzhou Chengmu Trading Company (Wenzhou, Zhejiang, China). The polypropylene (PP) layer of the face mask is served as a substrate for the sensors. [NH$_4$]$_2$S$_2$O$_8$ (APS), and 36-38% hydrochloric acid were purchased from Sigma-Aldrich. LiF (98.5% purity), Ti and Al powder (325 mesh), and pyrrole monomer were purchased from Alfa Aesar. Silver paint and HF (48-51%) were purchased from VWR, USA.

6.2.2 Preparation of Ti$_3$C$_2$T$_x$ Solution

The Ti$_3$AlC$_2$ Max Phase and delaminated Ti$_3$C$_2$T$_x$ MXene solution were fabricated according to previous reports in the literature [54]. In summary, 1 g of Ti$_3$AlC$_2$ powder was etched in a 20 mL

mixture of 12 M HCl and HF at 35°C for 24 h. After etching, the powder was washed at least 5 times with deionized (DI) water and centrifuged at 4000 rpm for 5 min to obtain the supernatant. Afterward, the sediment was mixed with a 50 mL solution containing 1g LiCl and stirred for 18h. Then, the mixture was centrifuged at 4000 rpm for 5 min. The centrifuging was repeated until the dark supernatant remained. The resulting MXene solution was stored in a fridge.

6.2.3 Preparation of PP/Ti$_3$C$_2$T$_x$ Sensor

The PP substrate was cleaned with ethanol and DI water to remove any contaminants. Then, the prepared Ti$_3$C$_2$T$_x$ MXene solution was drop-coated evenly onto the PP fabric surface. After air drying, the Ti$_3$C$_2$T$_x$ suspension was coated onto the PP surface again to synthesize the PP/Ti$_3$C$_2$T$_x$ sensor.

6.2.4 Preparation of PP/Ti$_3$C$_2$T$_x$/PPy Sensor

The preparation process involved the addition of 0.6 mL pyrrole monomer to 200 mL of 1 M HCl solution in a 400 mL beaker, followed by the addition of 0.69 g of APS dissolved in 40 mL of 1 M HCl solution and then the APS-HCl solution was mixed with the pyrrole-HCl suspension at room temperature. The PP substrate and PP/Ti$_3$C$_2$T$_x$ were dipped in the mixed suspensions, and the polymerization reaction was performed by magnetic stirring at 30°C for 65 min. The resulting PP/PPy and PP/ PP/Ti$_3$C$_2$T$_x$/PPy composites were cleaned with DI water three times and dried in an oven at 40°C for 7 h. After drying, all the samples were cut into 20 mm x 10 mm pieces. Then, the composite fabrics were coated with silver paint. **Figure 6-1a** illustrates the synthesis process of the PP/Ti$_3$C$_2$T$_x$/PPy composite sensor.

6.2.5 Sensing Measurements.

To investigate the sensing performance, the as-prepared samples were placed in a closed chamber and the electrical resistance change was measured by a Kethley 2400 source meter. The gas

bubbling method was used to generate ethanol vapor. A flow of 80 sccm nitrogen was separated into two parts using a mass flow controller: a carrier part and a dilution part. The carrier part was bubbled through the liquid analyte of interest and then mixed with the diluted air in the test chamber. The operations were conducted at room temperature ($23.5\pm1°C$), and the atmospheric conditions were maintained during the experiment. The data collection and management were carried out using a specialized Labview program. The gas response value of the composite fabrics follows below equation:

$$R= (R_g - R_0)/R_0 * 100\% \tag{1}$$

where R_0 and R_g are the electrical resistance of the PP/$Ti_3C_2T_x$/PPy sensor exposed to the air and the target gas.

6.2.6 Wireless Bluetooth Sensor Module for Alcohol Intoxication Detection.

PP/$Ti_3C_2T_x$/PPy hybrid film was affixed to the surface of a disposable medical mask for alcohol breath detection. The Bluetooth sensor module was connected to the mask-sensing device, and a 5 V power bank was used to supply the voltage required by the sensor module. The resistance changes of the PP/$Ti_3C_2T_x$/PPy hybrid sensor were recorded using the WeChat applet "Wireless Bluetooth Sensor" for the alcohol test. During the alcohol breath test, a volunteer drank 60 mL of whiskey (50% ALC/VOL, 100 PROOF) and underwent alcohol breath tests at 20, 30, 40, 50, 55, 60, and 65 min, after drinking, respectively. Furthermore, the blood alcohol concentration (BAC) was determined by calibrating a commercial AD-8000 breathalyzer (2022 Upgrade Professional-Grade Accuracy Alcohol Tester, available on Amazon). After a certain duration of time since consuming alcohol, the volunteer took a deep breath and exhaled for approximately 4 seconds. The breathalyzer then provided the BAC value.

6.2.7 Characterization

The morphology and qualitative elemental analysis of the hybrid sensor were examined using a scanning electron microscope (JEOL JSM-7000F) equipped with an energy dispersive spectrometer mapping. The surface bonding of the hybrid films was investigated by FT-IR using a Thermo Nicolet 6700 instrument. Additionally, N_2 adsorption and desorption isotherms were collected to investigate the Barrett-Emmett-Teller (BET) surface area of the hybrid films. The pore size distribution of the hybrid films was analysed using the Barrett−Joyner−Halenda (BJH) method with a Quanta chrome NOVA 2200e instrument. The surface topography of the $Ti_3C_2T_x$ was characterized using an atomic force microscope (AFM, Park Instruments NX10). The valence states of elements were analysed using X-ray photoelectron spectroscopy through K-alpha (Thermo Scientific Inc., U.K.).

6.3 Results and discussion

6.3.1 Materials Characterization**.**

SEM imaging was employed to investigate the morphology of PP, PP/PPy, PP/$Ti_3C_2T_x$, and PP/$Ti_3C_2T_x$/PPy hybrid. The PP fabric presents a straight rod-like fibrous structure, as depicted in **Figure 6-2a**. As shown in **Figure 6-2b**, the layered structure of $Ti_3C_2T_x$ aggregated at the PP fiber surface, indicating the successful delamination process of $Ti_3C_2T_x$. **Figure 6-2c** clearly illustrates that the PP substrate is covered by a mass of irregular spherical PPy particles. Additionally, **Figure 6-2d** reveals that PPy is surrounded by some of the single-layer $Ti_3C_2T_x$, indicating that PPy was *in situ* polymerized on the Ti_3C_2Tx, and formed a well-combined structure with a porous surface, which facilitates gas adsorption and diffusion [44].
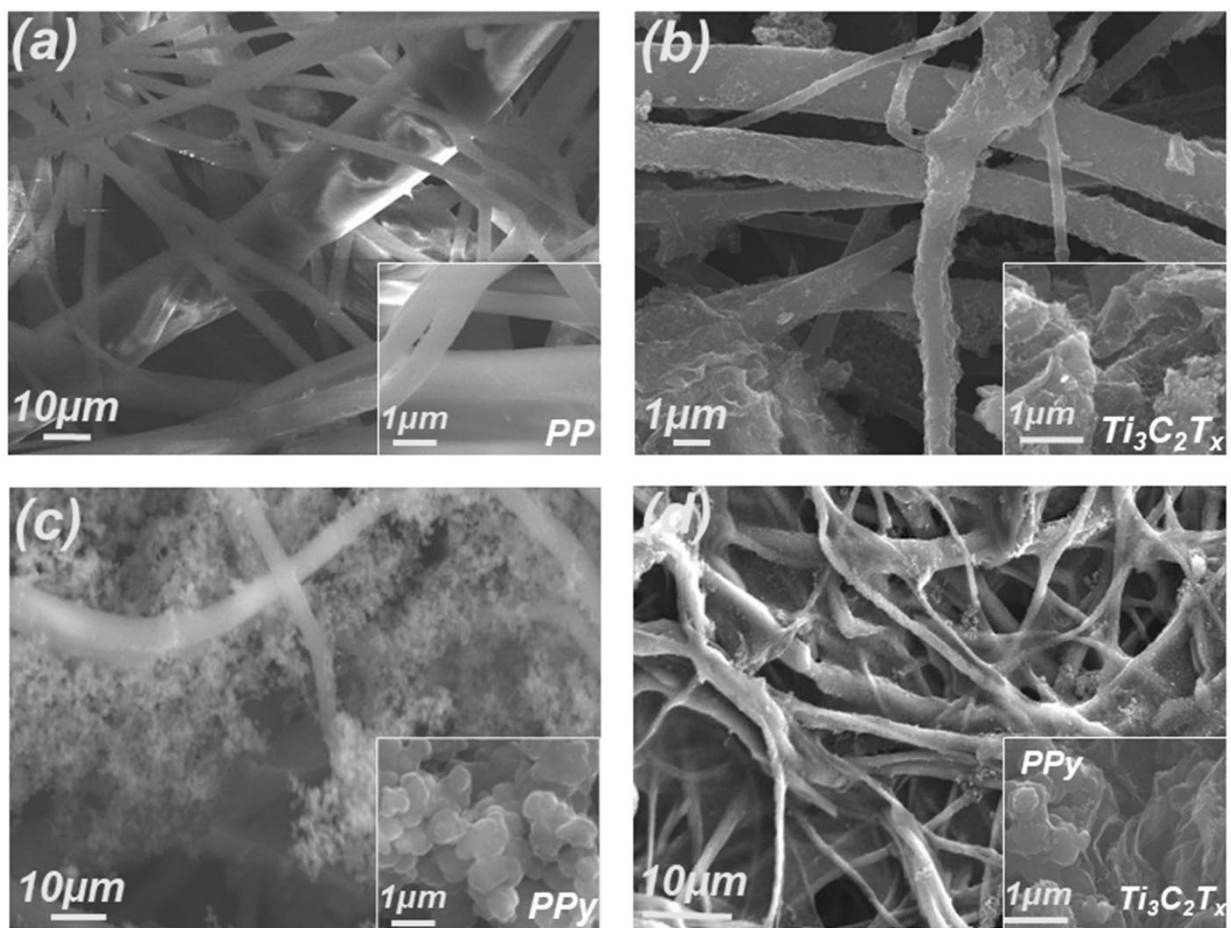
Figure 6-2. SEM images of (a) PP, (b) PP/Ti$_3$C$_2$T$_x$, (c) PP/PPy, and (d) PP/Ti$_3$C$_2$T$_x$/PPy.

EDS mapping was conducted to investigate the surface elemental distribution in the PP/Ti$_3$C$_2$T$_x$/PPy hybrid, and the results are presented in **Figure 6-3b–h**. The results revealed the presence of Cl, Ti, O, N, C, and F elements in the composite fabric. The element weight percentage and atomic percentage are presented in **Figure 6-3i**, which further indicates the successful incorporation of PPy on the Ti$_3$C$_2$T$_x$. **Figures 6-3j** and **3k** show the AFM images of Ti$_3$C$_2$T$_x$, demonstrating that the delaminated Ti$_3$C$_2$T$_x$ are predominantly single layers with a thickness of 1.43 nm. The electrode structure of the PP/Ti$_3$C$_2$T$_x$/PPy composite sensor is illustrated in **Figure**

6-3l. The application of silver paint on both sides of the composite sensor is to reduce contact resistance.
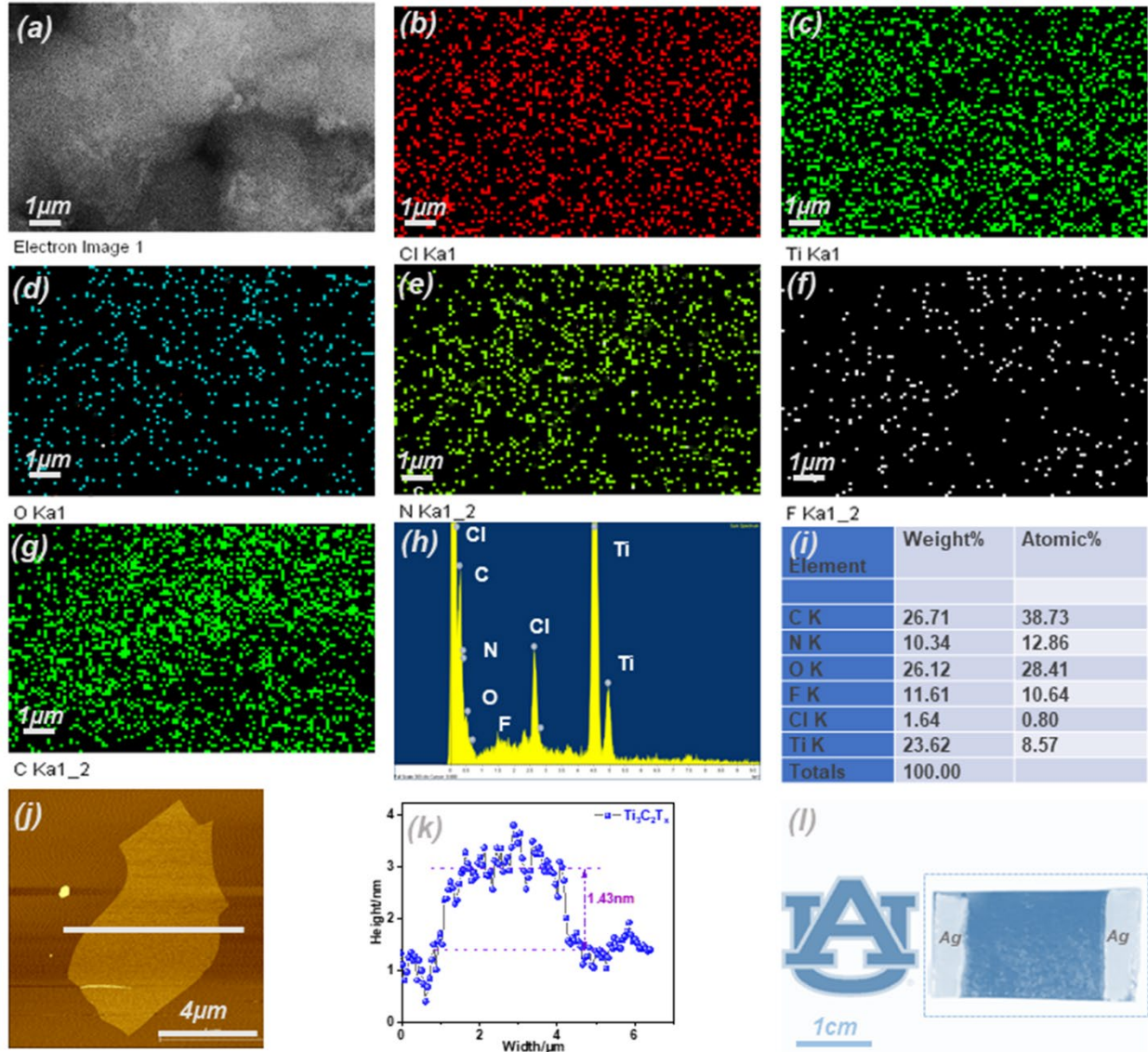
Figure 6-3. Typical EDS elemental mapping of the PP/Ti$_3$C$_2$T$_x$/PPy composite: (a) Magnified SEM image of **Figure 6-2d**. (b–g) The distribution of Cl, Ti, O, N, C, and F elements. (h) EDS spectra of the PP/Ti$_3$C$_2$T$_x$/PPy composite. (i) The weight and atomic percentage of each element in the PP/Ti$_3$C$_2$T$_x$/PPy composite. (j–k) AFM image and the corresponding height and width profile of the Ti$_3$C$_2$T$_x$ flake. (l) The electrode structure of the PP/Ti$_3$C$_2$T$_x$/PPy composite sensor.

FT-IR was conducted to examine the surface chemistry of PP, PP/PPy, PP/Ti$_3$C$_2$T$_x$, and PP/Ti$_3$C$_2$T$_x$/PPy, as shown in **Figure 6-4a**. The bands at 2922 cm^{-1}, 1450 cm^{-1}, 1390 cm^{-1}, 1165 cm^{-1}, and 842 cm^{-1} in PP film can be attributed to –CH$_2$ asymmetric stretching, –CH$_2$ symmetric bending vibration, –CH$_3$ symmetric bending, –CH$_3$ rocking vibration, and C–CH$_3$ stretching, respectively [64, 65]. The peaks at 1536 cm^{-1}, 1292 cm^{-1} in PP/PPy correspond to C=C stretching vibrations of the pyrrole ring and C–H or C–N in-plane deformation [66, 67]. The absorption peaks observed at 1651 cm^{-1}, 1367 cm^{-1}, 1202 cm^{-1}, and 1002 cm^{-1} in PP/Ti$_3$C$_2$T$_x$ are due to C=O bonding, molecular water (O–H), oxygen group vibration and C–F vibration [68]. The intensities of the bands corresponding to –O, –OH, and –F functional groups of Ti$_3$C$_2$T$_x$ (1651, 1367, 1202, and 1002 cm^{-1}) are observed to decrease in the PP/Ti$_3$C$_2$T$_x$/PPy, which is mainly due to the formation secondly bonding (e.g., Van der Waals forces) of deposition of PPy on Ti$_3$C$_2$T$_x$ MXene [69]. As shown in **Figure 6-4b**, Raman shifts of the PP/Ti$_3$C$_2$T$_x$/PPy composite revealed a significant decrease in the intensity of Ti$_3$C$_2$T$_x$ peaks (specifically, 1316 and 1603 cm^{-1} which are assigned to carbon atomic lattice defects and the stretching vibration of carbon atoms in the SP2 hybridization plane) after the PPy deposition [60]. In addition, the characteristic peaks of Ti$_3$C$_2$T$_x$ at 425 and 579 cm^{-1} are owing to Ti-C bond vibration, and the characteristic peaks of PPy at 1356 and 1620 cm^{-1} are attributed to the C–N bond stretching and C-C stretching of the pyrrole ring [70]. All these characteristic peaks indicated the successful fabrication of the PP/Ti$_3$C$_2$T$_x$/PPy composite.
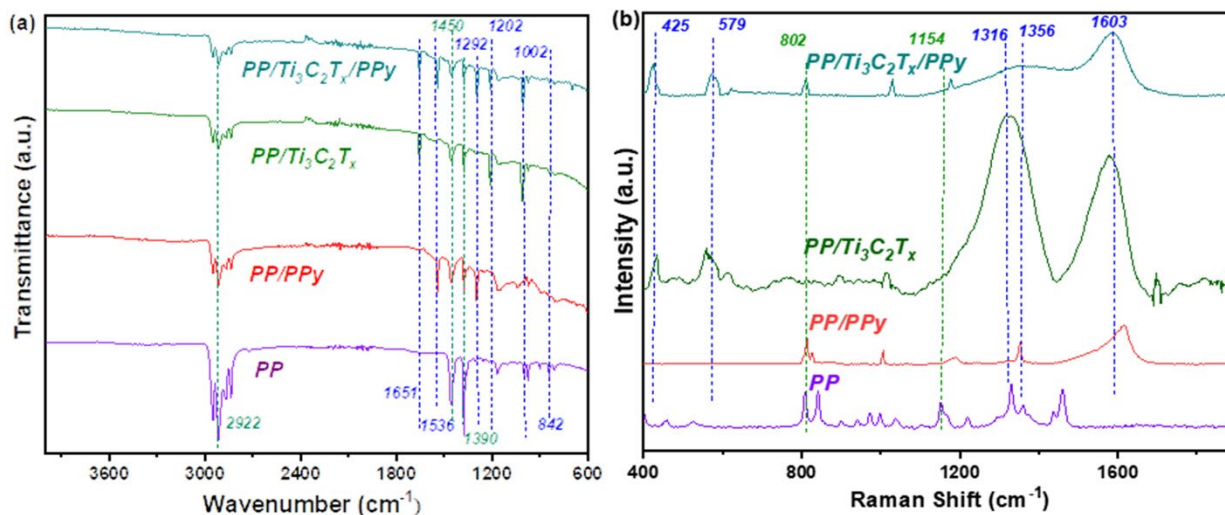
Figure 6-4. (a). FTIR spectra and (b) Raman spectra of PP, PP/PPy, PP/Ti$_3$C$_2$T$_x$, and PP/Ti$_3$C$_2$T$_x$/PPy.

The XPS spectra were used to determine the surface element information and functional groups of PP/Ti$_3$C$_2$T$_x$ and PP/Ti$_3$C$_2$T$_x$/PPy hybrid. The survey scan of PP/Ti$_3$C$_2$T$_x$ and PP/Ti$_3$C$_2$T$_x$/PPy in **Figure 6-5a** showed the presence of C, N, O, Ti, and F elements, indicating the combination of PPy and Ti$_3$C$_2$T$_x$. The C 1s signals in **Figure 6-5b** were concentrated around 281.9, 284.3, 285.4, and 287.4 eV, which were attributed to C–Ti, C–C, C–N, and C–O/C=O, respectively. The N 1s signals in **Figure 6-5c** were deconvoluted into three peaks centered at 398.7, 399.9, 401.9, corresponding to –N$^+$, –NH–, =NH, respectively. The amino groups in PPy may play an important role in promoting the formation of hydrogen bonding with ethanol molecules, which could improve the sensing performance of the composite [44]. The O 1s spectrum in **Figure 6-5d** showed peaks at 530.1, 531.0, 532.5 eV, representing Ti–O, C–Ti–O, and Ti–OH, respectively, indicating the abundant surface terminal groups of oxygen and hydroxyl groups on the composite, these terminal groups are conducive to form hydrogen bonding with ethanol molecules to facilitate the sensing signals. [60]. The high-resolution F1s spectrum in **Figure 6-5e** showed peaks at 683.1 and

684.4 eV, ascribed to Ti–F and C–F, respectively. The Ti 2p core level in **Figure 6-5f** was fitted

with 3 different doublets (Ti $2p_{1/2}$ and Ti $2p_{3/2}$), and the Ti $2p_{3/2}$ peaks at 455.2, 456.4, 458.2 eV

were attributed to Ti–C, Ti^{2+}/Ti^{3+}, and Ti–O (Ti^{4+}), respectively. These results suggest the partial

oxidation of $Ti_3C_2T_x$.
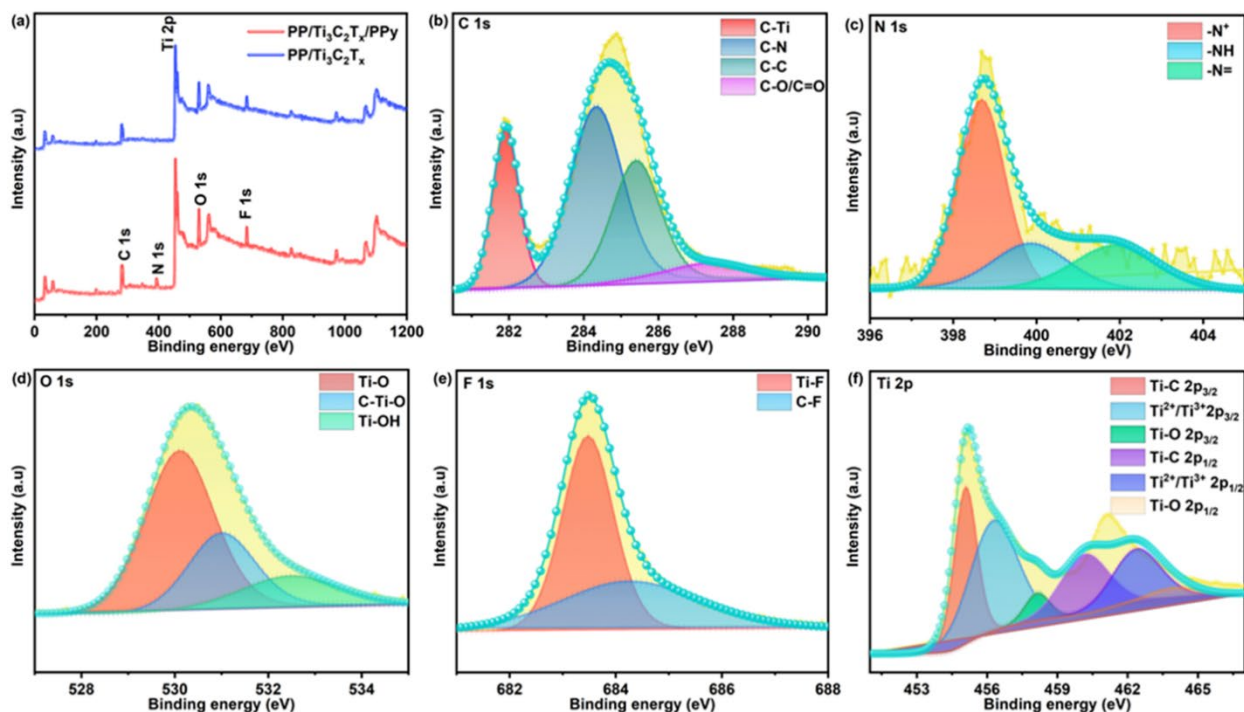
Figure 6-5. (a) The survey spectra of PP/$Ti_3C_2T_x$ and PP/$Ti_3C_2T_x$/PPy hybrid. (b–f) C 1s, N 1s, O 1s, F 1s, and Ti 2p spectra of the PP/$Ti_3C_2T_x$/PPy hybrid.

The N_2 adsorption-desorption (BET) curves and BJH pore volume distribution as a function of the

pore size are shown in Figure S1a–d. The specific surface areas measured by the BET equation

were 53.612, 60.123, 70.242, and 84.903m^2g^{-1} for PP, PP/PPy, PP/$Ti_3C_2T_x$, and PP/$Ti_3C_2T_x$/PPy,

respectively. Obviously, the PP/$Ti_3C_2T_x$/PPy composite displayed broader pore-size distribution

with more pores and possessed the highest specific surface area among all the samples. The porous

structure and the increased surface area of the PP/$Ti_3C_2T_x$/PPy will be beneficial to enhance

sensing characteristics.

6.3.2 Gas-Sensing Properties.

The sensing performance of PP/PPy, PP/Ti$_3$C$_2$T$_x$, and PP/Ti$_3$C$_2$T$_x$/PPy sensors were assessed at room temperature. The resistance baseline of the PP/Ti$_3$C$_2$T$_x$/PPy hybrid sensor was monitored over time, ranging from 10 ppm to 400 ppm, as shown in **Figure 6-6a**. For comparison, the baseline resistance curves of PP/PPy and PP/Ti$_3$C$_2$T$_x$ towards 400 ppm ethanol are shown in Figure S2. The initial resistance of the PP/Ti$_3$C$_2$T$_x$/PPy sensor was 10.5 KΩ, whereas the resistance of the PP/PPy sensor was 39.8 KΩ. This indicates that adding metallic MXene significantly enhances the conductivity of the hybrid sensor. As presented in **Figure 6-6b**, the resistance and response of all three sensors increased with the increased concentration of ethanol vapor. This might be due to the formation of more hydrogen bonds among Ti$_3$C$_2$T$_x$, PPy, and ethanol molecules. The sensing response of PP/PPy, PP/Ti$_3$C$_2$T$_x$, and PP/Ti$_3$C$_2$T$_x$/PPy hybrid sensors improved as the concentration of gas increased, with the response value of 18.1%, 35.5%, and 76.3% under 400 ppm ethanol, respectively. Notably, the PP/Ti$_3$C$_2$T$_x$/PPy hybrid sensor had a lower detection limit toward ethanol vapor (e.g., 10 ppm). The gas sensing response of PP/Ti$_3$C$_2$T$_x$ and PP/Ti$_3$C$_2$T$_x$/PPy sensors as a function of concentration is presented in **Figure 6-6c**, showing the excellent linear relationship between the sensor response and ethanol concentration. As shown in **Figure 6-6d**, the PP/Ti$_3$C$_2$T$_x$/PPy sensor had an admirable sensing property, with a response time of 49s and a recovery time of 18s. Furthermore, we investigated the impact of different synthesis orders on the sensing performance, as presented in Figure S3. The PP/PPy/Ti$_3$C$_2$T$_x$ hybrid sensor exhibited an average response value of only 50.1%, which was much lower than that of the PP/Ti$_3$C$_2$T$_x$/PPy sensor (76.3%). This could be attributed to the weaker bonding (e.g., van der Waals forces) between PP and PPy compared to that between PP and Ti$_3$C$_2$T$_x$, as evidenced by the SEM characterization of the PP/PPy and PP/Ti$_3$C$_2$T$_x$ films. This weakened bonding results in a reduced

deposition of both PPy and Ti₃C₂Tₓ onto the PP substrate. As a result, there is a decrease in the interaction with ethanol molecules, leading to a lower response value.
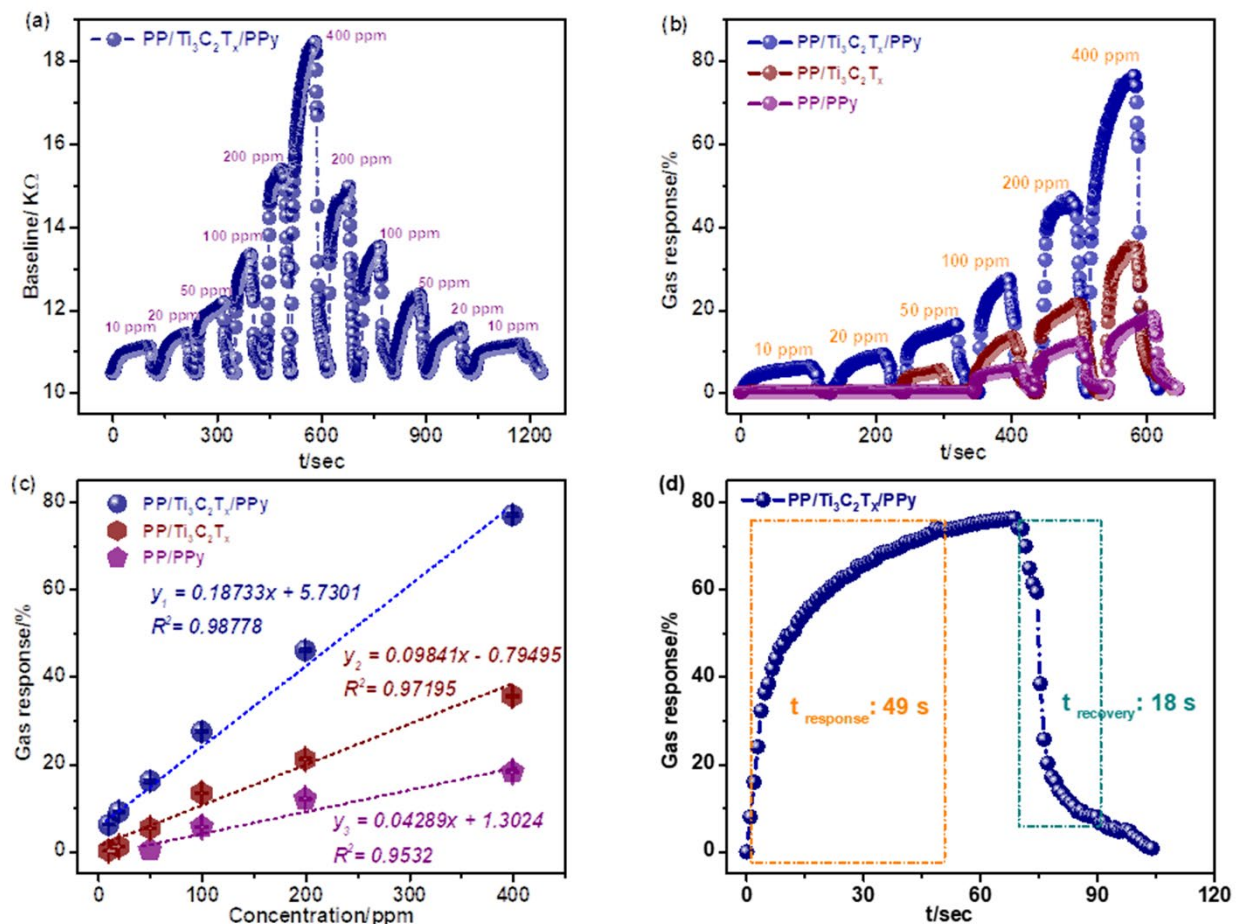
Figure 6-6. (a) The real-time resistance baseline of the PP/Ti₃C₂Tₓ/PPy hybrid sensor ranges from 10 ppm to 400 ppm. (b) The dynamic response/recovery curves of PP/Ti₃C₂Tₓ, PP/PPy, and PP/Ti₃C₂Tₓ/PPy composite sensors. (c) Sensing response of PP/Ti₃C₂Tₓ and PP/Ti₃C₂Tₓ/PPy sensors as a function of ethanol concentration ranging from 10-400 ppm at room temperature. (d) The change of response as a function of time shows the response and recovery time. Note: the relative humidity in the test chamber was 12–18%.

Selectivity is a vital parameter for assessing gas sensors. Therefore, the selectivity of the PP/Ti₃C₂Tₓ/PPy sensor was examined by comparing ethanol with various organic or inorganic gases, such as acetone, acetic acid, benzene, methane, ammonia, carbon monoxide, carbon dioxide, and hydrogen sulfide, as shown in **Figure 6-7a**. The responses towards the above gases were

76.3%, 25.2%, 20.3%, 29.4%, 11.2%, 38.8%, 19.1%, 13.0%, and 9.2%, respectively, implying good selectivity of the PP/$Ti_3C_2T_x$/PPy sensor towards ethanol. Furthermore, the reproducibility of resistance baseline and response changes for the PP/$Ti_3C_2T_x$/PPy composite sensor to 400 ppm ethanol is depicted in **Figure 6-7b**, showing the reliable reproducibility of the hybrid at room temperature. To further study the gas sensing properties of the PP/$Ti_3C_2T_x$/PPy hybrid, we investigated the impact of humidities, temperatures, and bending states on the sensing response. **Figure 6-7c** displays the humidity effect on the sensing response changes of the PP/$Ti_3C_2T_x$/PPy composite towards 400 ppm ethanol. The sensing response of the PP/$Ti_3C_2T_x$/PPy composite showed an obvious decrease with the increase of humidity (15–75% RH), i.e., the response value dropped from 76.3% to 10.8%. This observation might be attributed to the inhibition of the sensing reaction (e.g., hydrogen bonding) between $Ti_3C_2T_x$ and ethanol at high humidity due to the hydrophilic nature of the $Ti_3C_2T_x$ terminated by functional groups (e.g., –OH, –O, –F) [59]. Additionally, the presence of water molecules on the $Ti_3C_2T_x$/PPy active surface may lead to a decrease in gas adsorption sites, obstructing ethanol adsorption and further reducing the response [59, 71]. Furthermore, the temperature effect on the response change of the PP/$Ti_3C_2T_x$/PPy hybrid towards 400 ppm ethanol gas ranging from 20°C to 40°C is presented in **Figure 6-7d**. The PP/$Ti_3C_2T_x$/PPy sensor showed a slight decrease in response with the increase in temperature, which might be due to the enhanced desorption of ethanol at higher temperatures, leading to a reduction in resistance and subsequently a decrease in the sensing response [72].
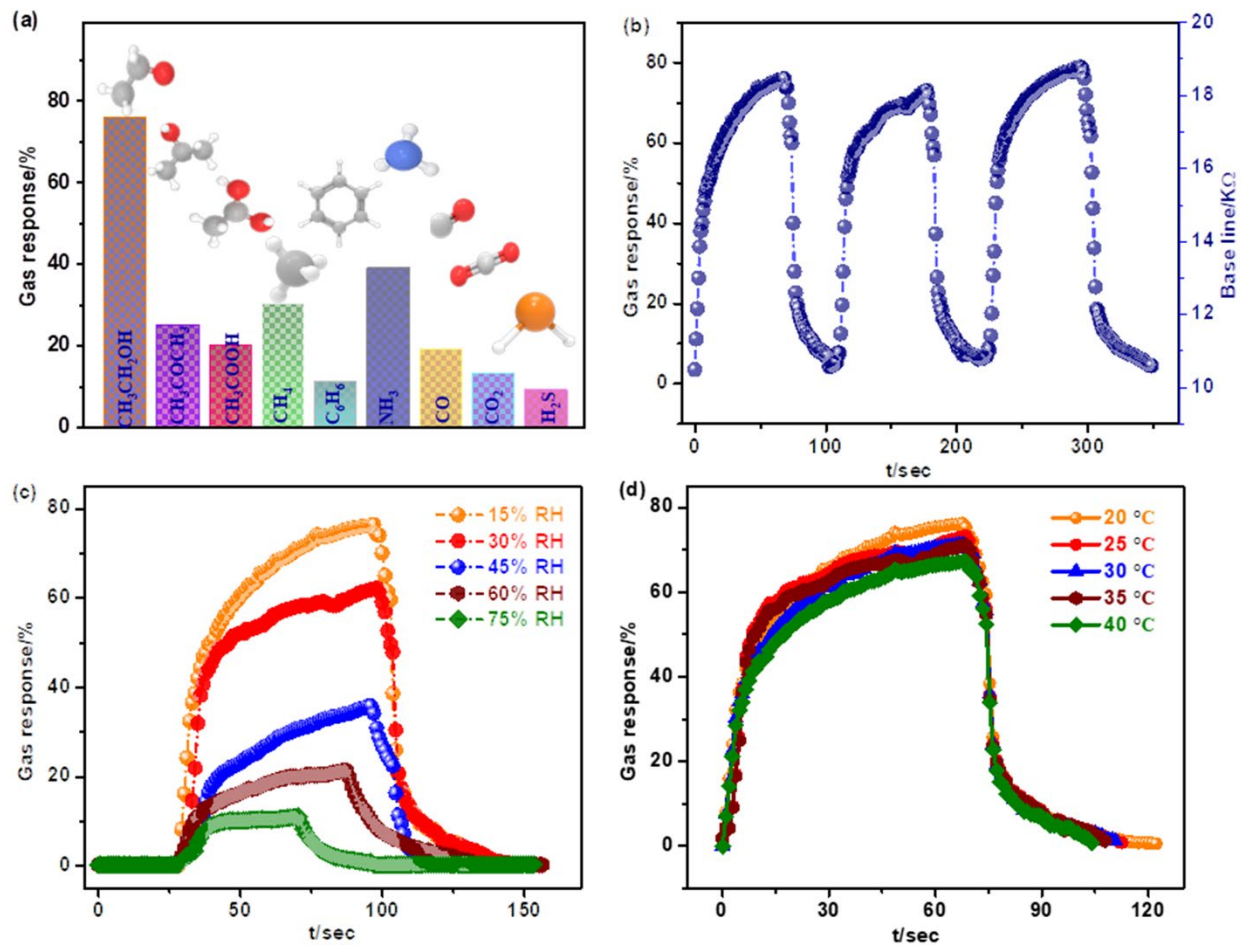
Figure 6-7. (a) The selectivity study of the PP/Ti$_3$C$_2$T$_x$/PPy hybrid sensor to 400 ppm ethanol and other interference gases at room temperature. (b) Reproducibility cycles of resistance baseline and response changes for the PP/Ti$_3$C$_2$T$_x$/PPy hybrid towards 400 ppm ethanol. (c) The humidity effect on the gas response of the PP/Ti$_3$C$_2$T$_x$/PPy sensor under ethanol gas circumstance. (d) The temperature effect on the gas response of the PP/Ti$_3$C$_2$T$_x$/PPy sensor ranges from 20°C to 40°C.

The flexibility of the PP/Ti$_3$C$_2$T$_x$/PPy was evaluated under different bending angles towards 400 ppm ethanol gas at room temperature, and the results are shown in **Figures 6-8a** and 6-**8b**. The response value of the PP/Ti$_3$C$_2$T$_x$/PPy sensor presents negligible change under different bending degrees, which demonstrates the commendable flexibility of the sensor. Besides, long-term stability is a crucial index to evaluate the reliability of the sensor. The response changes of the PP/Ti$_3$C$_2$T$_x$/PPy sensor towards 400 ppm ethanol at room temperature over a period of 13 days are

shown in **Figures 6-8c** and **8d**. The gas response of the PP/Ti$_3$C$_2$T$_x$/PPy sensor remained above 90% of the initial response after 13 days, indicating excellent stability of the composite sensor.
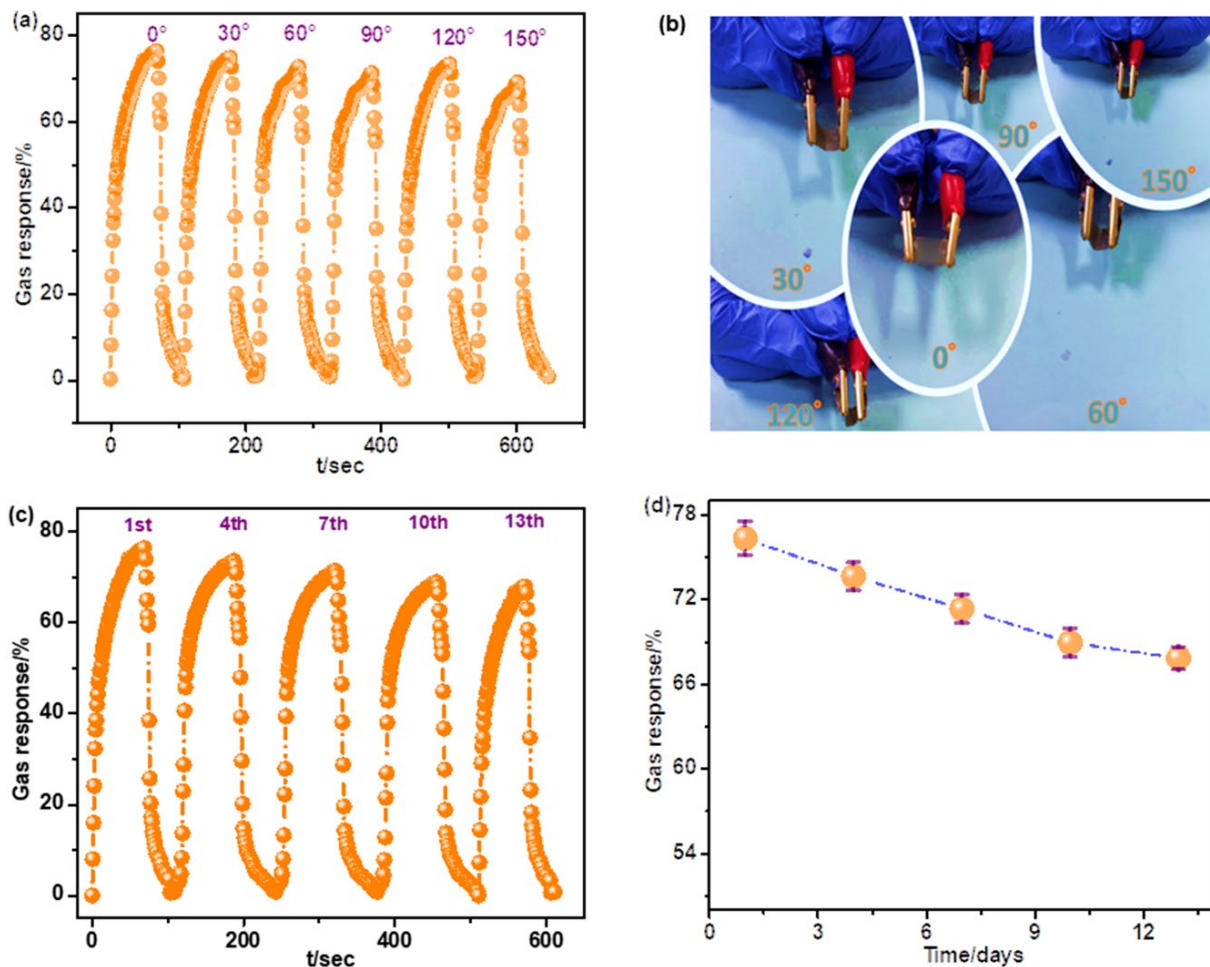
Figure 6-8. (a) The response curves of the PP/Ti$_3$C$_2$T$_x$/PPy sensor at different bending angles. (b) The different bending states of the composite sensor at 0, 30, 60, 90, 120, 150 bending angles. (c) Long-term stability of the PP/Ti$_3$C$_2$T$_x$/PPy sensor towards 400 ppm ethanol. (d) The gas response of the PP/Ti$_3$C$_2$T$_x$/PPy sensor as a function of time.

As summarized in **Table 6-1**, we compared the ethanol sensing characteristics of the sensors based on conducting polymers, Ti$_3$C$_2$T$_x$, or their composites in previous literature with our current work at room temperature (RT). The PP/Ti$_3$C$_2$T$_x$/PPy sensor exhibited a high response value, and short recovery time to ethanol gas, outperforming the sensing performance of most previously reported

sensors. Moreover, Figure S4 presents the investigation of the limit of detection (LOD) of the PP/Ti$_3$C$_2$T$_x$/PPy sensor with previous studies. The result indicates that the theoretical LOD of the PP/Ti$_3$C$_2$T$_x$/PPy sensor (2.21 ppm) is either comparable or lower than the reported values in previous studies.

Table 6-1. Comparison of the sensing characteristics of the sensors based on CPs, Ti$_3$C$_2$T$_x$, or their composites reported in the literature with the PP/Ti$_3$C$_2$T$_x$/PPy sensor obtained in the present work.

Sensing Materials	Substrate	Method	Analyte	Response	t_{Res}	T	Ref
PANI/PVDF	Cu	Spin-coating	Ethanol	31.6%(600 ppm)	50/15 s	RT	73
PPy nanoribbons	Glass	Coating	Ethanol	21.6% (50 ppm)	2/31 s	RT	66
Ti$_3$C$_2$T$_x$	PET	Drop coasting	Ethanol	11.5% (100 ppm) / 70% (100 ppm)	/	RT	74
PPy/ PVA	PVA	Coating	Ethanol		42/200 s	RT	48
Ti$_3$C$_2$T$_x$	SiO$_2$/Si	Vacuum filtration	Ethanol	1.7% (100 ppm) / 204% (100 ppm)	/	RT	56
Ti$_3$C$_2$T$_x$/Ag	PET	Electro-spinning	Ethanol	76.3% (400 ppm)	/	RT	6
Ti$_3$C$_2$T$_x$/PPy	PP	Drop-coating	Ethanol		49/18 s	RT	This work

6.3.3 The sensing mechanism of the PP/Ti$_3$C$_2$T$_x$/PPy sensor.

Ethanol, as an electron donor molecule, can be adsorbed on the active sites of Ti$_3$C$_2$T$_x$ through dispersion forces between the partially charged surface groups and polarized ethanol molecules [55]. During the sensing process, the bonding between ethanol molecules and terminal groups on the Ti$_3$C$_2$T$_x$ could be promoted due to the strong hydrogen bonding, leading to a higher binding energy [55, 56]. This process results in the transfer of electrons from the ethanol molecules to the Ti$_3$C$_2$T$_x$, reducing the concentration of majority charge carriers and causing a decrease in electrical conductivity. In addition, the resistance increase of PPy towards ethanol is mainly attributed to hydrogen bonding and dipole-dipole interaction between PPy and ethanol [66]. More specifically, when PPy is exposed to ethanol, hydrogen bonding occurs between PPy and ethanol molecules, as shown in **Figure 6-9b**. The hydrogen bonding can be understood as the dipole-dipole interaction, causing the swelling and distortion of the PPy molecular chains [66, 75]. As a result, the transfer of charge carriers is negatively affected, leading to a decrease in conductivity.

As illustrated in **Figure 6-9a**, the enhanced sensing performance of the PP/Ti$_3$C$_2$T$_x$/PPy composite sensor can be explained by several synergistic effects between PPy and Ti$_3$C$_2$T$_x$. Firstly, the formation of abundant hydrogen bonds among Ti$_3$C$_2$T$_x$, PPy, and ethanol molecules enhances the binding energy of the composite and enlarges the distortion of the PPy molecular chains, thus promoting the sensing property. Secondly, PPy is a p-type semiconductor, a Schottky junction [71, 76] and a narrowed depletion layer are formed at the interface of Ti$_3$C$_2$T$_x$ and PPy due to the lower work function of Ti$_3$C$_2$T$_x$ compared to PPy, as depicted in **Figure 6-9 (c–e)**. Upon exposure to ethanol, the generation of abundant hydrogen bonding decreases the majority carriers in Ti$_3$C$_2$T$_x$/PPy composite, widening the depletion layer at the interface of the composite and promoting the sensing characteristics. Furthermore, the excellent conductivity of Ti$_3$C$_2$T$_x$

promotes the electron transport process of the PP/Ti$_3$C$_2$T$_x$/PPy composite, and the abundant surface functional groups (such as –OH, –O) on Ti$_3$C$_2$T$_x$ expand the connecting channels for gas diffusion, thereby facilitating the sensing property [74]. Finally, the porous and uniform structure of the PP/Ti$_3$C$_2$T$_x$/PPy composite, with a specific surface area of 84.9 m^2/g, provides a larger number of adsorption sites on the composite surface, improving the adsorption process of ethanol gas molecules and thus promoting the sensing performance [77].
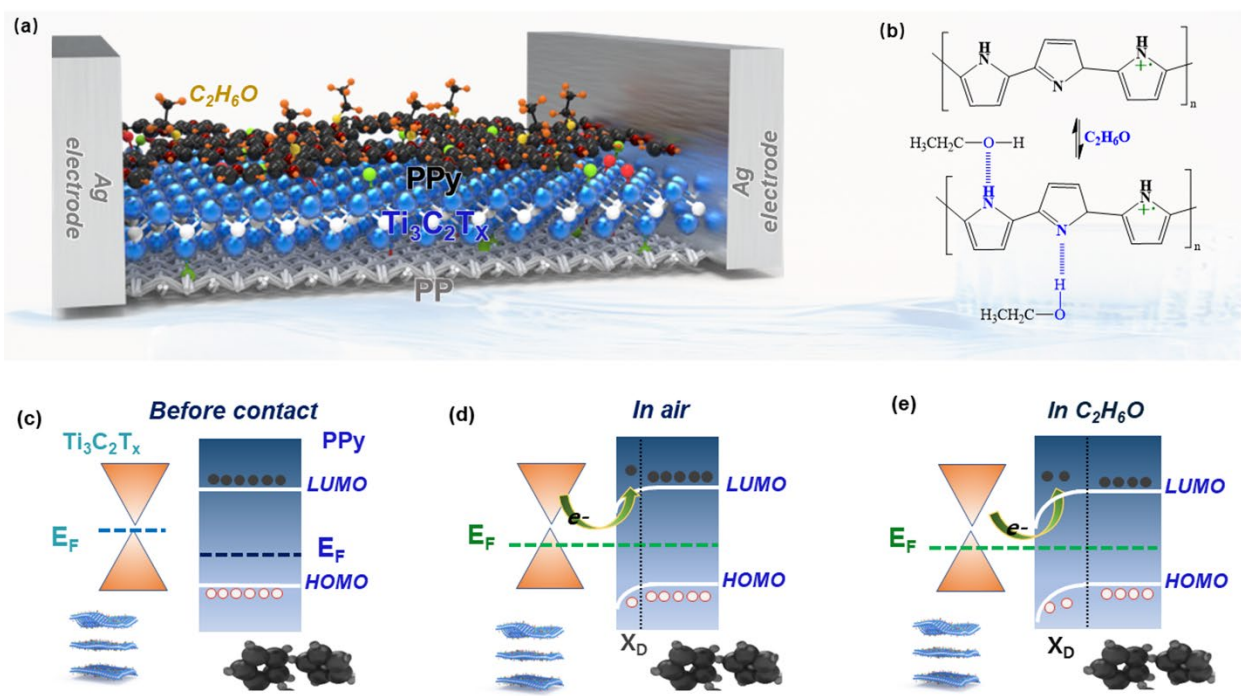
Figure 6-9. (a). The proposed sensing mechanism of the PP/Ti$_3$C$_2$T$_x$/PPy sensor towards ethanol gas. (b) The hydrogen bonding interaction between PPy and ethanol molecules. (c-e). The band structure between PPy and Ti$_3$C$_2$T$_x$: (c) before contact, (d) contact and the formation of Schottky junction in air, and (e) in ethanol, X$_D$ is the width of the hole depletion layer.

6.3.4 Bluetooth sensor module for alcohol exhaled breath monitoring.

In the United States, driving with a blood alcohol concentration (BAC) level above 0.08% is considered a criminal offense. To monitor BAC levels for drunk driving, we developed a wearable Bluetooth sensor module by integrating the PP/Ti$_3$C$_2$T$_x$/PPy composite into a disposable face

mask, as shown in **Figure 6-10(a-d)**. We compared the alcohol sensing performance of our Bluetooth sensor module with a commercial AD-8000 Breathalyzer and plotted the results for BAC levels ranging from 0 to 0.19% in **Figure 6-10(e–k)** and Videos S (1–8). The PP/Ti$_3$C$_2$T$_x$/PPy composite showed sensing responses of -3.3%, 4.7%, 10.6%, 24.7%, 35.4%, 71.4%, and 102.1% to BAC levels of 0%, 0.013%, 0.022%, 0.051%, 0.084%, 0.145%, and 0.190%, respectively. We observed that the BAC detection was mainly dependent on the concentration of alcohol and the moisture in exhaled breath, while temperature and bending states had little influence on the alcohol sensing property. The negative sensing signals in **Figure 6-10e** were mainly due to the high humidity in the exhaled gas, which led to the proton effect on the composite sensor, causing the resistance decrease [78]. Additionally, the higher the BAC concentration, the stronger the response intensity observed by the portable Bluetooth sensor module. Moreover, the concentration of alcohol in exhaled breath decreases continuously with time, resulting in weaker signal intensities towards the end of the curves. Interestingly, we observed an outstanding linear relationship between the BAC detected by the commercial Breathalyzer and the alcohol response tested by our Bluetooth sensor module, as shown in **Figure 6-10l**. Furthermore, we conducted a 5-minute maintenance test of the PP/Ti$_3$C$_2$T$_x$/PPy composite sensor towards 0.084% BAC, which proved the reliable stability of our wireless sensing module, as depicted **in Figure 6-10m**. These results indicate that our as-designed wireless sensing module device can be used for real-time alcohol breath monitoring, demonstrating its potential as a breath analyzer for human drunk driving monitoring.
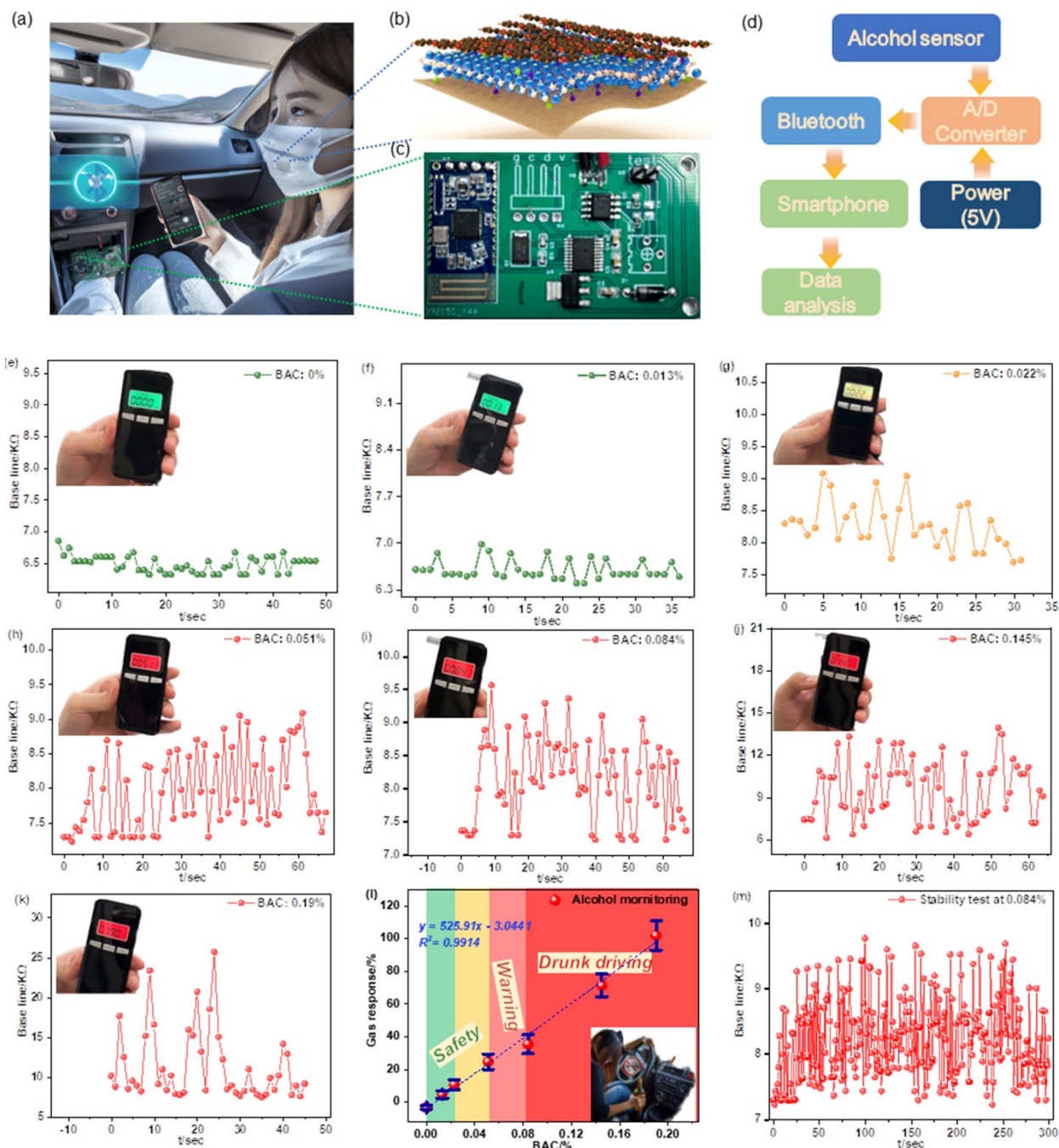
Figure 6-10. (a) Schematic of flexible PP/Ti$_3$C$_2$T$_x$/PPy-based wearable Bluetooth sensor module device for alcohol breath detection. (b) The PP/Ti$_3$C$_2$T$_x$/PPy composite. (c) The wireless Bluetooth sensor module. (d). The PP/Ti$_3$C$_2$T$_x$/PPy hybrid was utilized as an alcohol breath sensor and connected to a readout circuit that was powered by a 5V voltage source. The signals generated by the sensor were then transmitted via Bluetooth to a smartphone. (e-k) The alcohol exhaled breath test under different BAC. (l) The curve that fits the gas response to BAC. (m) The alcohol breath stability test.

6.4 Conclusion

In this study, we developed a wearable $PP/Ti_3C_2T_x/PPy$ composite sensor by combining delaminated $Ti_3C_2T_x$ MXene and PPy on a disposable face mask. The composite sensor depicted a rapid response (49s) and recovery time (18s), excellent repeatability and selectivity, low theoretical limit of detection (2.2 ppm), and a high response value of 76.3% towards 400 ppm ethanol gas, with a sensing response value above 69% even after 13 days. Meanwhile, we observed a negative effect of humidity on the sensing performance due to obstructed ethanol adsorption and decreased gas adsorption sites. Moreover, we elucidated the mechanism for the enhanced sensing property, which was attributed to the abundant functional groups on the composite and the formation of the Schottky junction between $Ti_3C_2T_x$ and PPy. Additionally, we demonstrated a wearable wireless Bluetooth sensing module based on the $PP/Ti_3C_2T_x/PPy$ composite, which could detect different alcohol concentrations in human breath at room temperature. It is believed that the $PP/Ti_3C_2T_x/PPy$ composite sensor has great potential for practical applications in human drunk driving monitoring.

Chapter 7 Conclusions and future work

7.1 Conclusions

Flexible gas sensors have gained prominence in environmental and human health monitoring due to their flexibility and compatibility with electronic substrates. Especially, CPs are exceptional for trace gas detection because of their noteworthy electrical and mechanical properties, biocompatibility, and distinct protonation/deprotonation processes. In this research, our primary aim was to address environmental pollution arising from discarded masks, and to enhance the sensing performance of PANI and PPy-based sensors. We innovatively repurposed disposable masks as flexible substrates, and combining conducting polymers with CNT and 2D materials, resulting in a nanocomposite with excellent sensing capabilities. This was subsequently applied for breath analysis, malodorous gas detection, and monitoring of drunk driving. Furthermore, we studied the sensing mechanisms mainly ascribed to the formation of Schottky junction and the increased surface area, and the humidity effect is the dominate factor on the sensing performance compared with other factors.

In Chapters 3 and 4, we devised a porous PANI-carbon series (either CNT or graphene) nanocomposite gas sensor using discarded surgical masks. By drop-coating an aqueous solution of the carbon series material with surfactant onto the mask's polypropylene fibers and instigating in-situ polymerization of aniline, we achieved our sensor design. This PANI-carbon series sensor showcased rapid response, swift recovery, an impressive low detection threshold (at ppb levels), a substantial response (over 400% for 70 ppm NH_3), and stability at ambient conditions. The standout performance can be credited to the PANI-carbon network's expansive surface area and their efficient conductive pathways. Notably, when embedded in a disposable mask, this sensor

can reliably trace breathing patterns and potentially monitor volatile sulfur compounds in exhaled breath.

Chapters 5 and 6 focused on the MXene/conducting polymer composite sensor, achieved by merging delaminated $Ti_3C_2T_x$ with either PANI or PPy on a mask substrate. The MXene/conducting polymer composite sensor was distinctly responsive to CO_2 and ethanol, exhibited commendable selectivity, demonstrated prolonged stability, and could detect substances at levels as low as about 2 ppm at room conditions. The heightened sensitivity in varied humidity levels and gas concentrations can be linked to the intricate interactions between H-bond sites, target gases, and water molecules. The enhanced sensor capabilities are largely due to the Schottky junction formed between $Ti_3C_2T_x$ and conducting polymers and the increased surface area of the composite. Besides, we showcased a wearable wireless sensing device integrated with Bluetooth, indicative of the potential for real-time monitoring of human exhalation and drunk driving using the MXene/conducting polymer sensor.

In summary, this research advances the field of gas sensing through innovative synthesis techniques, in-depth mechanism theories, and practical applications addressing environmental and health challenges.

7.2 Future work

In our background section, we highlighted the potential of MXene/conducting polymer composites as wearable sensors capable of detecting specific gases. These gases include NH_3, VOCs, VSCs, and phenolic compounds. Such sensors can be pivotal for monitoring food spoilage. Further investigation is needed to understand how different parameters influence the generation of sensing

signals.

Subsequently, there's significant interest in the development of MXene/conducting polymer composites for applications in supercapacitors. Ti_3C_2Tx/PANI composites Energy Storage Exploration**:** Polyaniline (PANI) is widely recognized as an ideal material for energy storage due to its exceptional attributes. These include high theoretical capacitance, impressive chemical stability, straightforward synthesis process, and cost-effectiveness. Nonetheless, pure PANI electrodes come with certain limitations. They exhibit compromised long-term stability and a reduced power density. The reasons for these shortcomings can be attributed to PANI's limited surface area, pronounced volume changes during ion release/doping, and comparatively lower conductivity.

MXenes, on the other hand, boast of a vast array of benefits. They have a tremendous surface-to-volume ratio, adjustable electronic structures, and remarkable flexibility. Additionally, their mechanical robustness is noteworthy. This makes MXenes suitable for a diverse range of applications, spanning from gas sensors and water purification to energy storage.

Considering the unique properties of both PANI and MXenes, it becomes evident why their composite is attracting attention in the energy storage sector. Specifically, for supercapacitor applications, the MXene/PANI composite is appealing due to the metallic conductivity of MXene and PANI's high theoretical capacitance. The synergetic effect between these materials enhances their combined potential.

The detail of research plan is shown below:

1. MXene/PANI Gas Sensor for Food Spoilage:

Given the potential of MXene/conducting polymer composites as wearable sensors for detecting gases such as NH$_3$, ethanol, VSCs, and phenolic compounds, for food deterioration monitoring.

MXenes Selection: MXenes like Ti$_3$C$_2$Tx or V$_2$CTx, the abundant of surface terminor groups, such as -O, -OH may enhance the sensitivity in ambient conditions.

Configuration: Develop a thin-film sensor based on CP/MXene composite by drop-coated Ti$_3$C$_2$T$_x$ MXene suspension and chemical polymerization of PPy on a flexible substrate, the lightweight film sensor can be easily integrated into food packaging.

Hypothesis: Combining MXenes with conducting polymers can enhance sensitivity to ascribed to the abundant functional groups of composite sensor (e.g., amino groups in PPy, terminal groups in Ti$_3$C$_2$T$_x$) and the formation of the Schottky junction, the food spoilage detection allowing early detection before human senses can notice.

2. MXene/Polymer Composites for Supercapacitors:

The union of MXene with conducting polymers like PANI has shown promise for energy storage, particularly in supercapacitors.

MXenes Selection: Focus on Ti$_3$C$_2$T$_x$ for its outstanding electrical conductivity, allowing for enhanced charge storage.

Configuration: Design a sandwich-structured electrode where PANI is infused between layers of MXene, ensuring maximum surface area for charge storage.

Hypothesis: The synergistic effects between PANI's high theoretical capacitance and MXene's

conductivity can overcome the limitations seen in pure PANI electrodes, offering both enhanced storage and discharge rates.

3. Challenges and Roadblocks:

While MXenes exhibit numerous advantages, their susceptibility to oxidation in ambient conditions may reduce the longevity of the composite sensors. Exploring protective coatings or environmental control might be a pivotal area of future investigation.

References

1.   Song, E.; Choi, J.-W., Conducting Polyaniline Nanowire and Its Applications in Chemiresistive Sensing. *Nanomaterials* **2013,** *3* (3), 498-523.

2.   Liu, X.; Zheng, W.; Kumar, R.; Kumar, M.; Zhang, J., Conducting polymer-based nanostructures for gas sensors. *Coordination Chemistry Reviews* **2022,** *462*, 214517.

3.   HEEGER, A. J.; MacDIARMID, A. G., For the discovery and development of conductive polymers. *Chemistry, 1996-2000* **2003**, 369.

4.   Kwon, O. S.; Park, E.; Kweon, O. Y.; Park, S. J.; Jang, J., Novel flexible chemical gas sensor based on poly(3,4-ethylenedioxythiophene) nanotube membrane. *Talanta* **2010,** *82* (4), 1338-1343.

5.   Wu, Z.; Chen, X.; Zhu, S.; Zhou, Z.; Yao, Y.; Quan, W.; Liu, B., Enhanced sensitivity of ammonia sensor using graphene/polyaniline nanocomposite. *Sensors and Actuators B: Chemical* **2013,** *178*, 485-493.

6.   Kar, P.; Choudhury, A., Carboxylic acid functionalized multi-walled carbon nanotube doped polyaniline for chloroform sensors. *Sensors and Actuators B: Chemical* **2013,** *183*, 25-33.

7.   Zhang, D.; Wu, Z.; Zong, X.; Zhang, Y., Fabrication of polypyrrole/Zn2SnO4 nanofilm for ultra-highly sensitive ammonia sensing application. *Sensors and Actuators B: Chemical* **2018,** *274*, 575-586.

8.   Su, P.-G.; Lee, C.-T.; Chou, C.-Y., Flexible NH3 sensors fabricated by in situ self-assembly of polypyrrole. *Talanta* **2009,** *80* (2), 763-769.

9.   Zhang, L.; Du, W.; Nautiyal, A.; Liu, Z.; Zhang, X., Recent progress on nanostructured conducting polymers and composites: synthesis, application and future aspects. *Science China Materials* **2018,** *61* (3), 303-352.

10.   Ma, Z.; Chen, P.; Cheng, W.; Yan, K.; Pan, L.; Shi, Y.; Yu, G., Highly Sensitive, Printable Nanostructured Conductive Polymer Wireless Sensor for Food Spoilage Detection. *Nano Lett* **2018,** *18* (7), 4570-4575.

11.   Wu, T. F.; Gray, E.; Chen, B. Q., A self-healing, adaptive and conductive polymer composite ink for 3D printing of gas sensors. *J Mater Chem C* **2018,** *6* (23), 6200-6207.

12.   Wang, T.; Guo, Y.; Wan, P.; Zhang, H.; Chen, X.; Sun, X., Flexible transparent electronic gas sensors. *Small* **2016,** *12* (28), 3748-3756.

13.   Chang, S.; Yang, M.; Pang, R.; Ye, L.; Wang, X.; Cao, A.; Shang, Y., Intrinsically flexible CNT-TiO2-Interlaced film for NO sensing at room temperature. *Applied Surface Science* **2022,** *579*, 152172.

14.   Quan, L.; Sun, J.; Bai, S.; Luo, R.; Li, D.; Chen, A.; Liu, C. C., A flexible sensor based on polyaniline hybrid using ZnO as template and sensing properties to triethylamine at room temperature. *Applied Surface Science* **2017,** *399*, 583-591.

15.   Arumugam, G. M.; Karunakaran, S. K.; Liu, C.; Zhang, C.; Guo, F.; Wu, S.; Mai, Y., Inorganic hole transport layers in inverted perovskite solar cells: A review. *Nano Select* **2021,** *2* (6), 1081-1116.

16.   Yoon, T.; Jun, J.; Kim, D. Y.; Pourasad, S.; Shin, T. J.; Yu, S. U.; Na, W.; Jang, J.; Kim, K. S., An ultra-sensitive, flexible and transparent gas detection film based on well-ordered flat polypyrrole on single-layered graphene. *Journal of Materials Chemistry A* **2018,** *6* (5), 2257-2263.

17.   Wan, P.; Wen, X.; Sun, C.; Chandran, B. K.; Zhang, H.; Sun, X.; Chen, X., Flexible Transparent Films Based on Nanocomposite Networks of Polyaniline and Carbon Nanotubes for High-Performance Gas Sensing. *Small* **2015,** *11* (40), 5409-15.

18.   Su, Y.; Chen, G.; Chen, C.; Gong, Q.; Xie, G.; Yao, M.; Tai, H.; Jiang, Y.; Chen, J., Self-powered respiration monitoring enabled by a triboelectric nanogenerator. *Advanced Materials* **2021,** *33* (35), 2101262.

19.   Wang, S.; Tai, H.; Liu, B.; Duan, Z.; Yuan, Z.; Pan, H.; Su, Y.; Xie, G.; Du, X.; Jiang, Y., A facile respiration-driven triboelectric nanogenerator for multifunctional respiratory monitoring. *Nano Energy* **2019,** *58*, 312-321.

20.   Zhou, X.; Xue, Z.; Chen, X.; Huang, C.; Bai, W.; Lu, Z.; Wang, T., Nanomaterial-based gas sensors used for breath diagnosis. *Journal of materials chemistry B* **2020,** *8* (16), 3231-3248.

21.   Helwig, A.; Beer, S.; Müller, G., Breathing mode gas detection. *Sensors and Actuators B: Chemical* **2013,** *179*, 131-139.

22.   Janik, P.; Janik, M. A.; Wróbel, Z., Micro-condensation sensor for monitoring respiratory rate and breath strength. *Sensors and Actuators A: Physical* **2012,** *185*, 160-167.

23.   Haick, H.; Broza, Y. Y.; Mochalski, P.; Ruzsanyi, V.; Amann, A., Assessment, origin, and implementation of breath volatile cancer markers. *Chemical Society Reviews* **2014,** *43* (5), 1423-1449.

24.   Güntner, A. T.; Righettoni, M.; Pratsinis, S. E., Selective sensing of NH3 by Si-doped α-MoO3 for breath analysis. *Sensors and Actuators B: Chemical* **2016,** *223*, 266-273.

25.   Shan, B.; Broza, Y. Y.; Li, W.; Wang, Y.; Wu, S.; Liu, Z.; Wang, J.; Gui, S.; Wang, L.; Zhang, Z.; Liu, W.; Zhou, S.; Jin, W.; Zhang, Q.; Hu, D.; Lin, L.; Zhang, Q.; Li, W.; Wang, J.; Liu, H.; Pan, Y.; Haick, H., Multiplexed Nanomaterial-Based Sensor Array for Detection of COVID-19 in Exhaled Breath. *ACS Nano* **2020,** *14* (9), 12125-12132.

26.   Jung, Y.; Moon, H. G.; Lim, C.; Choi, K.; Song, H. S.; Bae, S.; Kim, S. M.; Seo, M.; Lee, T.; Lee, S., Humidity-Tolerant Single-Stranded DNA-Functionalized Graphene Probe for

Medical Applications of Exhaled Breath Analysis. *Advanced Functional Materials* **2017,** *27* (26), 1700068.

27.   Naderi, H.; Hajati, S.; Ghaedi, M.; Dashtian, K.; Sabzehmeidani, M. M., Sensitive, selective and rapid ammonia-sensing by gold nanoparticle-sensitized V2O5/CuWO4 heterojunctions for exhaled breath analysis. *Applied Surface Science* **2020,** *501*, 144270.

28.   Li, S.; Lin, P.; Zhao, L.; Wang, C.; Liu, D.; Liu, F.; Sun, P.; Liang, X.; Liu, F.; Yan, X.; Gao, Y.; Lu, G., The room temperature gas sensor based on Polyaniline@flower-like WO3 nanocomposites and flexible PET substrate for NH3 detection. *Sensors and Actuators B: Chemical* **2018,** *259*, 505-513.

29.   Mao, L.-W.; Zhu, L.-Y.; Tao Wu, T.; Xu, L.; Jin, X.-H.; Lu, H.-L., Excellent long-term stable H2S gas sensor based on Nb2O5/SnO2 core-shell heterostructure nanorods. *Applied Surface Science* **2022,** *602*, 154339.

30.   Pandey, S., Highly sensitive and selective chemiresistor gas/vapor sensors based on polyaniline nanocomposite: A comprehensive review. *Journal of Science: Advanced Materials and Devices* **2016,** *1* (4), 431-453.

31.   Cui, S.; Yang, L.; Wang, J.; Wang, X., Fabrication of a sensitive gas sensor based on PPy/TiO2 nanocomposites films by layer-by-layer self-assembly and its application in food storage. *Sensors and Actuators B: Chemical* **2016,** *233*, 337-346.

32.   Williams, A.; Altman, I.; Burnett, D.; Gutierrez Zorrilla, E.; Garcia, A. R.; Cagle, C.; Luke Croessmann, C.; Pantoya, M., Variations in aluminum particle surface energy and reactivity induced by annealing and quenching. *Applied Surface Science* **2022,** *579*, 152185.

33. Abdulla, S.; Mathew, T. L.; Pullithadathil, B., Highly sensitive, room temperature gas sensor based on polyaniline-multiwalled carbon nanotubes (PANI/MWCNTs) nanocomposite for trace-level ammonia detection. *Sensors and Actuators B: Chemical* **2015,** *221*, 1523-1534.

34. Liu, C.; Hayashi, K.; Toko, K., Au nanoparticles decorated polyaniline nanofiber sensor for detecting volatile sulfur compounds in expired breath. *Sensors and Actuators B: Chemical* **2012,** *161* (1), 504-509.

35. Chaitow, L., Breathing pattern disorders, motor control, and low back pain. *Journal of Osteopathic Medicine* **2004,** *7* (1), 33-40.

36. DuBois, S.; Eng, S.; Bhattacharya, R.; Rulyak, S.; Hubbard, T.; Putnam, D.; Kearney, D. J., Breath Ammonia Testing for Diagnosis of Hepatic Encephalopathy. *Digestive Diseases and Sciences* **2005,** *50* (10), 1780-1784.

37. Yadav, A.; Lokhande, A.; Kim, J.; Lokhande, C., Enhanced sensitivity and selectivity of CO2 gas sensor based on modified La2O3 nanorods. *Journal of Alloys and Compounds* **2017,** *723*, 880-886.

38. Marsal, A.; Cornet, A.; Morante, J., Study of the CO and humidity interference in La doped tin oxide CO2 gas sensor. *Sensors and Actuators B: chemical* **2003,** *94* (3), 324-329.

39. Li, D.-Y.; Liu, L.-X.; Wang, Q.-W.; Zhang, H.-B.; Chen, W.; Yin, G.; Yu, Z.-Z., Functional Polyaniline/MXene/Cotton Fabrics with Acid/Alkali-Responsive and Tunable Electromagnetic Interference Shielding Performances. *ACS Applied Materials & Interfaces* **2022,** *14* (10), 12703-12712.

40. Xu, H.; Zheng, D.; Liu, F.; Li, W.; Lin, J., Synthesis of an MXene/polyaniline composite with excellent electrochemical properties. *Journal of Materials Chemistry A* **2020,** *8* (12), 5853-5858.

41.   Zhao, L.; Wang, K.; Wei, W.; Wang, L.; Han, W., High-performance flexible sensing devices based on polyaniline/MXene nanocomposites. *InfoMat* **2019,** *1* (3), 407-416.

42.   Pei, Y.; Zhang, X.; Hui, Z.; Zhou, J.; Huang, X.; Sun, G.; Huang, W., Ti3C2TX MXene for sensing applications: recent progress, design principles, and future perspectives. *ACS nano* **2021,** *15* (3), 3996-4017.

43.   Saberian, M.; Li, J.; Kilmartin-Lynch, S.; Boroujeni, M., Repurposing of COVID-19 single-use face masks for pavements base/subbase. *Science of The Total Environment* **2021,** *769*, 145527.

44.   Yu, R.; Wen, X.; Liu, J.; Wang, Y.; Chen, X.; Wenelska, K.; Mijowska, E.; Tang, T., A green and high-yield route to recycle waste masks into CNTs/Ni hybrids via catalytic carbonization and their application for superior microwave absorption. *Applied Catalysis B: Environmental* **2021,** *298*, 120544.

45.   Zhong, H.; Zhu, Z.; Lin, J.; Cheung, C. F.; Lu, V. L.; Yan, F.; Chan, C.-Y.; Li, G., Reusable and Recyclable Graphene Masks with Outstanding Superhydrophobic and Photothermal Performances. *ACS Nano* **2020,** *14* (5), 6213-6221.

46.   Li, Q.; Yin, Y.; Cao, D.; Wang, Y.; Luan, P.; Sun, X.; Liang, W.; Zhu, H., Photocatalytic Rejuvenation Enabled Self-Sanitizing, Reusable, and Biodegradable Masks against COVID-19. *ACS Nano* **2021,** *15* (7), 11992-12005.

47.   Kim, K. H.; Jahan, S. A.; Kabir, E., A review of breath analysis for diagnosis of human health. *TrAC Trends in Analytical Chemistry* **2012,** *33*, 1-8.

48.   Liu, H.; Allen, J.; Zheng, D.; Chen, F., Recent development of respiratory rate measurement technologies. *Physiological Measurement* **2019,** *40* (7), 07TR01.

49.   Liu, Y.; Shukla, D.; Newman, H.; Zhu, Y., Soft wearable sensors for monitoring symptoms of COVID-19: A review. *Progress in Biomedical Engineering* **2021**.

50.   Choi, W.; Kim, J.; Lee, E.; Mehta, G.; Prasad, V., Asymmetric 2D MoS2 for Scalable and High-Performance Piezoelectric Sensors. *ACS Applied Materials & Interfaces* **2021,** *13* (11), 13596-13603.

51.   Wang, X.; Gong, L.; Zhang, D.; Fan, X.; Jin, Y.; Guo, L., Room temperature ammonia gas sensor based on polyaniline/copper ferrite binary nanocomposites. *Sensors and Actuators B: Chemical* **2020,** *322*, 128615.

52.   Javadian-Saraf, A.; Hosseini, E.; Wiltshire, B. D.; Zarifi, M. H.; Arjmand, M., Graphene oxide/polyaniline-based microwave split-ring resonator: A versatile platform towards ammonia sensing. *Journal of Hazardous Materials* **2021,** *418*, 126283.

53.   Li, H.-Y.; Lee, C.-S.; Kim, D. H.; Lee, J.-H., Flexible Room-Temperature NH3 Sensor for Ultrasensitive, Selective, and Humidity-Independent Gas Detection. *ACS Applied Materials & Interfaces* **2018,** *10* (33), 27858-27867.

54.   Righettoni, M.; Amann, A.; Pratsinis, S. E., Breath analysis by nanostructured metal oxides as chemo-resistive gas sensors. *Materials Today* **2015,** *18* (3), 163-171.

55.   Si, B.; Song, E., Recent Advances in the Detection of Neurotransmitters. *Chemosensors* **2018,** *6* (1), 1.

56.   Kim, J.; Lee, E.; Mehta, G.; Choi, W., Stable and high-performance piezoelectric sensor via CVD grown WS$_2$. *Nanotechnology* **2020,** *31* (44), 445203.

57.   Tan, H.; Chu, Y.; Wu, X.; Liu, W.-J.; Zhang, D. W.; Ding, S.-J., High-Performance Flexible Gas Sensors Based on Layer-by-Layer Assembled Polythiophene Thin Films. *Chemistry of Materials* **2021,** *33* (19), 7785-7794.

58.   Khan, N. I.; Maddaus, A. G.; Song, E., A Low-Cost Inkjet-Printed Aptamer-Based Electrochemical Biosensor for the Selective Detection of Lysozyme. *Biosensors* **2018,** *8* (1), 7.

59.   Liu, C.-X.; Choi, J.-W., Improved Dispersion of Carbon Nanotubes in Polymers at High Concentrations. *Nanomaterials* **2012,** *2* (4), 329-347.

60.   Jiang, Y.; Tang, N.; Zhou, C.; Han, Z. Y.; Qu, H.; Duan, X. X., A chemiresistive sensor array from conductive polymer nanowires fabricated by nanoscale soft lithography. *Nanoscale* **2018,** *10* (44), 20578-20586.

61.   Fan, G.; Chen, D.; Li, T.; Yi, S.; Ji, H.; Wang, Y.; Zhang, Z.; Shao, G.; Fan, B.; Wang, H.; Xu, H.; Lu, H.; Zhou, Y.; Zhang, R.; Sun, J., Enhanced room-temperature ammonia-sensing properties of polyaniline-modified WO3 nanoplates derived via ultrasonic spray process. *Sensors and Actuators B: Chemical* **2020,** *312*, 127892.

62.   Eising, M.; Cava, C. E.; Salvatierra, R. V.; Zarbin, A. J. G.; Roman, L. S., Doping effect on self-assembled films of polyaniline and carbon nanotube applied as ammonia gas sensor. *Sensors and Actuators B: Chemical* **2017,** *245*, 25-33.

63.   Zhang, D. Z.; Wu, Z. L.; Zong, X. Q., Flexible and highly sensitive H2S gas sensor based on in-situ polymerized SnO2/rGO/PANI ternary nanocomposite with application in halitosis diagnosis. *Sensor Actuat B-Chem* **2019,** *289*, 32-41.

64.   Zhang, W. Y.; Cao, S.; Wu, Z. F.; Zhang, M.; Cao, Y. L.; Guo, J. X.; Zhong, F. R.; Duan, H. M.; Jia, D. Z., High-Performance Gas Sensor of Polyaniline/Carbon Nanotube Composites Promoted by Interface Engineering. *Sensors-Basel* **2020,** *20* (1).

65.   Bandgar, D. K.; Navale, S. T.; Nalage, S. R.; Mane, R. S.; Stadler, F. J.; Aswal, D. K.; Gupta, S. K.; Patil, V. B., Simple and low-temperature polyaniline-based flexible ammonia sensor:

a step towards laboratory synthesis to economical device design. *J Mater Chem C* **2015,** *3* (36), 9461-9468.

66.　　Talwar, V.; Singh, O.; Singh, R. C., ZnO assisted polyaniline nanofibers and its application as ammonia gas sensor. *Sensors and Actuators B: Chemical* **2014,** *191*, 276-282.

67.　　Yang, M.; Zhang, X.; Guo, C.; Cheng, X.; Zhu, C.; Xu, Y.; Major, Z.; Huo, L., Resistive room temperature DMA gas sensor based on the forest-like unusual n-type PANI/TiO2 nanocomposites. *Sensors and Actuators B: Chemical* **2021,** *342*, 130067.

68.　　Liu, A.; Lv, S.; Jiang, L.; Liu, F.; Zhao, L.; Wang, J.; Hu, X.; Yang, Z.; He, J.; Wang, C.; Yan, X.; Sun, P.; Shimanoe, K.; Lu, G., The gas sensor utilizing polyaniline/ MoS2 nanosheets/ SnO2 nanotubes for the room temperature detection of ammonia. *Sensors and Actuators B: Chemical* **2021,** *332*, 129444.

69.　　Zhang, Y.; Zhang, J.; Jiang, Y.; Duan, Z.; Liu, B.; Zhao, Q.; Wang, S.; Yuan, Z.; Tai, H., Ultrasensitive flexible NH3 gas sensor based on polyaniline/SrGe4O9 nanocomposite with ppt-level detection ability at room temperature. *Sensors and Actuators B: Chemical* **2020,** *319*.

70.　　Albaris, H.; Karuppasamy, G., Fabrication of room temperature liquid petroleum gas sensor based on PAni–CNT–V2O5 hybrid nanocomposite. *Applied Nanoscience* **2019,** *9* (8), 1719-1729.

71.　　Ding, M.; Tang, Y.; Gou, P.; Reber, M. J.; Star, A., Chemical sensing with polyaniline coated single-walled carbon nanotubes. *Advanced Materials* **2011,** *23* (4), 536-540.

72.　　Liu, C. H.; Tai, H. L.; Zhang, P.; Yuan, Z.; Du, X. S.; Xie, G. Z.; Jiang, Y. D., A high-performance flexible gas sensor based on self-assembled PANI-CeO2 nanocomposite thin film for trace-level NH3 detection at room temperature. *Sensor Actuat B-Chem* **2018,** *261*, 587-597.

73.   Shin, Y.-H.; Teresa Gutierrez-Wing, M.; Choi, J.-W., Review—Recent Progress in Portable Fluorescence Sensors. *Journal of The Electrochemical Society* **2021,** *168* (1), 017502.

74.   Lee, S. H.; Eom, W.; Shin, H.; Ambade, R. B.; Bang, J. H.; Kim, H. W.; Han, T. H., Room-Temperature, Highly Durable Ti(3)C(2)T(x) MXene/Graphene Hybrid Fibers for NH(3) Gas Sensing. *ACS Appl Mater Interfaces* **2020,** *12* (9), 10434-10442.

75.   Lee, E.; VahidMohammadi, A.; Yoon, Y. S.; Beidaghi, M.; Kim, D.-J., Two-Dimensional Vanadium Carbide MXene for Gas Sensors with Ultrahigh Sensitivity Toward Nonpolar Gases. *ACS Sensors* **2019,** *4* (6), 1603-1611.

76.   Chatterjee, S.; Castro, M.; Feller, J. F., Tailoring selectivity of sprayed carbon nanotube sensors (CNT) towards volatile organic compounds (VOC) with surfactants. *Sensors and Actuators B: Chemical* **2015,** *220*, 840-849.

77.   Müller, C.; Al-Hamry, A.; Kanoun, O.; Rahaman, M.; Zahn, D. R. T.; Matsubara, E. Y.; Rosolen, J. M., Humidity Sensing Behavior of Endohedral Li-Doped and Undoped SWCNT/SDBS Composite Films. *Sensors-Basel* **2019,** *19* (1), 171.

78.   Wu, T.; Lv, D.; Shen, W.; Song, W.; Tan, R., Trace-level ammonia detection at room temperature based on porous flexible polyaniline/polyvinylidene fluoride sensing film with carbon nanotube additives. *Sensors and Actuators B: Chemical* **2020,** *316*, 128198.

79.   Krylova, V.; Dukštienė, N., Synthesis and Characterization of Ag$_2$S Layers Formed on Polypropylene. *Journal of Chemistry* **2013,** *2013*, 987879.

80.   Gopanna, A.; Mandapati, R. N.; Thomas, S. P.; Rajan, K.; Chavali, M., Fourier transform infrared spectroscopy (FTIR), Raman spectroscopy and wide-angle X-ray scattering (WAXS) of polypropylene (PP)/cyclic olefin copolymer (COC) blends for qualitative and quantitative analysis. *Polymer Bulletin* **2019,** *76* (8), 4259-4274.

81.   Bai, S.; Sun, C.; Wan, P.; Wang, C.; Luo, R.; Li, Y.; Liu, J.; Sun, X., Transparent conducting films of hierarchically nanostructured polyaniline networks on flexible substrates for high-performance gas sensors. *Small* **2015,** *11* (3), 306-10.

82.   Souto, L. F. C.; Soares, B. G., Polyaniline/carbon nanotube hybrids modified with ionic liquids as anticorrosive additive in epoxy coatings. *Progress in Organic Coatings* **2020,** *143*, 105598.

83.   Chen, R. J.; Zhang, Y.; Wang, D.; Dai, H., Noncovalent Sidewall Functionalization of Single-Walled Carbon Nanotubes for Protein Immobilization. *Journal of the American Chemical Society* **2001,** *123* (16), 3838-3839.

84.   Tanguy, N. R.; Thompson, M.; Yan, N., A review on advances in application of polyaniline for ammonia detection. *Sensors and Actuators B: Chemical* **2018,** *257*, 1044-1064.

85.   Hashemi Karouei, S. F.; Milani Moghaddam, H.; Saadat Niavol, S., Characterization and gas sensing properties of graphene/polyaniline nanocomposite with long-term stability under high humidity. *Journal of Materials Science* **2021,** *56* (6), 4239-4253.

86.   Li, S.; Diao, Y.; Yang, Z.; He, J.; Wang, J.; Liu, C.; Liu, F.; Lu, H.; Yan, X.; Sun, P.; Lu, G., Enhanced room temperature gas sensor based on Au-loaded mesoporous In2O3 nanospheres@polyaniline core-shell nanohybrid assembled on flexible PET substrate for NH3 detection. *Sensors and Actuators B: Chemical* **2018,** *276*, 526-533.

87.   Ma, J.; Fan, H.; Li, Z.; Jia, Y.; Yadav, A. K.; Dong, G.; Wang, W.; Dong, W.; Wang, S., Multi-walled carbon nanotubes/polyaniline on the ethylenediamine modified polyethylene terephthalate fibers for a flexible room temperature ammonia gas sensor with high responses. *Sensors and Actuators B: Chemical* **2021,** *334*, 129677.

88. Wu, Q.; Shen, W.; Lv, D.; Chen, W.; Song, W.; Tan, R., An enhanced flexible room temperature ammonia gas sensor based on GP-PANI/PVDF multi-hierarchical nanocomposite film. *Sensors and Actuators B: Chemical* **2021,** *334*, 129630.

89. Choi, S.-J.; Jang, B.-H.; Lee, S.-J.; Min, B. K.; Rothschild, A.; Kim, I.-D., Selective Detection of Acetone and Hydrogen Sulfide for the Diagnosis of Diabetes and Halitosis Using SnO2 Nanofibers Functionalized with Reduced Graphene Oxide Nanosheets. *ACS Applied Materials & Interfaces* **2014,** *6* (4), 2588-2597.

90. Hou, Y.; Lv, C.; Liu, W.; Guo, Y.; Jin, Y.; Li, B.; Zhang, Y.; Liu, Y., In situ synthesis of copper metal-organic framework on paper-based device for dual-mode detection of volatile sulfur compounds in exhaled breath. *Sensors and Actuators B: Chemical* **2022,** *352*, 131008.

91. Li, L.; Zhang, S.; Lu, Y.; Zhang, J.; Zhang, X.; Wang, R.; Huang, J., Highly Selective and Sensitive Detection of Volatile Sulfur Compounds by Ionically Conductive Metal-Organic Frameworks. *Advanced Materials* **2021,** *33* (52), 2104120.

92. Amano, A.; Yoshida, Y.; Oho, T.; Koga, T., Monitoring ammonia to assess halitosis. *Oral Surgery, Oral Medicine, Oral Pathology, Oral Radiology, and Endodontology* **2002,** *94* (6), 692-696.

93. Jung, H.; Min, H.; Hwang, J.; Kim, J.; Choe, Y.-S.; Lee, H.-S.; Lee, W., Selective detection of sub-1-ppb level isoprene using Pd-coated In2O3 thin film integrated in portable gas chromatography. *Applied Surface Science* **2022,** *586*, 152827.

94. Atanasova, G.; Dikovska, A. O.; Dilova, T.; Georgieva, B.; Avdeev, G. V.; Stefanov, P.; Nedyalkov, N. N., Metal-oxide nanostructures produced by PLD in open air for gas sensor applications. *Applied Surface Science* **2019,** *470*, 861-869.

95.   Nakate, U. T.; Patil, P.; Nakate, Y. T.; Na, S.-I.; Yu, Y. T.; Hahn, Y.-B., Ultrathin ternary metal oxide Bi2MoO6 nanosheets for high performance asymmetric supercapacitor and gas sensor applications. *Applied Surface Science* **2021,** *551*, 149422.

96.   Naganaboina, V. R.; Singh, S. G., Graphene-CeO2 based flexible gas sensor: Monitoring of low ppm CO gas with high selectivity at room temperature. *Applied Surface Science* **2021,** *563*, 150272.

97.   Jeon, I. S.; Bae, G.; Jang, M.; Yoon, Y.; Jang, S.; Song, W.; Myung, S.; Lim, J.; Lee, S. S.; Jung, H.-K.; Hwang, J.; An, K.-S., Atomic-level mediation in structural interparameter tradeoff of zinc oxide nanowires-based gas sensors: ZnO nanofilm/ZnO nanowire homojunction array. *Applied Surface Science* **2021,** *540*, 148350.

98.   Shin, D. H.; Choi, Y. S.; Park, S. Y.; Yeo, C.-S.; Park, Y. Y.; Song, J. Y.; Lee, S.-K.; Kim, T.-W.; Bae, S.; Hong, B. H., Fast and complete recovery of TMDs-decorated rGO fiber gas sensors at room temperature. *Applied Surface Science* **2022,** *578*, 151832.

99.   Gao, L.; Han, Y.; Surjadi, J. U.; Cao, K.; Zhou, W.; Xu, H.; Hu, X.; Wang, M.; Fan, K.; Wang, Y.; Wang, W.; Espinosa, H. D., Magnetically induced micropillar arrays for an ultrasensitive flexible sensor with a wireless recharging system. *SCIENCE CHINA Materials* **2021,** *64* (2095-8226), 1977.

100.   Nasirian, S., Enhanced carbon dioxide sensing performance of polyaniline/tin dioxide nanocomposite by ultraviolet light illumination. *Applied Surface Science* **2020,** *502*, 144302.

101.   Milani Moghaddam, H.; Nasirian, S., Hydrogen gas sensing feature of polyaniline/titania (rutile) nanocomposite at environmental conditions. *Applied Surface Science* **2014,** *317*, 117-124.

102.   He, H.; Zhang, M.; Zhao, T.; Zeng, H.; Xing, L.; Xue, X., A self-powered gas sensor based on PDMS/Ppy triboelectric-gas-sensing arrays for the real-time monitoring of automotive exhaust gas at room temperature. *SCIENCE CHINA Materials* **2019,** *62* (2095-8226), 1433.

103.   Nasirian, S.; Milani Moghaddam, H., Polyaniline assisted by TiO2:SnO2 nanoparticles as a hydrogen gas sensor at environmental conditions. *Applied Surface Science* **2015,** *328*, 395-404.

104.   Li, S.; Liu, A.; Yang, Z.; He, J.; Wang, J.; Liu, F.; Lu, H.; Yan, X.; Sun, P.; Liang, X.;   Gao, Y.; Lu, G., Room temperature gas sensor based on tin dioxide@ polyaniline nanocomposite assembled on flexible substrate: ppb-level detection of NH3. *Sensors and Actuators B: Chemical* **2019,** *299*, 126970.

105.   Hsini, A.; Naciri, Y.; Laabd, M.; Bouziani, A.; Navío, J. A.; Puga, F.; Boukherroub, R.;   Lakhmiri, R.; Albourine, A., Development of a novel PANI@WO3 hybrid composite and its application as a promising adsorbent for Cr(VI) ions removal. *Journal of Environmental Chemical Engineering* **2021,** *9* (5), 105885.

106.   Ma, Y.; Zhou, Y.; Sun, Y.; Chen, H.; Xiong, Z.; Li, X.; Shen, L.; Liu, Y., Tunable magnetic properties of Fe3O4/rGO/PANI nanocomposites for enhancing microwave absorption performance. *Journal of Alloys and Compounds* **2019,** *796*, 120-130.

107.   Xue, L.; Wang, W.; Guo, Y.; Liu, G.; Wan, P., Flexible polyaniline/carbon nanotube nanocomposite film-based electronic gas sensors. *Sensors and Actuators B: Chemical* **2017,** *244*, 47-53.

108.   Guo, Y.; Wang, T.; Chen, F.; Sun, X.; Li, X.; Yu, Z.; Wan, P.; Chen, X., Hierarchical graphene–polyaniline nanocomposite films for high-performance flexible electronic gas sensors. *Nanoscale* **2016,** *8* (23), 12073-12080.

109.   Hu, X.; Lin, Z., Transforming waste polypropylene face masks into S-doped porous carbon as the cathode electrode for supercapacitors. *Ionics* **2021,** *27* (5), 2169-2179.

110.   Lee, E.; Yoon, Y. S.; Kim, D.-J., Two-Dimensional Transition Metal Dichalcogenides and Metal Oxide Hybrids for Gas Sensing. *ACS Sensors* **2018,** *3* (10), 2045-2060.

111.   Chang, J.; Zhang, X.; Wang, Z.; Li, C.; Hu, Q.; Gao, J.; Feng, L., Polyaniline-Reduced Graphene Oxide Nanosheets for Room Temperature NH3 Detection. *ACS Applied Nano Materials* **2021,** *4* (5), 5263-5272.

112.   Kumar, L.; Rawal, I.; Kaur, A.; Annapoorni, S., Flexible room temperature ammonia sensor based on polyaniline. *Sensors and Actuators B: Chemical* **2017,** *240*, 408-416.

113.   Qi, J.; Xu, X.; Liu, X.; Lau, K. T., Fabrication of textile based conductometric polyaniline gas sensor. *Sensors and Actuators B: Chemical* **2014,** *202*, 732-740.

114.   Li, S.; Wang, T.; Yang, Z.; He, J.; Wang, J.; Zhao, L.; Lu, H.; Tian, T.; Liu, F.; Sun, P.; Yan, X.; Lu, G., Room temperature high performance NH3 sensor based on GO-rambutan-like polyaniline hollow nanosphere hybrid assembled to flexible PET substrate. *Sensors and Actuators B: Chemical* **2018,** *273*, 726-734.

115.   Maity, D.; Kumar, R. T. R., Polyaniline Anchored MWCNTs on Fabric for High Performance Wearable Ammonia Sensor. *ACS Sensors* **2018,** *3* (9), 1822-1830.

116.   Chen, W.; Yang, P.; Shen, W.; Zhu, C.; Lv, D.; Tan, R.; Song, W., Flexible room temperature ammonia gas sensor based on in suit polymerized PANI/PVDF porous composite film. *Journal of Materials Science: Materials in Electronics* **2020,** *31* (14), 11870-11877.

117.   Ates, H. C.; Dincer, C., Wearable breath analysis. *Nature Reviews Bioengineering* **2023,** *1* (2), 80-82.

118.   Zhong, J.; Li, Z.; Takakuwa, M.; Inoue, D.; Hashizume, D.; Jiang, Z.; Shi, Y.; Ou, L.; Nayeem, M. O. G.; Umezu, S., Smart face mask based on an ultrathin pressure sensor for wireless monitoring of breath conditions. *Advanced Materials* **2022,** *34* (6), 2107758.

119.   Cheng, Y.; Wang, C.; Zhong, J.; Lin, S.; Xiao, Y.; Zhong, Q.; Jiang, H.; Wu, N.; Li, W.; Chen, S.; Wang, B.; Zhang, Y.; Zhou, J., Electrospun polyetherimide electret nonwoven for bi-functional smart face mask. *Nano Energy* **2017,** *34*, 562-569.

120.   Ates, H. C.; Brunauer, A.; von Stetten, F.; Urban, G. A.; Güder, F.; Merkoçi, A.; Früh, S. M.; Dincer, C., Integrated Devices for Non-Invasive Diagnostics. *Advanced Functional Materials* **2021,** *31* (15), 2010388.

121.   Leding, C.; Skov, J.; Uhrbrand, K.; Lisby, J. G.; Hansen, K. P.; Benfield, T.; Duncan, L. K., Detection of SARS-CoV-2 in exhaled breath from non-hospitalized COVID-19-infected individuals. *Scientific Reports* **2022,** *12* (1), 11151.

122.   Righettoni, M.; Tricoli, A.; Pratsinis, S. E., Si: WO3 sensors for highly selective detection of acetone for easy diagnosis of diabetes by breath analysis. *Analytical chemistry* **2010,** *82* (9), 3581-3587.

123.   Shin, J.; Choi, S. J.; Lee, I.; Youn, D. Y.; Park, C. O.; Lee, J. H.; Tuller, H. L.; Kim, I. D., Thin-wall assembled SnO2 fibers functionalized by catalytic Pt nanoparticles and their superior exhaled-breath-sensing properties for the diagnosis of diabetes. *Advanced Functional Materials* **2013,** *23* (19), 2357-2367.

124.   Zhang, N.; Tao, C.; Fan, X.; Chen, J., Progress in triboelectric nanogenerators as self-powered smart sensors. *Journal of Materials Research* **2017,** *32* (9), 1628-1646.

125.   Hromadka, J.; Tokay, B.; Correia, R.; Morgan, S. P.; Korposh, S., Carbon dioxide measurements using long period grating optical fibre sensor coated with metal organic framework HKUST-1. *Sensors and Actuators B: Chemical* **2018,** *255*, 2483-2494.

126.   EH40, H., Workplace exposure limits. *London: Health and Safety Executive* **2011**.

127.   Escobedo, P.; Fernández-Ramos, M. D.; López-Ruiz, N.; Moyano-Rodríguez, O.; Martínez-Olmos, A.; Pérez de Vargas-Sansalvador, I. M.; Carvajal, M. A.; Capitán-Vallvey, L. F.; Palma, A. J., Smart facemask for wireless CO2 monitoring. *Nature Communications* **2022,** *13* (1), 72.

128.   Naganaboina, V. R.; Anandkumar, M.; Deshpande, A. S.; Singh, S. G., Single-Phase High-Entropy Oxide Nanoparticles for Wide Dynamic Range Detection of CO2. *ACS Applied Nano Materials* **2022,** *5* (3), 4524-4536.

129.   Peng, Z.; Jimenez, J. L., Exhaled CO2 as a COVID-19 infection risk proxy for different indoor environments and activities. *Environmental Science & Technology Letters* **2021,** *8* (5), 392-397.

130.   Stassen, I.; Dou, J.-H.; Hendon, C.; Dincă, M., Chemiresistive sensing of ambient CO2 by an autogenously hydrated Cu3 (hexaiminobenzene) 2 framework. *ACS central Science* **2019,** *5* (8), 1425-1431.

131.   Artanto, Y.; Jansen, J.; Pearson, P.; Do, T.; Cottrell, A.; Meuleman, E.; Feron, P., Performance of MEA and amine-blends in the CSIRO PCC pilot plant at Loy Yang Power in Australia. *Fuel* **2012,** *101*, 264-275.

132.   Wang, C.; Ding, Y.; Li, M.; Li, H.; Xu, S.; Li, C.; Qian, L.; Yang, B., Surface acoustic wave sensor based on Au/TiO2/PEDOT with dual response to carbon dioxide and humidity. *Analytica Chimica Acta* **2022,** *1190*, 339264.

133.   Frodl, R.; Tille, T., An automotive Bi-Source spectroscopic carbon dioxide sensor with pressure compensation. *Sensors and Actuators B: Chemical* **2007,** *127* (1), 82-88.

134.   Xiong, Y.; Xue, Q.; Ling, C.; Lu, W.; Ding, D.; Zhu, L.; Li, X., Effective CO_2 detection based on LaOCl-doped SnO_2 nanofibers: Insight into the role of oxygen in carrier gas. *Sensors and Actuators B: Chemical* **2017,** *241*, 725-734.

135.   Tanvir, N. B.; Yurchenko, O.; Laubender, E.; Urban, G., Investigation of low temperature effects on work function based CO_2 gas sensing of nanoparticulate CuO films. *Sensors and Actuators B: Chemical* **2017,** *247*, 968-974.

136.   Lee, M.-S.; Meyer, J.-U., A new process for fabricating CO_2-sensing layers based on $BaTiO_3$ and additives. *Sensors and Actuators B: Chemical* **2000,** *68* (1), 293-299.

137.   Kanaparthi, S.; Singh, S. G., Chemiresistive Sensor Based on Zinc Oxide Nanoflakes for CO_2 Detection. *ACS Applied Nano Materials* **2019,** *2* (2), 700-706.

138.   Joshi, S.; Ippolito, S. J.; Periasamy, S.; Sabri, Y. M.; Sunkara, M. V., Efficient Heterostructures of Ag@CuO/$BaTiO_3$ for Low-Temperature CO_2 Gas Detection: Assessing the Role of Nanointerfaces during Sensing by Operando DRIFTS Technique. *ACS Applied Materials & Interfaces* **2017,** *9* (32), 27014-27026.

139.   Bai, S.; Sun, C.; Wan, P.; Wang, C.; Luo, R.; Li, Y.; Liu, J.; Sun, X., Transparent Conducting Films of Hierarchically Nanostructured Polyaniline Networks on Flexible Substrates for High-Performance Gas Sensors. *Small* **2015,** *11* (3), 306-310.

140.   Wu, G.; Du, H.; Cha, Y. L.; Lee, D.; Kim, W.; Feyzbar-Khalkhali-Nejad, F.; Oh, T.-S.; Zhang, X.; Kim, D.-J., A wearable mask sensor based on polyaniline/CNT nanocomposites for monitoring ammonia gas and human breathing. *Sensors and Actuators B: Chemical* **2023,** *375*, 132858.

141. Barde, R., Preparation, characterization and CO2 gas sensitivity of polyaniline doped with sodium superoxide (NaO2). *Materials Research Bulletin* **2016,** *73*, 70-76.

142. Sonker, R. K.; Sabhajeet, S.; Yadav, B., TiO 2–PANI nanocomposite thin film prepared by spin coating technique working as room temperature CO 2 gas sensing. *Journal of Materials Science: Materials in Electronics* **2016,** *27*, 11726-11732.

143. Wu, J.; Feng, S.; Wei, X.; Shen, J.; Lu, W.; Shi, H.; Tao, K.; Lu, S.; Sun, T.; Yu, L., Facile synthesis of 3D graphene flowers for ultrasensitive and highly reversible gas sensing. *Advanced Functional Materials* **2016,** *26* (41), 7462-7469.

144. Wu, G.; Du, H.; Lee, D.; Cha, Y. L.; Kim, W.; Zhang, X.; Kim, D.-J., Polyaniline/Graphene-Functionalized Flexible Waste Mask Sensors for Ammonia and Volatile Sulfur Compound Monitoring. *ACS Applied Materials & Interfaces* **2022,** *14* (50), 56056-56064.

145. Cho, S. Y.; Lee, Y.; Koh, H. J.; Jung, H.; Kim, J. S.; Yoo, H. W.; Kim, J.; Jung, H. T., Superior chemical sensing performance of black phosphorus: comparison with MoS2 and graphene. *Advanced Materials* **2016,** *28* (32), 7020-7028.

146. Kim, J.-S.; Yoo, H.-W.; Choi, H. O.; Jung, H.-T., Tunable volatile organic compounds sensor by using thiolated ligand conjugation on MoS2. *Nano letters* **2014,** *14* (10), 5941-5947.

147. Cho, S.-Y.; Kim, S. J.; Lee, Y.; Kim, J.-S.; Jung, W.-B.; Yoo, H.-W.; Kim, J.; Jung, H.-T., Highly enhanced gas adsorption properties in vertically aligned MoS2 layers. *ACS nano* **2015,** *9* (9), 9314-9321.

148. VahidMohammadi, A.; Rosen, J.; Gogotsi, Y., The world of two-dimensional carbides and nitrides (MXenes). *Science* **2021,** *372* (6547), eabf1581.

149. Naguib, M.; Kurtoglu, M.; Presser, V.; Lu, J.; Niu, J.; Heon, M.; Hultman, L.; Gogotsi, Y.; Barsoum, M. W., Two-dimensional nanocrystals produced by exfoliation of Ti3AlC2. *Advanced materials* **2011,** *23* (37), 4248-4253.

150. Parui, A.; Srivastava, P.; Singh, A. K., Selective Reduction of CO2 on Ti2C(OH)2 MXene through Spontaneous Crossing of Transition States. *ACS Applied Materials & Interfaces* **2022,** *14* (36), 40913-40920.

151. Liu, X.; Chen, T.; Xue, Y.; Fan, J.; Shen, S.; Hossain, M. S. A.; Amin, M. A.; Pan, L.; Xu, X.; Yamauchi, Y., Nanoarchitectonics of MXene/semiconductor heterojunctions toward artificial photosynthesis via photocatalytic CO2 reduction. *Coordination Chemistry Reviews* **2022,** *459*, 214440.

152. van den Broek, J.; Abegg, S.; Pratsinis, S. E.; Güntner, A. T., Highly selective detection of methanol over ethanol by a handheld gas sensor. *Nature Communications* **2019,** *10* (1), 4220.

153. Ravi Kumar, Y.; Deshmukh, K.; Kovářík, T.; Khadheer Pasha, S. K., A systematic review on 2D materials for volatile organic compound sensing. *Coordination Chemistry Reviews* **2022,** *461*, 214502.

154. Chen, W. Y.; Jiang, X.; Lai, S.-N.; Peroulis, D.; Stanciu, L., Nanohybrids of a MXene and transition metal dichalcogenide for selective detection of volatile organic compounds. *Nature Communications* **2020,** *11* (1), 1302.

155. Tripathi, K. M.; Kim, T.; Losic, D.; Tung, T. T., Recent advances in engineered graphene and composites for detection of volatile organic compounds (VOCs) and non-invasive diseases diagnosis. *Carbon* **2016,** *110*, 97-129.

156.   He, S.; Li, W.; Feng, L.; Yang, W., Rational interaction between the aimed gas and oxide surfaces enabling high-performance sensor: The case of acidic α-MoO3 nanorods for selective detection of triethylamine. *Journal of Alloys and Compounds* **2019,** *783*, 574-582.

157.   Yuan, W.; Yang, K.; Peng, H.; Li, F.; Yin, F., A flexible VOCs sensor based on a 3D Mxene framework with a high sensing performance. *Journal of Materials Chemistry A* **2018,** *6* (37), 18116-18124.

158.   Adiguzel, Y.; Kulah, H., Breath sensors for lung cancer diagnosis. *Biosensors and Bioelectronics* **2015,** *65*, 121-138.

159.   Zhang, K.; Qin, S.; Tang, P.; Feng, Y.; Li, D., Ultra-sensitive ethanol gas sensors based on nanosheet-assembled hierarchical ZnO-In2O3 heterostructures. *Journal of Hazardous Materials* **2020,** *391*, 122191.

160.   Wang, L.; Kang, Y.; Liu, X.; Zhang, S.; Huang, W.; Wang, S., ZnO nanorod gas sensor for ethanol detection. *Sensors and Actuators B: Chemical* **2012,** *162* (1), 237-243.

161.   Azimi, P.; Zhao, D.; Pouzet, C.; Crain, N. E.; Stephens, B., Emissions of Ultrafine Particles and Volatile Organic Compounds from Commercially Available Desktop Three-Dimensional Printers with Multiple Filaments. *Environmental Science & Technology* **2016,** *50* (3), 1260-1268.

162.   Ubando, A. T.; Africa, A. D. M.; Maniquiz-Redillas, M. C.; Culaba, A. B.; Chen, W.-H., Reduction of particulate matter and volatile organic compounds in biorefineries: A state-of-the-art review. *Journal of Hazardous Materials* **2021,** *403*, 123955.

163.   Mirzaei, A.; Park, S.; Sun, G.-J.; Kheel, H.; Lee, C.; Lee, S., Fe2O3/Co3O4 composite nanoparticle ethanol sensor. *Journal of the Korean Physical Society* **2016,** *69* (3), 373-380.

164. Choi, S.; Bonyani, M.; Sun, G.-J.; Lee, J. K.; Hyun, S. K.; Lee, C., Cr2O3 nanoparticle-functionalized WO3 nanorods for ethanol gas sensors. *Applied Surface Science* **2018,** *432*, 241-249.

165. Li, Z.-g., Comparative study on WHO Western Pacific Region and World Federation of Chinese Medicine Societies international standard terminologies on traditional medicine: Diseases of Paediatrics (Part 1). *Journal of Integrative Medicine* **2015,** *13* (1), 61-64.

166. Ghassan, B. H.; Francine, L.; Aaron, J. C.; Ole, R.-N.; Michael, B.; Dana, L., Lung cancer and exposure to nitrogen dioxide and traffic: a systematic review and meta-analysis. *Environmental Health Perspectives* **2015,** *123* (11), 1107-1112.

167. Ram, K.; Sarin, M.; Sudheer, A.; Rengarajan, R., Carbonaceous and secondary inorganic aerosols during wintertime fog and haze over urban sites in the Indo-Gangetic Plain. *Aerosol and Air Quality Research* **2012,** *12* (3), 359-370.

168. Chen, C.; Campbell, K. D.; Negi, I.; Iglesias, R. A.; Owens, P.; Tao, N.; Tsow, F.; Forzani, E. S., A new sensor for the assessment of personal exposure to volatile organic compounds. *Atmospheric environment* **2012,** *54*, 679-687.

169. Spinelle, L.; Gerboles, M.; Kok, G.; Persijn, S.; Sauerwald, T., Review of portable and low-cost sensors for the ambient air monitoring of benzene and other volatile organic compounds. *Sensors-Basel* **2017,** *17* (7), 1520.

170. Chiang, W.-C.; Chen, C.-Y.; Lee, T.-C.; Lee, H.-L.; Lin, Y.-W., Fast and simple screening for the simultaneous analysis of seven metabolites derived from five volatile organic compounds in human urine using on-line solid-phase extraction coupled with liquid chromatography-tandem mass spectrometry. *Talanta* **2015,** *132*, 469-478.

171.   Haghighi, F.; Talebpour, Z.; Sanati-Nezhad, A., Through the years with on-a-chip gas chromatography: a review. *Lab on a Chip* **2015,** *15* (12), 2559-2575.

172.   Kumar, A.; Brunet, J.; Varenne, C.; Ndiaye, A.; Pauly, A., Phthalocyanines based QCM sensors for aromatic hydrocarbons monitoring: Role of metal atoms and substituents on response to toluene. *Sensors and Actuators B: Chemical* **2016,** *230*, 320-329.

173.   Xiao, X.; Zhou, X.; Ma, J.; Zhu, Y.; Cheng, X.; Luo, W.; Deng, Y., Rational Synthesis and Gas Sensing Performance of Ordered Mesoporous Semiconducting WO3/NiO Composites. *ACS Applied Materials & Interfaces* **2019,** *11* (29), 26268-26276.

174.   Li, W.-Y.; Xu, L.-N.; Chen, J., Co3O4 nanomaterials in lithium-ion batteries and gas sensors. *Advanced Functional Materials* **2005,** *15* (5), 851-857.

175.   Fu, D.; Zhu, C.; Zhang, X.; Li, C.; Chen, Y., Two-dimensional net-like SnO 2/ZnO heteronanostructures for high-performance H 2 S gas sensor. *Journal of Materials Chemistry A* **2016,** *4* (4), 1390-1398.

176.   Li, N.; Fan, Y.; Shi, Y.; Xiang, Q.; Wang, X.; Xu, J., A low temperature formaldehyde gas sensor based on hierarchical SnO/SnO2 nano-flowers assembled from ultrathin nanosheets: Synthesis, sensing performance and mechanism. *Sensors and Actuators B: Chemical* **2019,** *294*, 106-115.

177.   Michel, C. R.; Martínez-Preciado, A. H.; López-Mena, E. R.; Elías-Zuñiga, A.; Cayetano-Castro, N.; Ceballos-Sanchez, O., Improvement of the gas sensing response of nanostructured LaCoO3 by the addition of Ag nanoparticles. *Sensors and Actuators B: Chemical* **2017,** *246*, 181-189.

178.	Iwakuni, H.; Shinmyou, Y.; Yano, H.; Matsumoto, H.; Ishihara, T., Direct decomposition of NO into N2 and O2 on BaMnO3-based perovskite oxides. *Applied Catalysis B: Environmental* **2007,** *74* (3-4), 299-306.

179.	Zoolfakar, A. S.; Ahmad, M. Z.; Rani, R. A.; Ou, J. Z.; Balendhran, S.; Zhuiykov, S.; Latham, K.; Wlodarski, W.; Kalantar-zadeh, K., Nanostructured copper oxides as ethanol vapour sensors. *Sensors and Actuators B: Chemical* **2013,** *185*, 620-627.

180.	Qin, W.; Yuan, Z.; Gao, H.; Zhang, R.; Meng, F., Perovskite-structured LaCoO3 modified ZnO gas sensor and investigation on its gas sensing mechanism by first principle. *Sensors and Actuators B: Chemical* **2021,** *341*, 130015.

181.	Jo, Y. K.; Jeong, S.-Y.; Moon, Y. K.; Jo, Y.-M.; Yoon, J.-W.; Lee, J.-H., Exclusive and ultrasensitive detection of formaldehyde at room temperature using a flexible and monolithic chemiresistive sensor. *Nature Communications* **2021,** *12* (1), 4955.

182.	Nakata, S.; Shiomi, M.; Fujita, Y.; Arie, T.; Akita, S.; Takei, K., A wearable pH sensor with high sensitivity based on a flexible charge-coupled device. *Nature Electronics* **2018,** *1* (11), 596-603.

183.	Wen, X.; Cai, Y.; Nie, X.; Xiong, J.; Wang, Y.; Song, H.; Li, Z.; Shen, Y.; Li, C., PSS-doped PANI nanoparticle/Ti3C2Tx composites for conductometric flexible ammonia gas sensors operated at room temperature. *Sensors and Actuators B: Chemical* **2023,** *374*, 132788.

184.	Barkade, S. S.; Naik, J. B.; Sonawane, S. H., Ultrasound assisted miniemulsion synthesis of polyaniline/Ag nanocomposite and its application for ethanol vapor sensing. *Colloids and Surfaces A: Physicochemical and Engineering Aspects* **2011,** *378* (1-3), 94-98.

185.	Gawri, I.; Ridhi, R.; Singh, K.; Tripathi, S., Chemically synthesized TiO2 and PANI/TiO2 thin films for ethanol sensing applications. *Materials Research Express* **2018,** *5* (2), 025303.

186. Das, M.; Sarkar, D., Development of room temperature ethanol sensor from polypyrrole (PPy) embedded in polyvinyl alcohol (PVA) matrix. *Polymer Bulletin* **2018,** *75*, 3109-3125.

187. Liu, Y.; Zhang, B.; Yang, Y.; Chang, Z.; Wen, Z.; Wu, Y., Polypyrrole-coated α-MoO 3 nanobelts with good electrochemical performance as anode materials for aqueous supercapacitors. *Journal of Materials Chemistry A* **2013,** *1* (43), 13582-13587.

188. Yenorkar, S. M.; Zade, R. N.; Mude, B. M.; Mayekar, V. M.; Mude, K. M.; Raulkar, K. B.; Mistry, R. R.; Patange, A. In *Polymer-Metal Oxide Composite (PPy–MoO3) for Ammonia and Ethanol Gas Sensor*, Macromolecular Symposia, Wiley Online Library: 2021; p 2100049.

189. Bhati, V. S.; Kumar, M.; Banerjee, R., Gas sensing performance of 2D nanomaterials/metal oxide nanocomposites: A review. *J Mater Chem C* **2021**.

190. Agrawal, A. V.; Kumar, N.; Kumar, M., Strategy and future prospects to develop room-temperature-recoverable NO 2 gas sensor based on two-dimensional molybdenum disulfide. *Nano-micro letters* **2021,** *13*, 1-58.

191. Lee, E.; VahidMohammadi, A.; Prorok, B. C.; Yoon, Y. S.; Beidaghi, M.; Kim, D.-J., Room Temperature Gas Sensing of Two-Dimensional Titanium Carbide (MXene). *ACS Applied Materials & Interfaces* **2017,** *9* (42), 37184-37190.

192. Kim, S. J.; Koh, H.-J.; Ren, C. E.; Kwon, O.; Maleski, K.; Cho, S.-Y.; Anasori, B.; Kim, C.-K.; Choi, Y.-K.; Kim, J.; Gogotsi, Y.; Jung, H.-T., Metallic Ti3C2Tx MXene Gas Sensors with Ultrahigh Signal-to-Noise Ratio. *ACS Nano* **2018,** *12* (2), 986-993.

193. Zhang, S.; Song, P.; Sun, J.; Ding, Y.; Wang, Q., MoO3/Ti3C2Tx MXene nanocomposites with rapid response for enhanced ethanol-sensing at a low temperature. *Sensors and Actuators B: Chemical* **2023,** *378*, 133216.

194.   Bu, X.; Ma, F.; Wu, Q.; Wu, H.; Yuan, Y.; Hu, L.; Han, C.; Wang, X.; Liu, W.; Li, X., Metal-organic frameworks-derived Co3O4/Ti3C2Tx Mxene nanocomposites for high performance ethanol sensing. *Sensors and Actuators B: Chemical* **2022,** *369*, 132232.

195.   Luo, W.; Sun, Y.; Han, Y.; Ding, J.; Li, T.; Hou, C.; Ma, Y., Flexible Ti3C2Tx MXene/polypyrrole composite films for high-performance all-solid asymmetric supercapacitors. *Electrochimica Acta* **2023,** *441*, 141818.

196.   Yang, S.; Yang, R.; Lin, Z.; Wang, X.; Liu, S.; Huang, W.; Chen, Z.; Wei, J.; Zeng, Z.; Chen, H., Ultrathin, flexible, and high-strength polypyrrole/Ti 3 C 2 T x film for wide-band gigahertz and terahertz electromagnetic interference shielding. *Journal of Materials Chemistry A* **2022,** *10* (44), 23570-23579.

197.   Zheng, C.; Yao, Y.; Rui, X.; Feng, Y.; Yang, D.; Pan, H.; Yu, Y., Functional MXene-Based Materials for Next-Generation Rechargeable Batteries. *Advanced Materials* **2022**, 2204988.

198.   Li, C.; Xu, J.; Xu, Q.; Xue, G.; Yu, H.; Wang, X.; Lu, J.; Cui, G.; Gu, G., Synthesis of Ti3C2 MXene@PANI composites for excellent anticorrosion performance of waterborne epoxy coating. *Progress in Organic Coatings* **2022,** *165*, 106673.